Development of Novel Tools for Application of Ultrasonic Guided Waves in Fibre-Composites

A Thesis submitted to the University of Sheffield for the degree of Doctor of Philosophy in the Faculty of Engineering

by

Marcus Haywood-Alexander

Department of Mechanical Engineering
University of Sheffield

February 2022

ACKNOWLEDGEMENTS

The last three years, working on this project, have been an amazing experience. Not only have I learnt so much, thanks to the guidance and help from colleagues, but these people have become friends who I will hold dear for a long time. This work would not have been possible without their support and friendship.

Firstly, I would like to thank my supervisor Dr. Nikolaos Dervilis, who has been an amazing tutor, given incredible support, and was always on guard to prevent my burn-out. I am grateful for his wisdom, belief and encouragement, which was a primary reason for the success of the project. I would also like to thank Dr. Timothy Rogers for his guidance in the realm of probabilistic methods, and for always being enthusiastic whenever I needed help. Thanks also goes to Professor Keith Worden for his inspiration and teaching, and for opportunities in projects outside of this thesis.

The lab work in this project would not have been possible without several other valued colleagues. Firstly, Dr. Robin Mills, for sharing their fountain of knowledge in all things experimental, and for always being on hand to help when things were inevitably difficult. My gratitude goes to Michael Dutchman for making vital components of the laboratory setup. Special thanks also to Dr. Ramon Fuentes for being a great tutor at the beginning and for stoking the fire of my predilection for experimental work.

The Dynamics Research Group has been a brilliant group to be a part of, thanks to their high standards, wealth of knowledge, and uplifting demeanour. The DRG members have become more than colleagues, but friends; so, I would also like to thank Matty, Aidan, Max, Chandy, Julian, Tina, Chris Lindley, Tim Rooker, Kartik, and many others for making this a cherished period of time.

This project has been in close collaboration with Siemens Gamesa Renewable Energy, and there are many other people to thank from this organisation for their reception and help in navigating the boundary of research and industry application. My thanks go to Purim, Mads, Nevena, and Lars from SGRE. A special thanks goes to Purim and Mads for performing tests on my behalf when travel was restricted as a result of the pandemic. I would like to thank the EPSRC for their grant which funded this project (EP/R004900/1).

During the past three years, there are many others to thank for their friendship, and for making my time outside of the PhD a joy. To Colley, Dale, Chris Fung, Alex, Liam, thank you for being close friends, the entertaining and exciting times, and for helping keep my mental health intact with the adventures and all things mountainous. Thanks to Chris Smith, Lily, Elliott, Charlotte, Hamish, Jack Whittaker, Rob, and Jack Childerstone for their continued friendship. And a marked thank you goes to Hannah, for encouraging and supporting me, and for making the final year a lot more pleasant than it had any right to be.

I have always had the support of my family, who continually dealt a healthy dose of encouragement. So, a special thank you to Nicola, Ove, Mike, Byron, and Beth. And thanks to many other extended family members for their support (and for listening patiently after regretfully asking about my topic).

ABSTRACT

In order to decrease risk, downtime, and costs; modern structures often employ strategies to monitor their state and determine the existence, and characteristics, of any damage present. Ultrasonic guided waves may offer a convenient and practical approach to this problem. UGWs, offer a number of distinct advantages, such as; long range, accurate sizing potential, greater sensitivity and cost effectiveness. However, the current state-of-the-art for applications of UGWs in fibre composites is juvenile in comparison to their application in isotropic and homogeneous materials. The aim of this work was to develop advanced, novel tools for deeper understanding of ultrasonic guided waves, so that they can help and enhance NDE/SHM strategies for fibre-composite materials.

In particular, three tools have been developed, the details and results of which are presented in this thesis. The first of these tools is a physics-informed approach to machine learning of guided-wave feature spaces. In order to assess damage in a structure, and implement any NDE or SHM strategy, knowledge of the behaviour of a guided wave throughout the material/structure is important. Determining this behaviour is extremely difficult in fibre-composites, where unique phenomena such as continuous mode conversion takes place. This thesis introduces a novel method for modelling the feature-space of guided waves in a fibre-composite material. This technique is based on a data-driven model, where prior physical knowledge can be used to create structured machine-learning tools; where constraints are applied to provide said structure. The method makes use of a Gaussian process, a full Bayesian analysis tool. Experimental data of an energy-based Lamb wave feature over a fibre-composite plate were collected. This data was then fed through multiple learning algorithms, each with increasing levels of prior knowledge embedded. The work has shown how physical knowledge of the guided waves can be utilised in modelling using an ML tool, and that by careful consideration when applying machine-learning techniques, more robust models can be generated, which offer advantages such as extrapolation, physical interpretation, and increased performance.

The second tool developed was a Bayesian approach to decomposition of single-source, multi-mode signals. This tool was tested on a localisation problem, where decomposition of single-source signals is required to provide information on signals reflected from the damage. A simulation method which can model complex multi-mode wave interaction was used to demonstrate the capability of the decomposition tool. The tool shown here has a distinct advantage in that it produces quantified results for the uncertainty in the decomposed signal, which lends well to any NDE/SHM strategy utilising probabilistic approaches for detection. Furthermore, it was shown that the method inherently produces parametric features which are indicative of the physical behaviour of the wave. The proposed decomposition method was shown to allow localisation of damage accurate to within 1mm in many sensor configurations.

The final tool shown in this thesis, is a Bayesian method for material identification using UGWs. This tool was assessed with the objective of determining accurate group velocity, as is required for localisation of damage. The method uses a Markov chain Monte Carlo procedure to simulate samples of the distribution for each of the parameters. Observations of dispersion-curve data were measured, and used to assess the material properties using a computationally-efficient solution to dispersion curves in orthotropic materials. The results showed the importance and capability of the method having freedom to generate the posterior distribution with respect to both shape and multivariate dependencies. Furthermore, the work presented shows that the method performs well for the objective of determining accurate dispersion-curve information – i.e. group velocity curves.

NOMENCLATURE

Symbol	Variable	Unit
A	Amplitude of wave	
c	Bulk wave velocity	m/s
$c_{(p,g)}$	Wave velocity (phase and group)	m/s
$c_{(L,T)}$	Wave velocity (longitudinal and transverse)	m/s
C_{ijkl}	Stiffness tensor	N/m^2
D	Boolean image mask	
$\mathcal{D}$	Dataset	
E	Young's Modulus	N/m^2
$\mathbb{E}[\mathbf{y}]$	Expected values of model output	
f	frequency	Hz
h	Plate half-thickness	m
h_m	Maximum of Hilbert-envelope of signal	m
k	Wavenumber	rad/m
$k(\mathbf{x}, \mathbf{x})$	Covariance function	
ℓ	lengthscale	
$m(\mathbf{x})$	Mean function	
$NMSE$	Normalised mean squre error	
PLL	Predictive log-likelihood	
q	Dimensionless spatial coordinate	
t	Time	s

u_i	Displacement in direction i	m
$\mathbf{V}$	Covariance matrix	
$\mathbb{V}[\mathbf{y}]$	Expected variance of model output	
$\mathbf{w}$	Weight vector	
x	Propagation distance	m
x	x-coordinate	m
$\mathbf{x}$	Input vector of data point i	
$\mathbf{X} \subset \mathcal{D}$	Input set	
x_i	Location in direction i	m
y	Output of model	
y	y-coordinate	m
$\mathbf{y} \subset \mathcal{D}$	Output set	
$\tilde{\mathbf{y}}$	Predicted output	
β	Basis function coefficients	
ε	Model noise	
ε_{ij}	Strain field tensor element	
$\lambda,\ \mu$	Lamé parameters	N/m^2
ν	Poisson's ratio	
ρ	Density	kg/m^3
ρ	Radial coordinate	m
σ^2	Variance	
σ_{ij}	Stress field tensor element	N/m^2
θ	Angular coordinate	rad
θ	Propagation angle	rad
Θ	Parameter vector	
ω	Circular frequency	rad/s
ζ	Viscoelastic attenuation coefficient	

Table of Contents

1

INTRODUCTION

In engineering applications, the use of complex materials, such as fibre-composites, can offer benefits thanks to their high strength-to-weight ratio. In addition to the use of such materials, the employment of damage detection and state-monitoring strategies is also gaining popularity in order to decrease risk, downtime and costs. As well as determining the existent of damage, the location and characteristics of the damage are sought. Ultrasonic guided waves (UGWs), may offer a convenient and practical approach to this problem, as they have some distinct advantages – which will be discussed later in this chapter – and, thanks to analogy with diffraction theory, can detect, locate, and characterise damage of small size.

When applying UGWs on fibre-composite materials, there are many difficulties to overcome; which has limited their application to relatively-simple scenarios. The aim of this work was to develop advanced, novel tools, which enhance further understanding of UGWs in fibre-composite materials, in order to robustly design and implement/enhance damage detection strategies. The motivation for this project comes from the industry partner Siemens Gamesa Renewable Energy (SGRE). One such structure which uses fibre-composite materials and would benefit from a robust damage detection system is the wind turbine blade. In particular, there is a motive from SGRE to detect and locate damage in critical locations of the blade; which is where UGWs may offer an appropriate solution. In order to robustly develop such a system using UGWs, it is beneficial to develop some modern tools which will further enhance the understanding, and application, of UGWs in fibre-composites.

This chapter aims to introduce the concepts of non-destructive evaluation (NDE) and structural health monitoring (SHM), followed by how these strategies are useful for wind turbine blades. The uses of ultrasonic waves for NDE and SHM purposes are then introduced, and finally the objectives of this work are detailed, along with a brief outline of the chapters in the thesis.

1.1 Non-Destructive Evaluation and Structural Health Monitoring

Testing and monitoring of systems, objects and materials is so habitual that one doesn't notice. Inspection of the state of a system or structure can be either periodic (or interruptive) or continuous in its execution. This description of inspection frequency is one of the main differences in characterising *non-destructive evaluation* (NDE) and *structural health monitoring* (SHM). To better understand how these might differ in practice, it can be useful to explore the concept of checking the state of a car.

When purchasing a pre-owned car, a buyer will inspect the body and engine for any visible defects. This person might also run the engine and take the car for a drive, referring to how they know a car *should* operate or feel. The detection of any faults is done using an intuitive knowledge set – which could be called *features* – developed over years of driving; such as engine sound, clutch smoothness or exhaust. By proper checking of the car, the buyer can avoid large costs that would be associated with purchasing a damaged vehicle. The periodic checking of the state of the car by checking against the *expected* feature behaviour can be compared to *non-destructive evaluation* (NDE).

Modern cars can tell the driver where faults are, based on onboard sensors at known locations, which can be used to detect significant changes from the norm. The addition of an onboard diagnosis system decreases the uncertainty of defect detection and increases the efficiency of repair by providing information on the type and location of the defect. In an industrial context, continuous assessment and monitoring of the health of structures and systems has the same benefits of avoiding unnecessary cost, increasing efficiency and reducing waste. This concept is known as *structural health monitoring* (SHM). Detection via an intuitive sense is how one might envision the use of a probabilistic perspective on SHM.

Generally, the main difference between SHM and NDE, is the applicability of SHM strategies to be employed *on-line*. Farrar and Worden [1], state that SHM 'usually refers to the process of implementing a damage detection strategy for aerospace, civil or mechanical engineering infrastructure.' Though NDE is usually carried out *off-line*, such strategies can be used *in-situ* on structures. Traditionally, NDE is used when the site of potential damage is located, and so monitoring strategies may employ a two-step application where SHM alerts the engineers of damage being present, and NDE is used to locate, size or assess the damage.

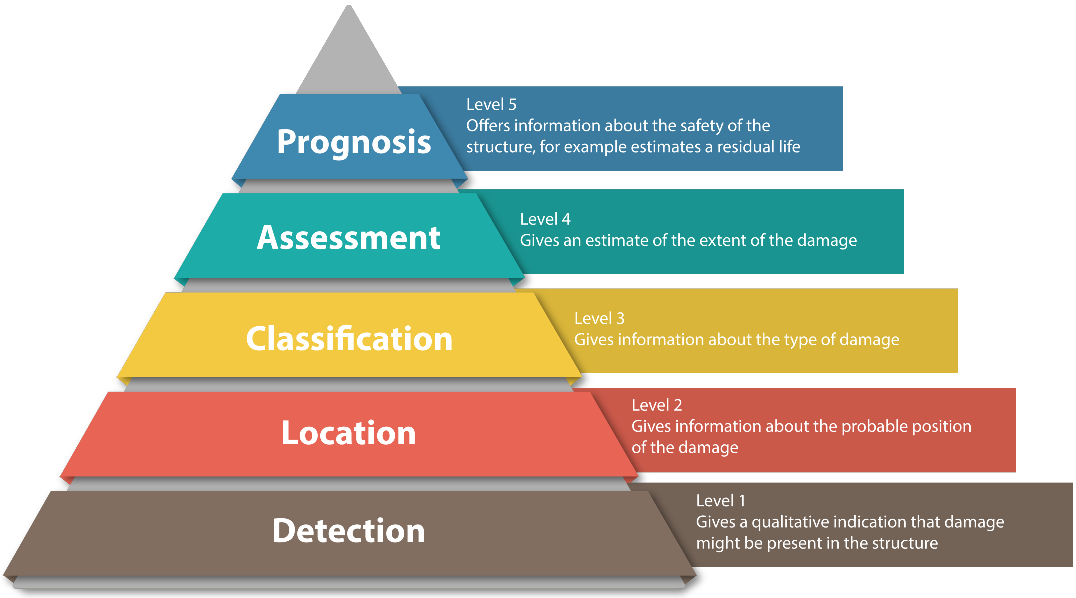

Figure 1.1: Adaption to Rytter's proposed hierarchy of SHM [1, 2].

Rytter [2] proposed a hierarchical structure to SHM, where each level requires that all lower-level information is available. The original hierarchy was proposed as follows,

- Level 1: detection,
- Level 2: location,
- Level 3: assessment,
- Level 4: prediction.

This four-stage hierarchy was then adapted by Farrar and Worden [1], to include *classification*, which is required when multiple damage mechanisms are possible. This five-stage hierarchy is shown in Figure 1.1, and has been widely adopted in the SHM community. This hierarchy can also be used in NDE; however it is likely that a minimum of at least Level Two would be necessary for an adequate NDE routine.

1.2 SHM and NDE for Fibre-Composite Materials

Modern structures are increasingly using fibre-composite materials (FCMs) thanks to advantages such as their strength-to-weight ratio [3]. Along with complex materials, modern structures are also progressively including SHM or NDE strategies into their infrastructure. There are a variety of methods used to detect damage in FCMs, each with their own advantages [4]. For example, SHM can be done using vibration analysis [5], in which the techniques do not vary greatly from non-complex materials and so are simpler to apply. Or, one might use methods involving shorter wavelengths, such as acoustic emission [6] or ultrasonic guided waves [7]. By analogy to diffraction theory, the use of shorter wavelengths allows for detection and characterisation of damage of smaller size; however, the implementation of strategies using these methods can be more difficult.

For a system which is capable of achieving levels 2 or 3 in Rytter's hierarchy [2], high-frequency elastic waves offer a useful tool. Acoustic emission (AE) is a passive approach to using such waves, whereby data is recorded when a 'burst' of read by the acoustic sensors. The use of AE was initially explored, however, there are two main disadvantages which deterred further investigation for this project. The first of these is the dependency of the propagation velocity of the wave on its frequency and propagation angle. With an active system, the central frequency is better controlled

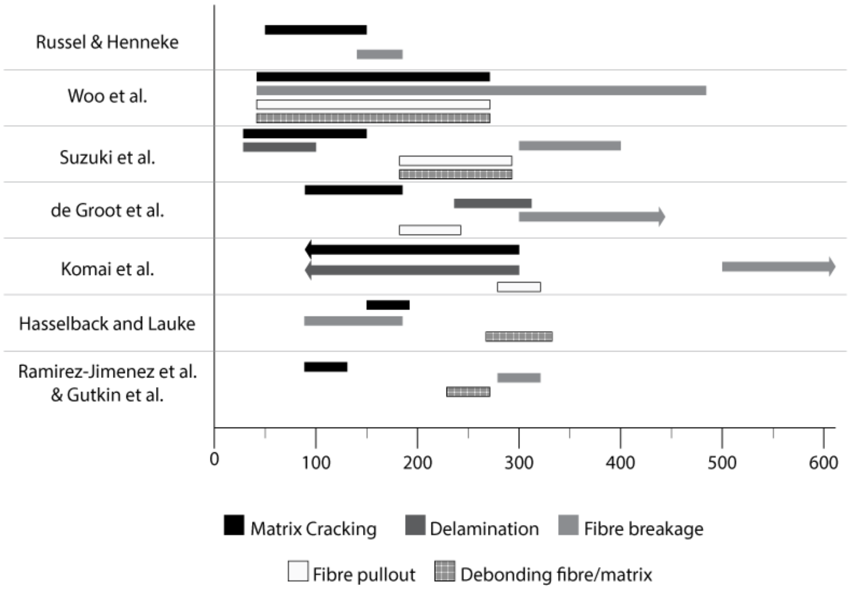

Figure 1.2: A comparison of characteristic frequencies of failure modes from various studies of composite structures [8–14]. Extended from the study by Autieri [15].

and known and so only the angular dependency needs to be overcome. The second disadvantage with respect to AE is the irregularity of characteristics frequencies of failure modes, as shown in Figure 1.2.

Fibre-reinforced polymers give rise to a number of increased difficulties in an SHM or NDE context, such as; greater number of failure mechanisms [16–18], increased modelling complexity [19], and nonlinear behaviour [20, 21]. There exists a broad range of strategies aiming to address these additional complexities in monitoring fibre-composite structures, from increased fidelity of physical modelling [22], to the use of machine-learning techniques to ‘fill in the gaps’ left behind by incomplete physical models [23], and lots of techniques in between.

An example of a fibre-composite structure which would benefit from a robust monitoring or damage identification system is a wind-turbine blade (WTB). There have been advances in methods involving the use of low-frequency behaviour of the blades in order to detect the onset of damage [24], though using a diffraction theory analogy suggests that these require large levels of damage in order to provide a significant enough change for detection. Furthermore, the information in these structures is highly susceptible to environmental conditions [25], such as wind speed (and therefore load).

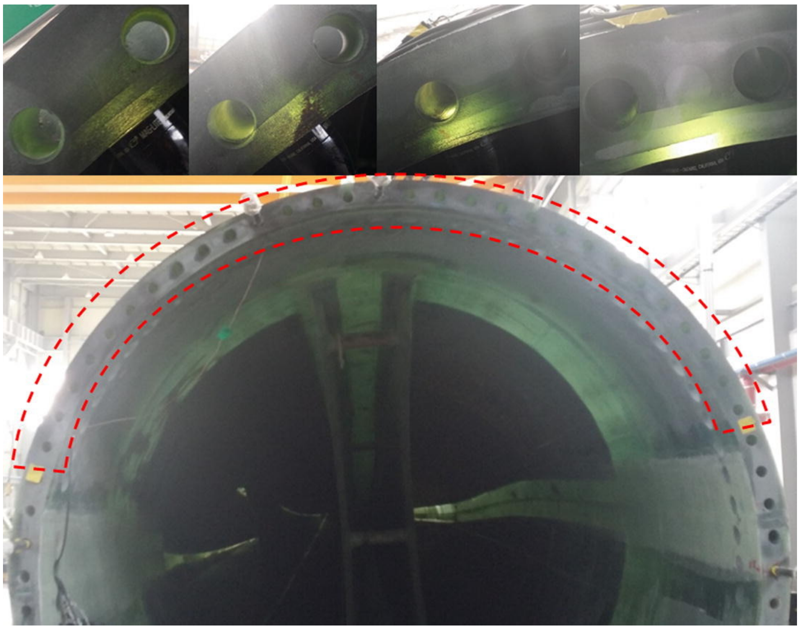

Figure 1.3: Example of the root of a wind turbine blade, which is an area susceptible to damage. Taken from Lee *et al.* [26].

Wind turbine blades are made of complex geometries and materials, therefore, there is a wide variety of failure mechanisms, severity and possibilities [27]. Geometric complexities at the root can cause delamination failures as a result of bumping of the blade shell [26], an example of which can be seen in Figure 1.3. Areas of structural joints, such as the web, can fail by debonding, delamination or core failure (where the wooden core exhibits cracks) [28]. Structural bond lines can suffer from tensile cracks, which can change direction partway through the damage life-cycle [29]. It is clear that there are several critical locations on the blade where there is motivation for an active monitoring strategy that can provide information at higher levels of the SHM hierarchy (Figure 1.1). Some of these critical locations are shown in Figure 1.4.

By using higher-frequency behaviour of the structure, advances in localisation and earlier detection can be made [30]. Ultrasonic scans have shown to be useful for

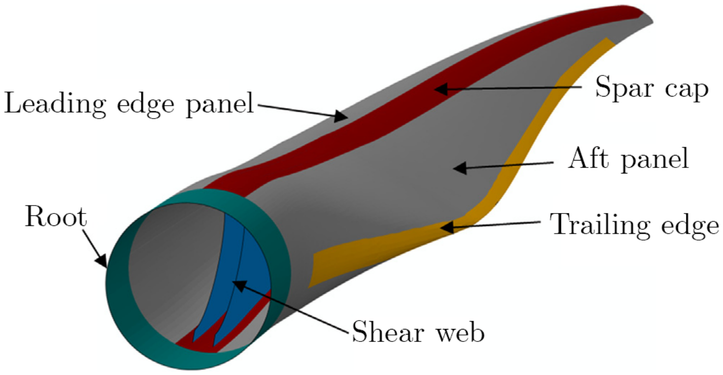

Figure 1.4: Diagram showing some critical locations on the wind turbine blade.

locating otherwise invisible damage within the material of the blades [31]. Previous work has shown the potential for the use of ultrasonic waves for application to damage detection on WTBs [32–34]. A network of on-board piezoelectric transducers was also tested, which successfully detected damage with basic techniques [35]. These papers show that ultrasonic waves offer a promising approach for damage detection in WTBs, although more advanced tools may be necessary to improve guided wave application in complex materials and geometries.

1.3 Use of Ultrasonic Waves in SHM and NDE

Ultrasonic waves are the general name for high-frequency stress waves within a material, and the use of these waves for damage detection has become increasingly prominent in SHM systems. An active example of using ultrasonic waves for damage detection is the use of *ultrasonic guided waves* (UGWs). This method induces a wave within certain structure types which act as wave-guides, and analysis of the *wave-packet* as it arrives in certain locations can give indications of any inhomogeneities in the structure. Figure 1.5 gives an illustration of how ultrasonic guided waves can be used to detect damage. The strength of UGWs as a damage detection tool is further reinforced by their additional use in automatic inspection during component manufacture [36]. The primary characteristic of UGW-based NDE/SHM regimes is by measuring both the direct (here named *nominal*) and reflected waves.

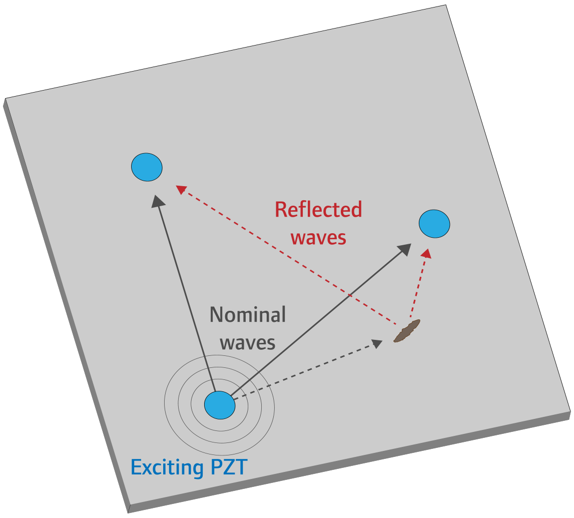

Figure 1.5: Illustration of damage detection using ultrasonic guided waves.

A good overview of the current and potential uses of UGWs in SHM is presented by Rose [37], as well as their limitations. There are a variety of natural wave-guides present in many structures, such as rods, hollow cylinders and, importantly for use in WTBs, multi-layered structures and plates. Some of the benefits of UGWs for SHM are:

i. inspection over long distance is possible with a single probe;
ii. via mode and frequency tuning, they have excellent detection and sizing potential;
iii. they have greater sensitivity than standard beam ultrasonic inspection;
iv. their ability to inspect hidden structures with great sensitivity;
v. their cost effectiveness, thanks to their simplicity and speed.

Many applications of UGWs have been demonstrated, and are gaining traction in the context of SHM and NDE in aircraft applications [38–40], because of their sensor simplicity, and capability to detect defects in complex structures. Thanks to their lightweight and simple system setup, they are often used for remotely deployed sensing systems [41].

Applying ultrasonic waves for SHM and NDE purposes on composite materials presents a number of increased difficulties [42] – much like any other damage-detection strategy for application to complex materials. In particular for fibre-composites, these difficulties include; steering of group velocity, additional damping from the epoxy matrix, and wave scattering from the fibres [43]. At the risk of repetition, addressing these difficulties has been attempted via the use of more complex analytical and numerical models [44–46], machine-learning methods [47, 48], and techniques in between [49].

1.4 Project Motivation and Objectives

The initial motivation behind the project was to research inspection methods for fibre-composite materials (FCMs). After an initial study, it was found that ultrasonic guided waves offer a potential solution for an active method of detecting damage in FCMs, however, guided waves in fibre-composites cannot be applied with rudimentary techniques. Therefore, the aim of the thesis was focussed to developing unique tools that advance new ways in understanding, and the use of, guided waves in fibre-composite structures. To attempt to achieve this aim, the objectives in this thesis are:

- To develop a method of determining physics-based feature spaces which are useful for damage detection.
- To build a localisation strategy which combats the steering behaviour of the group velocity.
- To develop a physics and data-driven method of determining accurate dispersion curve information for fibre-composite materials.

The motivation behind the first objective was to determine the ‘baseline’ model of the damage-sensitive feature set, but with more capabilities than a purely data-driven approach. The first objective can be classed into the first stage of Rytter’s hierarchy [2], and so the second objective was with an aim to develop tools for use in the second stage of the hierarchy. Localisation requires decomposition of the wave signals, though there is motivation to include a probabilistic approach to this decomposition, as this provides several advantages which are discussed later. The motivation behind the third tool follows on directly from the second; as the propagation velocity of the wave is required for localisation, it is important to be able to determine this information accurately for the material in question.

1.5 Outline of the Thesis

The thesis begins by detailing background information on using guided waves for SHM and NDE purposes. In Chapter 2 a review of the literature is presented which notes the current state-of-the-art and where there are gaps in research and the tools available. Following this, a detailed knowledge of the physics of ultrasonic waves is built in Chapter 3, as well as guided-wave phenomena in fibre-composites and the modelling techniques used in this work. Chapter 4 then gives an overview of the machine-learning techniques used in this thesis, including quantitative performance metrics used to assess the models generated.

At this point, the novel work of this project is presented for the remainder of the thesis. Chapter 5 shows the work done to generate feature spaces of guided waves in complex materials, using the machine-learning techniques introduced in Chapter 4, and is steered by the knowledge of physics built in Chapter 3. This work is applied to an experimental setup where guided waves are measured in a carbon-fibre composite using a scanning laser Doppler vibrometer (SLDV). In Chapter 6, a novel method of defect localisation is presented, which uses a probabilistic approach to decompose the wave signals, to extract signals of waves reflected from the defect. Chapter 6 directly leads on to the focus of Chapter 7, where the problem of modelling the wave propagation velocity is addressed. In Chapter 7, a Bayesian approach to determining this model is presented, using SLDV data to identify the material properties which govern wave velocity. Finally, conclusions are presented in Chapter 8, along with suggestions for further work.

2

LITERATURE REVIEW

This chapter provides an overview of the literature of ultrasonic guided waves (UGWs), their use in damage detection, and the state-of-the-art in their use in fibre-composite materials. The chapter begins in Section 2.1 by showing related work on the general background of UGWs. Section 2.2 presents the literature on guided waves in anisotropic and composite media, discussing modelling techniques and unique phenomena. This material is followed by a presentation of feature modelling strategies in Section 2.3, and guided wave interactions with damage in Section 2.4. Next, there are two associated sections on literature for Lamb-wave localisation and signal decomposition in Sections 2.5 and 2.6 respectively. Finally, literature is discussed on determining dispersion characteristics for guided waves in Section 2.7, which is followed by a summary of the literature in Section 2.8

The discussion on the literature here is aimed to be as non-technical and general as possible, with limited (or low-level) prior knowledge on guided waves required. However, if the reader would prefer to understand more on the mechanics of UGWs, detailed information on such is presented in Chapter 3. In this chapter, where required, a brief description of the UGW phenomena, which is being discussed, will be given.

2.1 Ultrasonic guided waves

One of the earliest resources available on the physics of guided waves is the work of Viktorov [50], where governing physical properties for both Rayleigh and Lamb waves are detailed. In the relatively short book, Viktorov uses fundamental physics to derive the equations which define the characteristics of guided waves in isotropic media. The book finishes with some brief examples of applications of ultrasonic guided waves in engineering, which arguably prophesied what was to come in later years.

When elastic waves propagate in certain structure types, guided waves can exhibit as either Rayleigh or Lamb waves. The former of these wave types is where the wave propagates on the surface of the medium, whereas in the latter as bounded by two surfaces. Further details on the physics of these waves, which are crucial understanding for their use in NDE and SHM regimes, are given in Chapter 3. Where discussion in this chapter references certain physical phenomena, this will be explained briefly here, and in more detail in later chapters. Now, there are a wealth of resources available for knowledge on ultrasonic guided waves (UGWs). For an introduction to UGWs, some useful reading is the work from Worden [51] and Rose [52]. In these writings, the fundamental concepts and physics of UGWs are introduced in an-easy-to follow manner, and are used as a reference for Chapter 3.

As stated earlier, and first referenced by Viktorov [50], UGWs are primarily used for non-destructive evaluation and structural health monitoring [38–40]. In their books, Rose [37] and Kundu [53], outline how UGWs are used in damage-detection strategies, and the physics and knowledge required for such application. Some key pre-requisite knowledge is of the dispersive properties of UGWs in the system of application; which are described by the relationship between the *central frequency* and the *wavenumber, phase velocity, or group velocity* of the wave.

There are several techniques available for detecting damage in composite materials using guided waves – in particular Lamb waves [54–56]. A key separation of methods for the study of Lamb waves is in the sparsity of measurement points; by this, one means primarily the use of individual sensors placed on the structure [57], or the use of a scanning-laser doppler vibrometer to measure a high density of points over the wave propagation [58]. In practice, the use of a high-density array for guided wave-based damage detection regimes is expensive and impractical, as it often requires laser-scanning-Doppler-vibrometers (SLDVs). The method often results in images which can be used to directly infer damage states [59]. However, their use is in the understanding and modelling stages of guided-wave strategies. As the quantification and modelling of guided waves in fibre-composite materials is still in a juvenile stage, much of the work here uses the high-density wave propagation measurements to deliver tools which can provide the beginning stages of a damage-detection regime.

2.2 Guided waves in anisotropic media

When elastic waves propagate in anisotropic media, the modelling and solutions become very complex, even more so when attempting to model their interaction with defects [60–62]. There have been several techniques shown which attempt to determine accurate numerical models of wave propagation in complex materials.

Another approach is to use finite-element modelling to generate an accurate physical model of wave propagation [63]. Developments in finite element modelling have included using a combined model to include physical descriptions of Lamb waves [64, 65]. However, the finite-element modelling approach has shortcomings, such as only being able to model one fundamental mode at a time [66], and so complex dispersive interactions between modes are not captured. Furthermore, because of computational constraints, these methods are still limited to transversely isotropic, or quasi-isotropic materials.

Another method of modelling guided-wave propagation in plates is using the local interaction simulation approach (LISA), which allows for more complex materials and wave interaction to be directly modelled. Application of this method was first shown by Delsanto [67–69], and has been shown to be accurate for use in Lamb-wave modelling for more complex methodologies by Dobie [70], who included a linear-systems model to allow for effects of the actuator to be applied. The LISA approach was improved further, to allow for simulation of anisotropic materials, by Nadella and Cesnik [71, 72], and was improved further to include viscoelastic properties of the material [73]. The main shortcoming of this method is the limit imposed by computational memory, and so only small systems can be modelled.

A crucial characteristic of guided waves in fibrous materials, such as carbon-fibre-reinforced-polymers (CFRP), is the phenomena of Continuous Mode Conversion (CMC) [74], as shown by Mook *et al* [75] and Willberg *et al* [76], where the boundaries of layers or weaves cause conversion of mode shapes with frequent-enough occurrence that they can be considered continuous along the propagation path. CMC can cause many issues in the application of UGWs in fibre-composite structures, in particular for time-series analysis techniques where the signal shape is more precisely dependent on the propagation distance when compared to less-complex material types. At propagation paths through the fibres, the energy of all modes is reduced, thanks to this phenomena. Much of the study into CMC is at a qualitative level currently, with much of the focus being on the first stages of numerical modelling of the phenomena. In certain structures, where CMC operates on a much smaller spatial scale than the area of interest, it may be useful to consider the problem at a more stochastic level, and consider the distribution of wave characteristics due to CMC instead.

Another key consideration of guided waves in anisotropic media is the propagation-angle-dependent wave velocity [77]. Determining this velocity can be done by measuring the onset of the wave-front at known distances [78], although for generating a model over a large frequency range, this could quickly become laborious and costly. A recent advancement in determining dispersion curve solutions of anisotropic materials was first shown by Lefebvre [79], which uses a Legendre polynomial expansion to form an eigenvalue problem for the final solution. This approach was then shown applicable to single and multi-layer orthotropic plates by Othmani [80,81], highlighting the method's much lower computational cost.

2.3 Guided wave feature modelling

In Chapter 1, the concepts of non-destructive evaluation and structural health monitoring were introduced. Both of these concepts use *features* as quantitative measures which provide information on the damage [1], and are used at all levels of Rytter's hierarchy [2]. Determining the feature space of guided waves could be done by several approaches. The first option would be to determine the feature spaces for each state using an analytical or numerical model [82]; examples have been given which compare single-location model features to detect damage [56,83]. However, the problem of using this approach is in the requirement of an accurate physical model, which aligns well with the system being evaluated. For fibre-composite materials, as discussed above, determining an accurate model can be difficult. Furthermore, as only features are used, it may be advantageous for computational resources to only generate a model of the features, rather than a full wave-propagation model.

An alternative approach would be to collect experimental data and use a machine-learning algorithm to determine an empirical feature space [84]. One such example of which was shown by Legendre [85], where an artificial neural network (ANN) was used to classify wavelet-based features from wave signals in numerous damage states. Another example was shown by Su [86], and Lu [87], in which they, again, used an ANN to identify cracks in plates, although finite element modelling was used here rather than experimental data.

Machine learning (ML), has become a popular tool for learning relationships which are highly complex and difficult to describe analytically. The capability and power of ML methods has given rise to the increased use of such methods [88], particularly in SHM [89]. However, in their applications to NDE and SHM, there is an often-overlooked flaw; they will generally mean that data on all possible states must be collected for a reasonable detection regime.

This discussion leads on to the concept of *physics-informed machine learning* of feature spaces for NDE/SHM. Prior knowledge of the physics involved in the problem can be used to 'guide' the learning of the model, and has been shown to be useful for applications such as parameter estimation [90,91]. Gaussian processes (GP) offer a useful approach to learning difficult models, and have been shown to be a powerful tool for SHM applications [92]. The methodology and mathematics behind GPs also allow for elegant methods of incorporating physics via kernel design [93,94].

2.4 Guided wave interactions with damage

The interaction of Lamb waves with local inhomogeneities is well studied and the effects are well documented [61]. Almost intuitively, when a Lamb wave interacts with damage, it will reflect and scatter in directions other than its original propagation direction collinear with the actuation source and the damage. UGWs are exhibited in multiple ‘modes’, and the reflection of UGWs when interacting with damage varies between these modes, and is dependent on the relation between wavelength and damage size [95, 96]. A particular phenomenon that occurs when Lamb waves interact with damage is that of *mode conversion* [61], where modes are converted into others as a result of variations in plate dimensions. This phenomenon is directly linked to the reflection characteristics of the interaction.

Numerical modelling of Lamb wave interaction with damage is possible, and the LISA method mentioned above has been shown to perform well for this [70, 82, 97]. These works show that, when developing and testing a methodology for Lamb wave application to damage detection, numerical models are an appropriate approach. A comparative review of state-of-the-art modelling methodologies for damage in composites has been made by Orifici *et al*˙ [98], in which they discuss many issues such as length scales and implicit modelling.

2.5 Localisation

There has been evidence of useful techniques for damage localisation that do not require decomposition, such as via the use of piezoelectric rosettes [99]; however, the cost of using such hardware may quickly rise for large-scale structures. A novel method has been proposed by Rebillat *et al.*, involving the decomposition of three-way tensors constructed from ‘actuator’, ‘sensor’ and ‘time dimensions’ that shows robustness [100]. However, this method requires that data are collected from multiple actuation sources and sensor locations, so it may be advantageous in some systems to be able to localise using fewer such locations, thus reducing data usage and processing time. Methods that do not require decomposition of measured signals, such as the ones mentioned here, use either costly equipment or are computationally expensive; consequently, there is an opportunity for a computationally-efficient strategy, involving simple equipment, to be developed.

After decomposition of Lamb wave signals into direct/nominal and reflected waves, the reflected wave signal can be treated as a new wave source; where the time of the reflection occurrence and distance of the damage from each sensor is *unknown*. After formulating the problem in this way, methods of localisation vary depending on the prior information known of the system [101, 102]. Common practice for localisation of unknown initiation time is relatively simple, involving the difference in time of arrival of the wave between sensors at known locations [101]. As numerical solutions of the Lamb waves give prior information on the wave velocity, given a frequency, the localisation step becomes a simple computation problem. However, for situations where the wave speed is unknown, localisation is still possible using an iterative optimisation procedure [102]. As the decomposition strategy used here is designed for application to complex geometries and materials, it is important to also consider localisation in situations where confidence in prior wave velocity is limited. For such situations, it may be useful to take a probabilistic approach, such as in [103] and [104]. Using such an approach would also allow for quantification of the uncertainty in location, an important metric to consider in NDE or SHM strategies.

2.6 Lamb-wave signal decomposition

For damage localisation using Lamb waves, the received signal must be decomposed into all waves and wave modes within the wave-packet, in order to determine which of the superposition of signals represents the reflected wave. Decomposition of Lamb waves can be separated into two main categories; full-field decomposition, which uses data along the propagation in one or more directions, or single-source decomposition which can be applied to the received signal at a single location. Previously, full-field decomposition has been done in the frequency-wavenumber space [105], where the wave propagation is represented in the form of dispersion curves.

Some multi-mode decomposition techniques have been proposed with a variety of approaches. One such approach is a parameter-based iterative procedure to match the shape of the wave with the physical equations governing a Lamb wave in homogeneous materials [106]. Other methods involve the identification of ratio features from signal processing of the received signal [107]; however, this relies on an accurate physical model and has so far only been shown on isotropic materials. Another method involves using concentric ring and circular PZTs [108], but some drawbacks are; increased equipment cost of sensors, lack of, or more complex, actuation from such concentric sensors, meaning limited sensor-actuator array capabilities.

Many current individual-signal decomposition methods require accurate previous models of guided-wave propagation in the material being inspected, and analytical models of which are difficult to attain accurately for complex materials. Such an example would be for fibre-matrix composites, where the attenuation varies with respect to fibre-orientation. Therefore, there is an apparent need for a method for single-source, multi-mode decomposition, that only requires prior data on Lamb wave propagation in an arbitrary material.

2.7 Determining dispersion characteristics

A particular characteristic of guided waves is their dispersion, and information of this phenomenon is used frequently in guided-wave research and application. As the propagation velocity of guided waves is dependent on the wave mode and frequency, a wave-packet of mixed waves will spread out in space and time – this is known as *dispersion*. More information on dispersion, and how to determine this information, is given in Chapter 3. Therefore, accurate determination of solutions for dispersion curves for a given material/structure is key to their application in NDE/SHM regimes. Solutions of dispersion curves for isotropic materials are a simple numerical procedure [37]; however, the solutions for complex materials are more difficult.

There is no standard model for anisotropic materials, though many are available. An approach by Solie and Auld [109], attempts to derive the equations using the partial-wave technique, which aims to provide a solution for wave propagation in anisotropic media. This method assumes that the Lamb wave can be formulated as the superposition of three upward and three downward waves, each of which are referred to as partial waves. Traditionally, matrix formulations are used to retrieve wave propagation characteristics for a given frequency [53]. Both these methods have a high computational cost.

An issue is still present in the requirement of accurate information *a priori*; in this case, the elastic constants must be known for the material. When this information is not known, an accurate prior model of dispersion characteristics is difficult to obtain. For an arbitrary material, the evident next step is to determine measurements of the dispersion curve. One potential method is by the use of a ‘Matrix Pencil’ method [110], which forms an eigenvalue problem on either the frequency-time or wavenumber-distance space, of which the eigenvalues are used to determine the wavenumber or frequency respectively. However, the results shown lacked accuracy in comparison to analytical and standard method results, especially for the symmetric mode, and for regions in the curve where multiple modes coincide.

From the governing equations, the dispersion curves are defined by these elastic constants, the number of which can become extensive for anisotropic and/or inhomogeneous materials. It follows then, that information on the dispersion curves may allow for inference of these material properties. An example of this has been shown using a genetic algorithm to estimate the elastic constants of a fibre-composite plate using dispersion curves [111]; this generated feasible elastic constants and a distribution based on an assumed Gaussian posterior. This assumption of the posterior shape is a shortcoming of the approach, as well as the absence of any possible inference on the cross-correlation between material properties. In addition, the genetic algorithm has a high computational cost [112].

2.8 Summary of literature

It is clear from the literature that the use of ultrasonic guided waves for damage detection in fibre-composite requires development of more tools for their application. The modelling of UGWs in fibre-composites is difficult and costly, and can be difficult to adapt to multiple material/geometry types. This issue led to the aim of the tools developed to be generalisable approaches which, though applied specifically here, are easily adaptable to the other complex materials/geometries.

The aim of this thesis is to present a number of unique tools that have been developed for advancing the use of ultrasonic guided waves in fibre-composite structures. The approaches use a probabilistic approach, as these methods lend themselves well to a damage-detection strategy, as the quantified uncertainty can be propagated through each stage of the strategy. In the rest of the thesis, the motivation behind the methodology or tool being presented is discussed at the beginning of each chapter.

3

ULTRASONIC WAVES

For the application of ultrasonic waves in the fields of non-destructive evaluation and structural health monitoring, prior knowledge of their behaviour is essential. Such waves undergo an interesting phenomenon when they occur in particular structures, such as rods, hollow cylinders and plates; they propagate primarily in the longitudinal direction perpendicular to oscillation and are known as guided waves. When such waves are guided via propagation along the surface of a medium, they are known as *Rayleigh* waves. However, if a wave travels in a bounded medium, between two surfaces, where the wavelength is sufficiently long compared to the distance between these surfaces, often exhibited in plates, it is called a *Lamb* wave [50–52]. This chapter aims to provide a general background for ultrasonic waves in isotropic and anisotropic media, with some information on modelling techniques that are used throughout this thesis.

3.1 Bulk waves

The coordinate system for the following description of bulk waves is shown in Figure 3.1. The equation of motion for an elastic medium can be derived from Newton's second law [113], and if the body forces are neglected, the equation can be

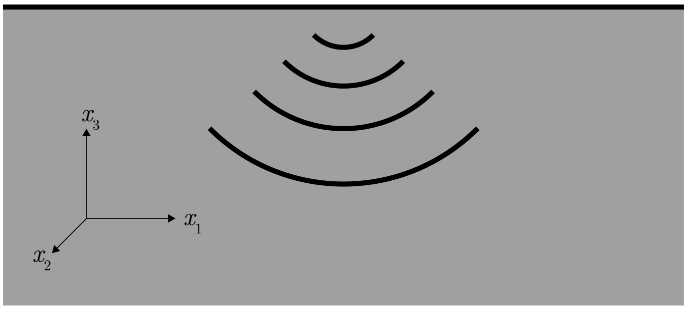

Figure 3.1: Coordinate system for bulk waves in an arbitrary medium.

expressed as [114],

$$\rho \frac{\partial^2 u_i}{\partial t^2} = \frac{\partial \sigma_{ij}}{\partial x_{ij}} \tag{3.1}$$

where i, j refers to the three dimensions in Cartesian space, $i, j = 1, 2, 3$, u_i is the particle displacement in the x_1, x_2, x_3 directions respectively, σ_{ij} is the stress field tensor element and ρ is the density of the material. According to the generalised Hooke's law, the stress σ_{ij} of a given material is proportional to the stiffness tensor C_{ijkl} and the strain ε_{ij},

$$\sigma_{ij} = C_{ijkl}\varepsilon_{kl} \tag{3.2}$$

where $i, j, k, l = 1, 2, 3$ and the strain tensor ε_{ij} is linked to the displacement u by,

$$\varepsilon_{ij} = \frac{1}{2}\left(\frac{\partial u_i}{\partial x_j} + \frac{\partial u_j}{\partial x_i}\right) \tag{3.3}$$

where $i, j = 1, 2, 3$. By including the stress symmetry $\sigma_{ij} = \sigma_{ji}$ and strain symmetry $\varepsilon_{ij} = \varepsilon_{ji}$, the stiffness tensor derives similar symmetry expressions; $C_{ijkl} = C_{jikl}$ and $C_{ijkl} = C_{ijlk}$ respectively. Additionally, the following matrix notation is defined using Voigt notation,

$$[\sigma] = \begin{bmatrix} \sigma_{11} \\ \sigma_{22} \\ \sigma_{33} \\ \sigma_{23} \\ \sigma_{13} \\ \sigma_{12} \end{bmatrix}, \quad [\varepsilon] = \begin{bmatrix} \varepsilon_{11} \\ \varepsilon_{22} \\ \varepsilon_{33} \\ 2\varepsilon_{23} \\ 2\varepsilon_{13} \\ 2\varepsilon_{12} \end{bmatrix} \tag{3.4}$$

For arbitrary anisotropic materials, the generalised Hooke's law, implying the stress-strain relation, can be written in the following form,

$$\begin{Bmatrix} \sigma_{11} \\ \sigma_{22} \\ \sigma_{33} \\ \sigma_{23} \\ \sigma_{13} \\ \sigma_{12} \end{Bmatrix} = \begin{bmatrix} C_{11} & C_{12} & C_{13} & C_{14} & C_{15} & C_{16} \\ & C_{22} & C_{23} & C_{24} & C_{25} & C_{26} \\ & & C_{33} & C_{34} & C_{35} & C_{36} \\ & & & C_{44} & C_{45} & C_{46} \\ & & & & C_{55} & C_{56} \\ & & & & & C_{66} \end{bmatrix} \begin{Bmatrix} \varepsilon_{11} \\ \varepsilon_{22} \\ \varepsilon_{33} \\ 2\varepsilon_{23} \\ 2\varepsilon_{13} \\ 2\varepsilon_{12} \end{Bmatrix} \tag{3.5}$$

where $C_{kl}(k, l = 1, 6)$ identifies the stiffness matrix and represents the elastic constant of the anisotropic medium.

3.1.1 Isotropic media

For an isotropic medium, Hooke's law can be written as,

$$\sigma_{ij} = \lambda\delta_{ij}\varepsilon_{kk} + 2\mu\varepsilon_{ij} \tag{3.6}$$

where δ_{ij} is the Kronecker delta and λ, μ are the Lamé constants, which are related to the stiffness tensor by,

$$C_{12} = C_{13} = C_{21} = C_{23} = C_{31} = C_{32} = \lambda \tag{3.7}$$

$$C_{44} = C_{55} = C_{66} = \mu \tag{3.8}$$

$$C_{11} = C_{22} = C_{33} = \lambda + 2\mu \tag{3.9}$$

The Lamé constants can be expressed in terms of the more common Young's modulus E, Poisson's ratio ν and bulk modulus μ.

$$E = \frac{\mu(3\lambda + 2\mu)}{\lambda + \mu} \tag{3.10}$$

$$\nu = \frac{\lambda}{2(\lambda + \mu)} \tag{3.11}$$

By substituting these relations into the elastodynamic equation (3.1), it can be expressed as,

$$\rho\frac{\partial^2 u_i}{\partial t^2} = (\lambda + \mu)\frac{\partial \Delta}{\partial x_i} + \mu\nabla^2 u_i \tag{3.12}$$

where $i, j = 1, 2, 3$, $\Delta = \varepsilon_{11} + \varepsilon_{22} + \varepsilon_{33}$ and ∇^2 is defined as,

$$\nabla^2 = \frac{\partial^2}{\partial x_1^2} + \frac{\partial^2}{\partial x_2^2} + \frac{\partial^2}{\partial x_3^2} \tag{3.13}$$

Solutions to equation (3.12), give two different propagation velocities, which correspond to the longitudinal and shear waves, the first of which represents motion where no rotation takes place and the second represents motion where no change in the volume of a unit cube (or dilatation) occurs. The relation between the velocities of these waves and the Lamé constants is,

$$\lambda = \rho c_L^2 - 2\mu \tag{3.14}$$

$$\mu = \rho c_T^2 \tag{3.15}$$

where c_L and c_T are the propagation velocities of the longitudinal and shear waves respectively.

3.2 Lamb Waves

When a wave travels in a bounded medium, the boundary conditions can be applied to produce some neat descriptions of the physics. In bounded media, these waves will exhibit as Lamb waves, which in isotropic elastic media will exhibit two distinct modes: *symmetric* (S) and *antisymmetric* (A). For anisotropic media, an additional shear horizontal (SH) mode will propagate, where particle motion is in the same direction as propagation. The model that describes the governing equations is shown here and follows the free-plate problem as described in [52]. For the purposes of this problem, the coordinates are defined as in Figure 3.2.

Via steps provided in [52], the equations to describe particle motion on the surface of an isotropic plate can be developed. There are two types of solutions available, in the first, the in-plane displacement u_1 is an even function of u_3; such solutions are called *symmetric*. When u_1 is an odd function of u_3, the *antisymmetric* solutions are returned.

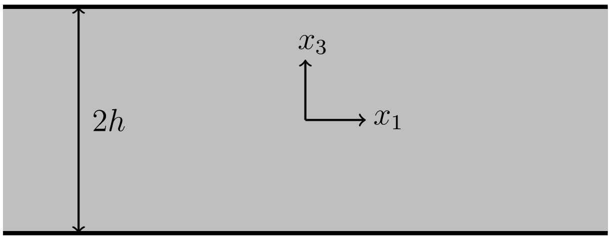

Figure 3.2: Coordinate system and dimensions for Lamb waves in a plate of thickness $2h$

Where $A_{1,2}$ and $B_{1,2}$ are arbitrary constants, and x_3 is the distance from the centre of the plate, for symmetric modes one has [52],

$$u_1 = ikA_2\cos(px_3) + qB_1\cos(qx_3) \tag{3.16a}$$

$$u_3 = -pA_2\sin(px_3) - ikB_1\sin(qx3) \tag{3.16b}$$

and for antisymmetric modes,

$$u_1 = ikA_1\sin(px_3) - qB_2\sin(qx_3) \tag{3.17a}$$

$$u_3 = pA_1\cos(px_3) - ikB_2\cos(qx3) \tag{3.17b}$$

where,

$$p = \frac{\omega}{\sqrt{c_L^2 - c^2}}, \qquad q = \frac{\omega}{\sqrt{c_T^2 - c}} \tag{3.18}$$

where $2h$ is the plate thickness, k is the real wavenumber, ω is the central frequency, c is the material bulk wave speed, c_L is the longitudinal wave speed and c_T is the transverse wave speed. For guided waves in isotropic materials, the bulk wave speed is equal to the *phase velocity*, $c_p = c$ and the wavenumber is equal to $k = \omega/c_p$.

After applying the boundary conditions $\sigma_{31} = \sigma_{33} = 0$ at $x_3 = \pm h$, two characteristic equations are formed for Lamb waves which describe their behaviour in given media:

$$\frac{\tan(qh)}{\tan(ph)} = -\frac{4k^2pq}{(q^2-k^2)^2} \tag{3.19}$$

for the symmetric modes and,

$$\frac{\tan(ph)}{\tan(qh)} = -\frac{4k^2pq}{(q^2-k^2)^2} \tag{3.20}$$

for the antisymmetric modes. These equations are known as the Rayleigh-Lamb frequency relations. It should be noted that these equations will only hold for isotropic materials, approaches to deriving the governing equations of anisotropic materials are discussed later.

3.3 Dispersion

This section will introduce the concept of dispersion by explanation with respect to isotropic materials, solutions for dispersion curves in anisotropic materials will be presented in Section 3.5. Given a value of ω, equations (3.19) and (3.20) specify allowed values of c for either mode; as c is a function of ω this means that the waves will spread out in space and time – i.e. they are *dispersive*. As ω only enters into equations (3.19) and (3.20) as a product with h, dispersion curves are often presented in terms of the *frequency-thickness product* (FTP). Solutions to these equations are determined numerically, and plots of the wave velocity with respect to frequency-thickness are called *dispersion curves*. In order to generate dispersion curves in relation to the *phase velocity* c_p, the governing equations (3.19) and (3.20) are rearranged as,

$$\frac{\tan(qh)}{q} + \frac{4k^2 p \tan(ph)}{(q^2 - k^2)^2} = 0 \tag{3.21}$$

for the symmetric modes and,

$$q \tan(qh) + \frac{(q^2 - k^2)^2 \tan(ph)}{4k^2 p} = 0 \tag{3.22}$$

for the antisymmetric modes. The steps for generating dispersion curves are,

1. Choose frequency-thickness $(\omega h)_0$.
2. Make an initial estimate of the phase velocity $(c_p)_0$.
3. Evaluate the left-hand side of equation (3.21) or equation (3.22).
4. Choose another phase velocity $(c_p)_1 > (c_p)_0$ and re-evaluate the sign of equation (3.21) or equation (3.22).
5. Repeat Steps 3 and 4 until the sign changes. As the function is continuous, a change in sign between phase velocities $(c_p)_n$ and $(c_p)_{n+1}$ indicates the root is between these values.

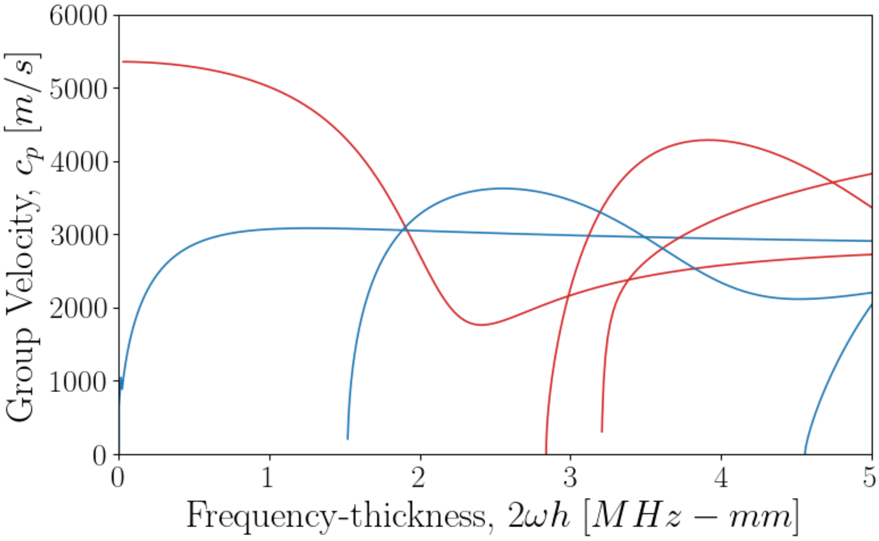

Figure 3.3: Dispersion curves for the group velocity of a 1mm-thick aluminium plate, calculated using DISPERSE software [117]. The blue lines indicate the antisymmetric A_n modes, and the red lines indicate the symmetric S_n modes, with the order they appear along the x-axis being the order n of the mode. The aluminium plate is modelled with density of 2710 kg/m^3, $c_L = 6.42$ m/ms & $c_T = 3.04$ m/ms.

6. Use an iterative root-finding algorithm such as Newton-Raphson [115] or Secant methods [116], to locate precisely the phase velocity in the interval $(c_p)_n < c_p < (c_p)_{n+1}$.
7. Chose another frequency-thickness $(\omega h)_n$ and repeat Steps 2 to 6.

From the phase velocity, the wave number and group velocity can be determined using the relations,

$$k = \frac{\omega}{c_p} \tag{3.23}$$

$$c_g = \frac{d\omega}{dk} \tag{3.24}$$

Software packages are available to calculate these solutions and generate numerically-determined dispersion curve information – an example being *DISPERSE* [117]. An example of dispersion information determined using this method is shown in Figure 3.3.

Dispersion curves can also be determined from experimental regimes by the use of a *two-dimensional Fourier transform* (2DFT); this is done by recording the surface displacement of a Lamb wave, spatially sampled along its propagation path, to generate the time-distance [t-x] space. Passing this through a 2DFT then provides a transformation to the frequency-wavenumber [ω-k] space [118].

Typical presentations of dispersion curves are as the relation of FTP to *group velocity*, *phase velocity* or *wavenumber*. For this thesis, the group velocity and wavenumber dispersion curves are important, as the group velocity is required for triangulation of reflection signals, and the [ω-k] curve is the type generated by experiment.

Dispersion curves are regularly used in guided-wave application, as knowledge of the wave velocity is required for wave source localisation, and wavenumber characteristics can be used as features for detection regimes. Lamb waves often propagate with multiple modes – a minimum of two – which causes a problem for practical application as the separation of these modes may be necessary for proper determination of reflected waves. As a result of the dispersive nature of Lamb waves, they will arrive at a sensor at different times, which may make the signal processing again more difficult. By the use of tuned actuation techniques, it is possible to excite individual modes, although these are often more expensive, and exciting multiple modes can provide more information on the structure.

3.4 Attenuation of guided waves

The attenuation of Rayleigh waves can be defined fairly simply. As Rayleigh waves propagate along a surface of a structure, their amplitude A, decays with propagation distance [50], x, by

$$A(x) \propto \frac{1}{\sqrt{k_R x}} \tag{3.25}$$

where k_R is the real wavenumber. The attenuation of Lamb waves depends on many factors, although Pollock [74] states the four most important ones to be:

(i) geometric spreading (as above),

(ii) material damping,

(iii) dissipation into adjacent media,

(iv) wave dispersion,

Attenuation of Lamb waves has been accurately modelled by the inclusion of proportional damping in numerical and experimental studies [119, 120]. Geometric spreading describes the loss of amplitude because of the growing length of a wave front departing in all directions from a source. The effect of propagation distance on the amplitude of the wave has been described for geometric spreading [120],

$$A(r) \propto A_0 \sqrt{r_0/r} \tag{3.26}$$

where A_0 & r_0 are the amplitude and distance at an initial location from a point source. It should be noted that for fibre-reinforced materials, attenuation of waves propagating along fibre-rich directions is reduced in geometric spreading. Material damping [37], describes how much energy stored in the wave dissipates because of non-perfect elastic material behaviour. Fibre-reinforced materials exhibit much larger material damping than metallic structures. Attenuation from material damping is described as,

$$A(r) \propto A_0 \exp\left(-\zeta_i r\right) \tag{3.27}$$

where ζ_i is the attenuation coefficient of the viscoelastic medium. Because of dispersive characteristics of Lamb waves, ζ_i is dependent on the central frequency of the wave. Two relatively-simple attenuation mechanisms have been introduced here, and will be used in Chapter 5, as these are the fundamental mechanisms which are found to be exhibited in every material. If wishing to model multiple attenuation mechanisms, the method of combination is important. An additive (or subtractive) combination would imply that each mechanism acts independently to each other and only relies on the initial amplitude. However, a multiplicative combination would imply the attenuation mechanisms act in conjunction, and so the amplitude is considered along the entire propagation path.

3.5 Guided waves in anisotropic media

The study of guided-wave propagation in anisotropic media has attracted a lot of attention recently because of its growing use in state-of-the-art industrial applications.

However, modelling guided-wave phenomena in complex materials is much more difficult than for isotropic materials because of their anisotropy resulting in more complicated phenomena.

Following discussions made earlier on the methods proposed for modelling Lamb wave characteristics of anisotropic media, the work of Lefebvre [79] is described here for determining dispersion curves of anisotropic media. This method uses a Legendre polynomial expansion to form an eigenvalue problem, utilising the orthonormal basis set for expansion of the field quantities. For orthotropic materials, the generalised Hooke's law (equation (3.5)), can be rewritten as,

$$\begin{Bmatrix} \sigma_{11} \\ \sigma_{22} \\ \sigma_{33} \\ \sigma_{23} \\ \sigma_{13} \\ \sigma_{12} \end{Bmatrix} = \begin{bmatrix} C_{11} & C_{12} & C_{13} & 0 & 0 & 0 \\ & C_{22} & C_{23} & 0 & 0 & 0 \\ & & C_{33} & 0 & 0 & 0 \\ & & & C_{44} & 0 & 0 \\ & & & & C_{55} & 0 \\ & & & & & C_{66} \end{bmatrix} \begin{Bmatrix} \varepsilon_{11} \\ \varepsilon_{22} \\ \varepsilon_{33} \\ 2\varepsilon_{23} \\ 2\varepsilon_{13} \\ 2\varepsilon_{12} \end{Bmatrix} \tag{3.28}$$

The boundary conditions of zero stresses on the surface can be applied by introducing a rectangular window function $\pi_h(x_3)$,

$$\pi_h(x_3) = \begin{cases} 1 & 0 \leq x_3 \leq h \\ 0 & \text{otherwise} \end{cases} \tag{3.29}$$

the above-mentioned boundary conditions are automatically incorporated in the constitutive relations, and by substituting in the relationship of the strain (equation (3.3)), and transforming the spatial coordinates into dimensionless form q_α,

$$q_\alpha = kx_\alpha, \qquad (\alpha = 1, 3) \tag{3.30}$$

then the constitutive relations are,

$$\sigma_{ij} = \left(C_{ijkl} \frac{\partial u_l}{\partial q_k} \right) k\pi_h(q_3) \tag{3.31}$$

For a wave propagating in the x_1 direction, the displacement components are assumed to be of the form,

$$u_i(q_1, q_2, q_3, t) = U_i(q3)e^{i(q_1 - \omega t)} \tag{3.32}$$

where the $U_i(q_3)$ represent the magnitudes of the fields in the x_i direction. Substituting equations (3.31) and (3.32) into equation (3.1) gives,

$$\begin{aligned}-\frac{\omega^2}{k^2}U_1 =& -U_1\frac{C_{11}}{\rho} + iU_3'\left(\frac{C_{13}+C_{55}}{\rho}\right) + U_1''\frac{C_{55}}{\rho}\\ &+ iU_3\frac{C_{55}}{\rho}\left(\delta(q3)-\delta(q3=kh)\right) + U_1'\frac{C_{55}}{\rho}\left(\delta(q3)-\delta(q3=kh)\right)\end{aligned} \tag{3.33a}$$

$$-\frac{\omega^2}{k^2}U_2 = -U_2\frac{C_{66}}{\rho} + U_2''\frac{C_{44}}{\rho} + U_2'\frac{C_{44}}{\rho}\left(\delta(q3)-\delta(q3=kh)\right) \tag{3.33b}$$

$$\begin{aligned}-\frac{\omega^2}{k^2}U_3 =& -U_3\frac{C_{55}}{\rho} + iU_1'\left(\frac{C_{31}+C_{55}}{\rho}\right) + U_3''\frac{C_{33}}{\rho}\\ &+ iU_1\frac{C_{13}}{\rho}\left(\delta(q3)-\delta(q3=kh)\right) + U_3'\frac{C_{55}}{\rho}\left(\delta(q3)-\delta(q3=kh)\right)\end{aligned} \tag{3.33c}$$

where the superscript $(\cdot)'$ refers to the partial derivative with respect to q_3. It is clear to see that equation (3.33b) is independent of equations (3.33a) and (3.33c); in fact, equation (3.33b) represents the vibration of the SH waves in the orthotropic viscoelastic plates and equations (3.33a) and (3.33c) control propagation of Lamb-wave modes.

In order to solve the decoupled wave equations, the Legendre polynomial method expands $U_i(x_3)$ over an orthonormal-polynomial basis [79–81],

$$U_i(q_3) = \sum_{m=0}^{\infty} p_m^i Q_m(q_3), \qquad i = 1, 2, 3 \tag{3.34}$$

where p_m^i is the expansion coefficient and,

$$Q_m(q_3) = \sqrt{\frac{2m+1}{kh}}P_m\left(\frac{q_3}{kh}-1\right) \tag{3.35}$$

where $P_m(x)$ is the Legendre polynomial expansion of order m. Theoretically, m runs from 0 to ∞; however in practice, the summation over polynomials in equation (3.34) can be halted at some finite value of $m = M$, when higher-order terms become negligible.

To retrieve the final equations to be solved, one substitutes equations (3.34) and (3.35) into equation (3.33), multiplies by $Q_j^*(q_3)$ and integrates over q_3 from 0 to kh, giving,

$$\frac{\omega^2}{k^2}p_m^1 = -M_{jm}^{-1}\left[A_{11}^{jm}p_m^1 + A_{13}^{jm}p_m^3\right] \tag{3.36a}$$

$$\frac{\omega^2}{k^2}p_m^2 = -M_{jm}^{-1}\left[A_{22}^{jm}p_m^2\right] \tag{3.36b}$$

$$\frac{\omega^2}{k^2}p_m^3 = -M_{jm}^{-1}\left[A_{31}^{jm}p_m^1 + A_{33}^{jm}p_m^3\right] \tag{3.36c}$$

with j and m running from 0 to M, and $(\cdot)^*$ means the complex conjugate. The definitions of the matrix elements are given in **??**.

By separating out equation (3.36) into only the coupled Lamb-wave modes and decoupled SH wave mode, the final solution can be arranged as an eigenvalue problem,

$$\begin{bmatrix} A_{11}^{jm} & A_{13}^{jm} \\ A_{31}^{jm} & A_{33}^{jm} \end{bmatrix} \begin{bmatrix} p_m^1 \\ p_m^3 \end{bmatrix} = -\frac{\omega^2}{k^2}M_{jm}\begin{bmatrix} p_m^1 \\ p_m^3 \end{bmatrix} \tag{3.37a}$$

$$\left[A_{22}^{jm}\right]p_m^2 = -\frac{\omega^2}{k^2}M_{jm}p_m^2 \tag{3.37b}$$

with eigenvalues $\lambda_i - c_{p,i}^2$ and corresponding eigenvectors $\{p_m^1, p_m^3\}_i^\top$. Here, $3(M+1)$ eigenmodes are generated at the order M of the expansion. The solutions to be accepted are only those eigenmodes for which convergence is obtained as M is increased [79–81].

Previous studies on this Legendre-polynomial expansion approach showed the accuracy and rigour of the method, including the ability to determine the through-thickness mode shapes by determining the values of the eigenvectors. This method's low computational-cost gives it promising application for modelling of guided waves in complex materials, in particular as it uses the stiffness tensor elements allowing for dull definition of the material in question. The next steps of research using this method would be to implement the approach using an unreduced stiffness tensor for fully asymmetric materials.

3.6 LISA Simulation

A proven-robust method for simulating guided waves in plates has been shown using the *local interaction simulation approach* (LISA), a particular advantage of which is that it captures multi-mode interactions well. For this reason, the approach was used in this work (shown in Chapter 6), and a short introduction will be given here. The LISA simulation method uses iterative difference equations and is based on a sharp-interface model. This allows LISA to incorporate the effects of boundaries and inhomogeneities with ease – a primary benefit of using the method – as well as faster computing time in comparison to finite-element analysis (FEA). The application of LISA to the simulation of guided waves is well documented [69, 70, 72]. A key difference between this method and standard finite-difference (FD) approaches is that LISA solves a discrete form of equation (3.1) exactly, modelling physical phenomena without other approximations, whereas the FD is a solution of the partial differential equation after discretisation.

A finite-difference formulation is used in equation (3.1) to generate spatial and temporal iterative equations that can be applied for a given point in space. For LISA simulation of orthotropic media with in-plane rotation (such as fibres), the stiffness tensor from equation (3.1) is often expressed in terms of stress and Lamé parameters [71, 72],

$$C = \begin{pmatrix} C_{11} & C_{12} & C_{13} & 0 & 0 & C_{16} \\ C_{12} & C_{22} & C_{23} & 0 & 0 & C_{26} \\ C_{13} & C_{23} & C_{33} & 0 & 0 & C_{36} \\ 0 & 0 & 0 & C_{44} & C_{45} & 0 \\ 0 & 0 & 0 & C_{45} & C_{55} & 0 \\ C_{16} & C_{26} & C_{36} & 0 & 0 & C_{66} \end{pmatrix} = \begin{pmatrix} \sigma_1 & \lambda_6 & \lambda_5 & 0 & 0 & \tau_{16} \\ & \sigma_2 & \lambda_4 & 0 & 0 & \tau_{26} \\ & & \sigma_3 & 0 & 0 & \tau_{36} \\ & & & \mu_4 & \gamma_{45} & 0 \\ & & & & \mu_5 & 0 \\ & & & & & \mu_6 \end{pmatrix} \tag{3.38}$$

First, the system is discretised into evenly-sized cells and these cells are considered as a series of springs and masses which populate the medium. At any point, which is neighboured by eight cells, the sharp-interface model is used to average the properties of the neighbouring cells. It is assumed at each point, that the material properties and displacements are continuous, whereas interfaces of cells are treated as discontinuous.

As the LISA simulation is not the focus of this work, detailed information on the method and the final equations are given in **??**. The main considerations of LISA simulation is the limit of computer memory, and so only small simulations can be considered for now. However, the main advantage of LISA is that there are few limitations on the material type, as the governing equations stem directly from the stiffness tensor. So, as less sparse stiffness matrices simply result in more laborious, but no less difficult, derivation of the final equations, model reduction and simplification is by reduction of the stiffness tensor.

4

MACHINE LEARNING TECHNIQUES

As discussed previously, the physics of guided waves in fibre-composite materials becomes complex, and it is difficult to generate accurate analytical or numerical models that are easily updated (though this does not discredit their capability, as is seen in later chapters). So in this work, machine-learning techniques are used in a variety of ways to model wave propagation in fibre-composite materials. In this chapter, some background is provided on two of the primary machine-learning techniques used in this work; *Bayesian linear regression* and *Gaussian processes*. These are both methods that attempt to 'learn' the mapping between an input and output space.

The methods outlined in this work follow the format of Bayesian probability theory. To illustrate these methods it useful to discuss some definitions. Firstly, there is the *prior* and *posterior* probability distributions; the former of which is the distribution that is believed to describe the data before any evidence is provided. The posterior distribution is that which is determined with proper evidence and background information. An *uninformative prior* is one which gives vague information of the probabilities, and is useful when prior knowledge is not available. When the posterior distributions belong to the same family as the prior distributions, these are known as *conjugate distributions*, and the prior is called a *conjugate prior*. Finally, the *likelihood* expresses how likely a particular value or set of values is, given the statistical parameters, and is a useful tool for determining the best estimates of unknown parameters or models. As well as the above definitions, it is useful to introduce Bayes' rule [121]; this provides a way of updating one's belief based on new, relevant pieces of evidence. If A is the event one wishes to know the probability of, and B is the new evidence, Bayes' rule states that the posterior $P(A|B)$ is dependent on the likelihood $P(B|A)$, the prior $P(A)$ and the marginal likelihood $P(B)$ via,

$$P(A|B) = \frac{P(B|A)P(A)}{P(B)} \tag{4.1}$$

4.1 Bayesian Linear Regression (BLR)

Traditional linear regression formulates a model using point estimates of a set of parameters which "best" fit an available dataset, based on minimising an L^2-norm between the model predictions and the data. Instead, BLR aims to establish a probability distribution of possible model parameters. This method is often used when the model is either linear or 'linear-in-the-parameters', and so it is simple and efficient to recover both the estimate of the mean and the variance (uncertainty) in the model. For models where linearity in the model is not possible, more complex methods and algorithms can be used such as neural networks [122], or spline regression [123]. BLR is used here as the models used are simple to define in linear terms, and so recovering probabilistic quantities is simpler and computationally efficient to do. The model has the form,

$$y = \mathbf{w}^{\top}\phi(\mathbf{x}) + \varepsilon, \qquad \varepsilon \sim \mathcal{N}(0, \sigma^2) \tag{4.2}$$

where ϕ is some basis for expansion of a p-dimensional data point $\mathbf{x}$; the associated weights of the basis expansion are $\mathbf{w} = \{w_1, w_2, ..., w_p\}$, and ε is an additive Gaussian white noise distributed as $\mathcal{N}(0, \sigma^2)$. The weights $\mathbf{w}$ and the variance σ^2 are the unknowns. The Bayesian linear regression model approach was chosen since it returns a quantified uncertainty. The task is then to compute the posterior distribution of the parameters $p(\mathbf{w}, \sigma^2|D)$. This posterior distribution has the form,

$$p(\mathbf{w}, \sigma^2|\mathcal{D}) = NIG(\mathbf{w}, \sigma^2|\mathbf{w}_N, \mathbf{V}_N, a_N, b_N) \tag{4.3}$$

where NIG is the *normal-inverse-gamma* distribution. And the parameters are defined by,

$$\mathbf{w}_N = \mathbf{V}_N(\mathbf{V}_0^{-1}\mathbf{w}_0 + \mathbf{X}^\top\mathbf{y}) \tag{4.4}$$

$$\mathbf{V}_N = (\mathbf{V}_0^{-1} + \mathbf{X}^\top\mathbf{X})^{-1} \tag{4.5}$$

$$a_N = a_0 + n/2 \tag{4.6}$$

$$b_N = b_0 + \frac{1}{2}\left(\mathbf{w}_0^\top\mathbf{V}_0^{-1}\mathbf{w}_0 + \mathbf{y}^\top\mathbf{y} - \mathbf{w}_N^\top\mathbf{V}_N^{-1}\mathbf{w}_N\right) \tag{4.7}$$

where $\mathbf{V}_0$, $\mathbf{w}_0$, a_0 and b_0 are hyperparameters of the prior, which are parameters used to control the learning process. It is possible to set a less-informative prior for σ^2 by applying $a_0 = b_0 = 0$. Also setting $\mathbf{w}_0 = 0$ and $\mathbf{V}_0 = g(\mathbf{X}^\top\mathbf{X})^{-1}$ for any positive value g; leads to Zellner's *g-prior* [124]. By having the prior variance proportional to $(\mathbf{X}^\top\mathbf{X})^{-1}$, it is ensured that the posterior is invariant under scaling of the inputs.

An important assessment metric that is attainable from the Bayesian linear regression method, is the *predictive likelihood*, which gives an indication of the likelihood that the model fits, and takes into account the uncertainty as well as the quality of the mean fit. In probabilistic data science, the likelihood is the calculation of the best distribution of data, given a set of observations. In this case, the likelihood is the value of probability of a predicted value, taken from the distribution of these predicted values, based on the observed data.

As this method uses a tractable Gaussian posterior, the predictive likelihood is given by,

$$p(\tilde{\mathbf{y}}|\tilde{\mathbf{x}}, \mathbf{y}, \mathbf{x}) = \mathcal{N}\left(\mathbb{E}\left[\tilde{\mathbf{y}}\right], \mathbb{V}\left[\tilde{\mathbf{y}}\right]\right) \tag{4.8}$$

where $\mathbb{E}\left[\tilde{\mathbf{y}}\right]$ and $\mathbb{V}\left[\tilde{\mathbf{y}}\right]$ are the predicted values and variance of the output, given input $\mathbf{x}$. For computational stability, this likelihood is calculated in the log space, and is named the *independent predictive log-likelihood* PLL_i and is defined by,

$$PLL_i = \sum_i^N \log \mathcal{N}(\mathbf{y}_i|\mathbb{E}[\mathbf{y}_i], \mathbb{V}[\mathbf{y}_i], \mathbf{w}) \tag{4.9}$$

for N data points. This value is the product over the predictive likelihoods for every point, i.e. the joint likelihood if they were uncorrelated.

4.2 Gaussian Processes

The Gaussian process (GP) is a flexible Bayesian regression method, which works by placing a prior over functions, which is then updated on the basis of data, to return a posterior distribution over functions [125, 126]. Conceptually, one can think of this process as estimating, rather than one "best" fit through the data, a distribution over all the possible functions that could explain the data. By virtue of its construction, the marginal and conditional distributions of any finite subset of data points in the function are Gaussian. In other words, any finite set of data modelled by the Gaussian process can be represented by a multivariate Gaussian distribution. The benefit of this result is that computations are normally available in closed form; for example, the conditional distribution of some new test points given the already observed data can be recovered exactly. The model is also *nonparametric*; the form of the function which will fit the data does not need to be specified, i.e. it is not necessary to choose a basis, such as a polynomial one. Instead, the function is modelled by representing the covariance in the data via a kernel or covariance function. This kernel is used to embed belief about which *family of functions* the data have come from, e.g. a nonlinear or periodic function.

The Gaussian process can be used to model nonlinear regression problems of the form,

$$\mathbf{y} = f(\mathbf{X}) + \boldsymbol{\varepsilon} \qquad \boldsymbol{\varepsilon} \sim \mathcal{N}(\mathbf{0}, \sigma_n^2 \mathbb{I}) \tag{4.10}$$

where $\mathbf{y}$ is a vector of N observed targets, $\mathbf{X}$ a matrix of N observed inputs in D dimensions, and ε a vector of realisations from a zero-mean Gaussian white noise process with variance σ_n^2.

A GP is fully defined by its mean and covariance functions,

$$f(\mathbf{x}) \sim \mathcal{GP}\left(m(\mathbf{x}), k(\mathbf{x}, \mathbf{x}')\right) \tag{4.11}$$

The mean function $m(\mathbf{x})$, can be any parametric mapping of $\mathbf{x}$, e.g. a polynomial. The correlation between the targets is captured by the covariance function which expresses the similarity between two input vectors $\mathbf{x}$ and $\mathbf{x}'$. To predict at a new test point $\mathbf{x}_\star$, or set of test points $X_\star$, predictive equations are used to determine the expected mean function $\mathbb{E}[f_\star]$ and expected covariance $\mathbb{V}[f_\star]$ [125],

$$f_\star \sim \mathcal{N}\left(\mathbb{E}[f_\star], \mathbb{V}[f_\star]\right) \tag{4.12a}$$

$$\mathbb{E}[f_\star] = m(\mathbf{x}_\star) + k(\mathbf{x}_\star, X)(k(X, X) + \sigma_n^2 \mathbb{I})^{-1}\mathbf{y} \tag{4.12b}$$

$$\mathbb{V}[f_\star] = k(\mathbf{x}_\star, \mathbf{x}_\star) - k(\mathbf{x}_\star, X)(k(X, X) + \sigma_n^2 \mathbb{I})^{-1}k(X, \mathbf{x}_\star) \tag{4.12c}$$

If predicting at noisy output locations, i.e. $y_\star$, it is trivial to add the noise variance $\sigma_n^2\mathbb{I}$ to the predictive covariance in equation (4.12c). As such the GP returns the posterior distribution over $f_\star$ or $y_\star$ as a Gaussian distribution.

The primary influence of the user, when implementing a GP, is in the choice of the kernel, which is calculated as any other kernel; linear pair-wise distances between points to form a covariance matrix. Careful consideration of data should also be applied in implementation, such as data type (scale, sign, etc.), data size and space on which it operates. There are a number of choices available for the kernel function, each of which embeds a different prior belief as to which *family of functions* $f(\mathbf{x})$ is drawn from. For example, if a linear kernel is used, the solution to a Bayesian linear regression is recovered. More commonly, nonlinear kernels will be chosen, as many tasks require regression of nonlinear functions; popular choices include the use of the Squared-Exponential (SE) kernel or the Matérn class of kernels. In most cases the mean function is set to zero in the prior.

4.2.1 General nonlinear kernels

It will be important to consider how the GP would model data if no restrictions were placed on it with respect to the coordinate system of the input space. Two important properties, which certain kernels possess, are stationarity and isotropy. A *stationary* kernel is only dependent upon the difference between any two points, not the absolute values of those points. An *isotropic* kernel is invariant to translation or rotation of the input data; practically, this appears as the covariance being only dependent on the absolute difference between two data points [125]. These properties will be important when discussing what is desired from a kernel to model the features of guided waves.

One such stationary and isotropic kernel, is the popular squared-exponential (SE) kernel [125]. This kernel is given by,

$$k_{\mathrm{SE}}(\mathbf{x}, \mathbf{x}') = \sigma_f^2 \exp\left\{-\frac{||\mathbf{x}-\mathbf{x}'||_2^2}{2\ell^2}\right\} \tag{4.13}$$

where ℓ is the characteristic lengthscale, and σ_f^2 is the noise variance parameter. An alternative general nonlinear kernel is the Matérn 5/2 kernel (as applied here to the radial dimension); this well-established kernel is used as it offers relatively smooth shapes and is defined as,

$$k_{\mathrm{mat}}(\mathbf{x}, \mathbf{x}') = \left(1 + \frac{\sqrt{5}|\mathbf{x}-\mathbf{x}'|}{\ell} + \frac{5|\mathbf{x}-\mathbf{x}'|^2}{3\ell^2}\right) \exp\left(-\frac{\sqrt{5}|\mathbf{x}-\mathbf{x}'|}{\ell}\right) \tag{4.14}$$

4.2.2 Applying Gaussian processes in polar coordinates

Chapter 3 provided detail on the physics and modelling of guided waves, the descriptions of characteristics such as attenuation are often expressed in terms of the wave propagation distance. As well as this, dispersive characteristics of waves means that the time-difference between wave modes within one wave-packet will depend on propagation distance. For anisotropic materials, the propagation angle has an effect on the propagation of the waves; for all propagation characteristics. From this, the description of the physics of guided wave propagation is more suitably defined in polar coordinate space. Therefore, it is useful to look at how to modify the Gaussian process to be better applied in this space.

To make this modification is not as trivial as it may seem. Remembering that the covariance function is a measure of similarity between two data points, it is necessary to define a kernel which encodes this. Specifically, it is necessary to have high covariance between points that are close to each other in angle. For example a point with angle 359° should have a high covariance with 1° if the radii are also close. This will require modifications to the kernel in terms of the distance used to assess how close together points are and also to the covariance function itself. Padonou and Roustant [127] suggest two potential definitions for a distance which fulfils this criteria, as shown in Figure 4.1(a). These two distances are: the *chordal* distance

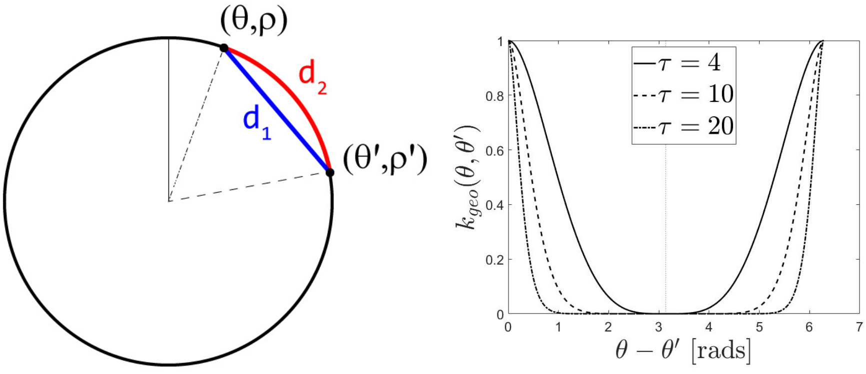

(a)

(b)

Figure 4.1: (a) Chordal (d_1) and geodesic (d_2) distances. (b) Angular covariance as a function of geodesic distance, with varying values of τ.

$d_1(\theta,\theta') = 2\sin\left(\frac{\theta-\theta'}{2}\right)$ or the *geodesic* distance $d_2(\theta,\theta') = \arccos(\cos(\theta-\theta'))$. Using these definitions, it is possible to define the covariance in the θ dimension of a $\{\rho,\theta\}$ polar coordinate system.

The C^2-Wendland function is used as the kernel, since this produces a covariance of 0 when $d_2 = \pi$ and is strictly positive when $d_2 > \pi$, both are necessary conditions for the polar kernel design. The C^2-Wendland function is defined as,

$$W_c(t) = \left(1 + \tau\frac{t}{c}\right)\left(1 - \frac{t}{c}\right)_+^{\tau}, \quad c \in [0,\pi]; \tau \geq 4 \tag{4.15}$$

When applying the Wendland function as the covariance function, the value of c must change depending on the angular distance chosen,

$$k_{\mathrm{W}} = \begin{cases} k_{chord}(\theta,\theta') = W_2(d_1(\theta,\theta')) \\ k_{geo}(\theta,\theta') = W_\pi(d_2(\theta,\theta')) \end{cases} \tag{4.16}$$

Here, the value of τ acts as a ‘steepening’ parameter on the angular covariance; this can be seen as the angular analogue to the inverse of the length-scale parameter described previously. By displaying equation (4.15) as a function of geodesic distance as in Figure 4.1(b), the effect of τ can be more clearly seen.

To form a full polar covariance function, a different kernel is applied only on the radial dimension of the input. This kernel could be any stationary isotropic kernel;

in this work the Matérn 5/2 kernel is used as in [127],

$$k_{mat} = \sigma_n^2 \left(1 + \frac{\sqrt{5}r}{\ell} + \frac{5r^2}{3\ell^2}\right) \exp\left(-\frac{\sqrt{5}r}{\ell}\right) \tag{4.17}$$

In that case the distance used in the Matérn kernel is the absolute difference between the two radial components $r = |\rho - \rho'|$. For the angular component, equation (4.15) is used with the geodesic distance such that kernel k_{geo} is used.

These choices define the covariance in the model along each of the directions - the radial ρ and the angular θ. To form the total covariance it is necessary to combine these two. It is known that the addition or pointwise multiplication of any two valid covariance functions is itself a valid covariance [125]. In this work an *ANOVA* combination [128] of the kernels in each dimension is used, as in [127]; this allows variations in each dimension, as well as the combination, to contribute to variation in the function. The combined *ANOVA* kernel is defined as,

$$k_2(\mathbf{x}, \mathbf{x}') = \sigma_f^2 \left(1 + \sigma_{f,r}^2 k_{\mathrm{mat}}(\rho, \rho')\right) \left(1 + \sigma_{f,a}^2 k_{\mathrm{W}}(\theta, \theta')\right) \tag{4.18}$$

where $\sigma_{f,m}$ and $\sigma_{f,a}$ act as weights representing the influence of changes in each dimension on a change in the output.

4.2.3 Hyperparameter learning

Thus far, the kernels of the GPs have been presented as priors over the functions which that GP will generate. However, each of these kernels has a small number of associated *hyperparameters*, which govern the characteristics of the family of functions they represent. It is necessary, therefore, to review how a user may practically ascertain the values of these hyperparameters. As with many problems in machine learning, and indeed engineering, this boils down to an optimisation problem. The specific form of this problem will now be shown.

The hyperparameters vary depending on the form of the kernel, but for generality, $\mathbf{\Theta}_k$ is considered to be the vector of hyperparameters for whichever kernel is being used. For example, in the case of the kernel proposed by equation (4.18), this vector is defined as $\mathbf{\Theta}_k = \{\ell, \sigma_{f,r}^2, \sigma_{f,a}^2, \tau, \sigma_n^2\}$. The hyperparameters each control distinct and important characteristics of the kernel. For example, for the kernel mentioned above, the characteristics are interpreted as follows:

(i) ℓ is the characteristic length scale of the Matérn kernel.

(ii) τ is the characteristic steepness of change with respect to angle (Figure 4.1(b)).

(iii) σ_f^2 terms are scaling factors for individual kernels which control their relative importance when combined.

(iv) σ_n^2 is the noise variance parameter related to the expected measurement noise in the signal.

Standard practice to determine the hyperparameters of a Gaussian process is to maximise the *marginal likelihood*, which in practice is done by minimising the *log marginal likelihood* (NLML),

$$\hat{\mathbf{\Theta}} = \arg\min(-\log p(\mathbf{y}|\mathbf{\Theta})) \tag{4.19}$$

where the negative log marginal likelihood of the Gaussian process is given by,

$$-\log p(\mathbf{y}|\mathbf{X}, \mathbf{\Theta}) = \frac{1}{2}\log|K_y| + \frac{1}{2}\mathbf{y}^\top K_y^{-1}\mathbf{y} + \frac{N}{2}\log(\sigma_n^2) \tag{4.20}$$

When defining $K_y = K(X, X) + \sigma_n^2\mathbb{I}$, $K(X, X)$ is the pairwise covariance matrix of all of the training inputs and N is the number of data points.

4.2.4 Performance metrics

At this point it is necessary to discuss some metrics by which machine-learning models can be assessed. It is common practice to separate the data into a *training* set, $\mathbf{X}_{tr}$ and a *test* set $\mathbf{X}_t$. The performance of each model is then reported on both the training and the test data; it is important to consider the test data performance, as this is the best indicator of which models are able to *generalise*, i.e. which will work best on unseen data.

The first metric used here is the *normalised mean squared error* (NMSE) which can be computed for both training set (NMSE_{tr}) and test set (NMSE_t). For descriptive purposes, the NMSE indicates how well the estimate of the output fits with the observed values. The NMSE will return a score of zero when the predicted values are identical to those measured (this is impossible in the presence of any noise). A score of 100 is equivalent to simply taking the mean of the observed data as the prediction at every instance. The calculation for the NMSE is,

$$\text{NMSE} = \frac{100}{n\sigma_y^2}(\mathbf{y} - \mathbf{y}^*)^\top(\mathbf{y} - \mathbf{y}^*) \tag{4.21}$$

where $\mathbf{y}$ is the vector of observed outputs and $\mathbf{y}^*$ the predicted outputs. n is the number of observations in $\mathbf{y}$ and σ_y^2 the variance of those observations.

The second metric will be to compare the predictive likelihoods of the model. This metric can be a more informative way of assessing the models as it takes into account the uncertainty in the prediction, as well as the quality of the mean fit. The predictive likelihood is given as $p(\mathbf{y}^*|\mathbf{x}^*, \mathbf{y}, \mathbf{x})$; this will change, dependent upon the model being assessed. For models which have a tractable Gaussian posterior, such as Bayesian linear regression and Gaussian process models, it is given by,

$$p(\mathbf{y}^*|\mathbf{x}^*, \mathbf{y}, \mathbf{x}) = \mathcal{N}(\mathbb{E}[\mathbf{y}^*], \mathbb{V}[\mathbf{y}^*]) \tag{4.22}$$

This quantity is used here in two ways. First, one can consider each prediction to be independent, by not including the cross variance terms in $\mathbb{V}[\mathbf{y}^*]$, the predictive variance matrix. The full covariance of the prediction, which considers each prediction to be co-dependent, can also be considered from the Gaussian process, and this can give better insight into how well the function has been modelled.

For computational stability, these likelihood estimates are both calculated in the log space. The first quantity will be referred to as the *independent predictive log-likelihood* PLL_i, and is defined by,

$$\text{PLL}_i = \sum_i^N \log \mathcal{N}(\mathbf{y}_,|\mathbb{E}[\mathbf{y}_i], \mathbb{V}[\mathbf{y}_i, \boldsymbol{\Theta}]) \tag{4.23}$$

for N data points. This is the product over the predictive likelihoods for every point, i.e. the joint likelihood if they were uncorrelated. The second will be considered the *co-dependent predictive log-likelihood* PLL_c, defined by,

$$\text{PLL}_c = \log p(\mathbf{y}_,|\mathbb{E}[\mathbf{y}_i], \mathbb{V}[\mathbf{y}_i, \boldsymbol{\Theta}]) \tag{4.24}$$

where PLL_c is computed as the likelihood of the full multivariate Gaussian over the predictive points, including the predicted covariance between these points. The full cross-covariance is not returned from the BLR method and so PLL_c cannot be calculated.

5

MODELLING GUIDED WAVE FEATURE SPACES IN COMPLEX MATERIALS

A key step in any structural health monitoring strategy is to establish a *baseline* or *healthy* state, deviation from which indicates damage. For guided-wave signal data, a healthy state can be found by measuring the propagation of signals in an undamaged system, either through experimental, analytical or numerical modelling. In order to reduce computational complexity and data storage, novelty detection using signal data is often done on a D-dimensional *feature space*. Transformation into the D-dimensional space from the full signal can be by either a dimensionality reduction technique or by physics-based signal processing. In this chapter, feature spaces from physics-based signal processing are used. Determination of a baseline model can be either physics driven, data driven, or a combination of both.

As discussed earlier, there have been many advances for guided waves in complex materials (see Chapter 2). A particular issue in modelling guided waves in fibre-composites is the phenomena of continuous mode conversion (CMC) [75, 76], which causes propagation-angle-dependent wave behaviour, such as wave velocity variation and attenuation. As a result of the increased cost and requirements of modelling guided waves in fibre-composites, there has been an increase in the use of purely data-driven models to determine a baseline state [129]; however, it is then reasonable to assume this baseline state *only* applies to nominally-identical scenarios/structures from which the data are collected. Since models generated from typical data-driven methods are general and not specific to the scenario of interest, enhancing the data-driven models may be valuable in order to offer advantages, such as extrapolability, whilst maintaining accuracy from real data.

In this chapter, a novel approach to feature-space modelling of guided waves in fibre-composite materials is presented, which uses physical knowledge to build structured machine-learning tools. Instead of building directly interpretable models (such as a system identification approach to find material properties), belief is embedded from prior knowledge of the physics which controls guided-wave features. Firstly, purely physical one-dimensional models of the attenuation of the waves as they propagate from a point source are investigated. The one-dimensional models are based on a Bayesian linear regression (BLR). This choice allows insight into the effect and contribution of the first two attenuation mechanisms described by Pollock [74], *geometric spreading* and *material damping*. This is followed by two-dimensional feature space modelling using Gaussian processes. Increasingly sophisticated models are generated to incorporate physical knowledge into the machine learning tool. After considering the effectiveness of a 'black-box' approach, where the model is purely based on data, the knowledge of the guided waves is included via two techniques; one of which is through incorporation of a mean function in the radial direction from the source. The mean function models the one-dimensional attenuation, i.e. it models the geometric spreading and material damping in the composite. The second approach is to include the physical knowledge of the guided waves by modifications to the kernel of the Gaussian process.

The models were tested on an energy-based feature extracted from signals of surface displacement measurements on a carbon-fibre-reinforced-polymer (CFRP) plate, taken using a scanning-laser-doppler-vibrometer (SLDV). CFRP weave represents one of the most complex materials to model guided wave propagation; for example, it strongly results in CMC, and has lines of symmetry for angular-dependent propagation. The use of CFRP is becoming more popular in aerospace and automotive applications [130, 131] and have potential future use in wind turbine blades [132]. For these reasons, CFRP was the chosen material for this work, as enhancing the understanding of guided waves for damage detection in fibre-weave materials is crucial.

5.1 Experiment

The physical setup of the experiment is shown in Figure 5.1, highlighting the orientation of the plate, where the fibre directions are shown by the coordinates arrows on the front view diagram. Wave propagation directions of 0°, 90°, -90° and 180° are termed as propagation *along* the fibres, and other directions as *through* the fibres. Guided waves were initiated in a CFRP plate by excitation of a 20mm diameter piezo-electric transducer (PZT) at the centre of the plate, as shown in Figure 5.1. The PZT was actuated with a 300kHz, five-cycle, Hanning-windowed sine wave, allowing multiple wave modes to be excited. A Polytec PSV-400 scanning laser vibrometer was used to measure the out-of-plane surface displacement of the induced wave-packets on the opposite side to the PZT, where the recording state was synchronised with the start of the excitation signal. Each wave-packet was then fed through a simple feature-extraction process to generate a two-dimensional feature-space map of the maximum of the Hilbert envelope, h_m, over the surface of the plate. The Hilbert envelope is taken as the magnitude of the complex Hilbert transform of the full signal. The maximum value of this envelope represents the maximum amplitude of the energy of the wave packet. Specific details of the experimental setup are shown in Table 5.1.

The results of the experiment showing the raw data feature-space map of h_m over the surface of the plate can be seen in Figure 5.2. One can clearly see the effect of the fibres on the amplitude of the first asymmetric mode; thanks to the phenomena of continuous mode conversion, the amplitude is greater when propagating along the fibres compared to when propagating across the fibres. There appears to be a ‘band’ of higher-energy waves at a propagation angle of 20°, which may be due to imperfections in the layup of the material, however, destructive testing and inspection

Plate dimensions	300 mm × 300 mm × 1 mm
Layup	$[90/0/90]_s$, Epoxy matrix
PZT Location	150 mm × 150 mm
Central frequency	300kHz
Signal record length	4ms
Pre-trigger	400µs
No. scan points	8,314
No. of averages	200

Table 5.1: Details of experimental setup used to acquire feature-space data.

of the plate revealed no major inhomogeneities. After inspection of the experimental area, the authors believe this to be an artefact resulting from strong reflections of light by a nearby object, which interfered with the laser measurement. This experimental procedure, though simple, is pivotal for the advanced tools in order to aid 'black-box' data-based ML tools for development of an *informed, data-driven* (IDD) model.

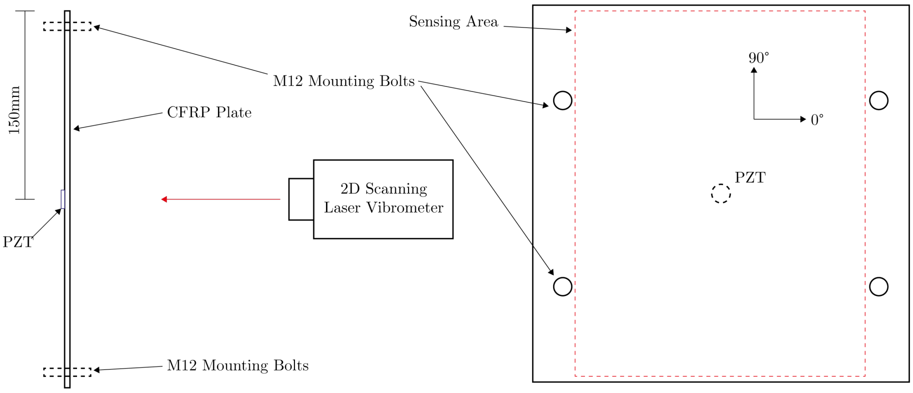

Figure 5.1: Diagram showing the experimental setup and location of PZT on the 300 mm × 300 mm CFRP plate. The left diagram shows as top-down view of the setup, and the right a front-on view. The redd dashed line shows the area captured using the SLDV, which was done up to the location of the bolts which held the plate in place.

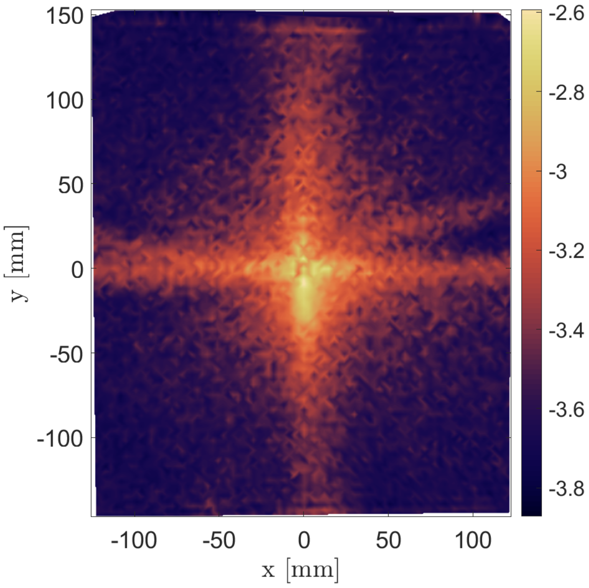

Figure 5.2: Results of feature-space map of h_m over the surface of the plate from raw data, represented in $\log_{10}$ scale for viewing purposes.

5.2 One-dimensional attenuation model

Initially, a one-dimensional attenuation model is considered, modelled using a Bayesian linear regression (BLR). A full description of BLR is given in Section 4.1. Several basis expansions of propagation distance ρ were tested in combination, the full model is shown in equation (5.1). These basis expansions correspond to different attenuation mechanisms associated with damping, geometric spreading and a combination of the two; these models are shown in Table 5.2. The parameters $(\Phi = \phi_1, \phi_2, \phi_3)$ are switching parameters $(\phi_n = 0, 1)$, which control the combination of functions shown in equation (5.2b). The initial model of the any energy based feature A, as a function of the propagation distance ρ, is defined as,

$$A(\rho) = \beta_1^{\phi_1}(\exp(-\beta_2\rho))^{\phi_2}\left(\rho^{-1/2}\right)^{\phi_3} \tag{5.1}$$

The model shown above is not a linear form that can be represented by equation (4.2); however, by taking the natural log of equation (5.1) a *linear-in-the-parameters* model can be developed;, this is shown below in equation (5.2b),

$$f(\rho) = \ln(A(\rho)) = (\ln(\beta_1)) \cdot \phi_1 - (\beta_2\rho) \cdot \phi_2 - 1/2(\ln(\rho)) \cdot \phi_3 \tag{5.2a}$$

$$f(\rho) = \ln(A(\rho)) = w_1 \cdot \phi_1 - (w_2\rho) \cdot \phi_2 - 1/2(\ln(\rho)) \cdot \phi_3 \tag{5.2b}$$

The values of β_1 and β_2 can be recovered by exponentiating w_1 and w_2 respectively.

Model Basis	Linear Form	Basis Parameters
$A_1(\rho) = \beta_1 \exp(-\beta_2\rho)$	$f(\rho) = \ln(\beta_1) - \beta_2\rho$	$\Phi_1 = [1,\ 1,\ 0]$
$A_2(\rho) = \beta_1\rho^{-1/2}$	$f(\rho) = \ln(\beta_1) - 1/2\ln(\rho)$	$\Phi_2 = [1,\ 0,\ 1]$
$A_3(\rho) = \beta_1 \exp(-\beta_2\rho)\rho^{-1/2}$	$f(\rho) = \ln(\beta_1) - \beta_2\rho - 1/2\ln(\rho)$	$\Phi_3 = [1,\ 1,\ 1]$

Table 5.2: Bayesian linear regression model basis expansions

The models shown in Table 5.2 were tested for two different cases; the first is where data are collected at points along the fibres in the weave and the second when across the fibres. The NMSE is calculated using equation (4.21) for both the training set and test data sets (NMSE_{tr} and NMSE_t respectively), and are shown in table 5.3. From the values of the NMSE for both propagation orientations, it appears that the multiplicative combination of geometric spreading and material damping is the most promising model for the attenuation of the energy of the first antisymmetric mode for all propagation directions in a CFRP plate.

When modelling the attenuation of the guided waves propagating through the fibres, the 95% confidence intervals, seen in Figure 5.3, are much larger. This is also reflected in the values for σ^2 in Table 5.3. By inspection of Figure 5.3, it appears that although the multiplicative combination of both attenuation mechanisms provides the optimal model, for propagation directions across the fibres, further mechanisms need to be included. As the wave propagates across the fibres, *continuous mode conversion* [75, 76] will provide additional mechanisms of attenuation. In contrast, when propagating along the fibres, the wave mode is relatively uninterrupted in comparison, and so its initial energy has a strong effect on the resulting shape.

An advantage of the method shown here is that the parameters are directly interpretable; here β_1 represents the product of the relative initial energy of the wave

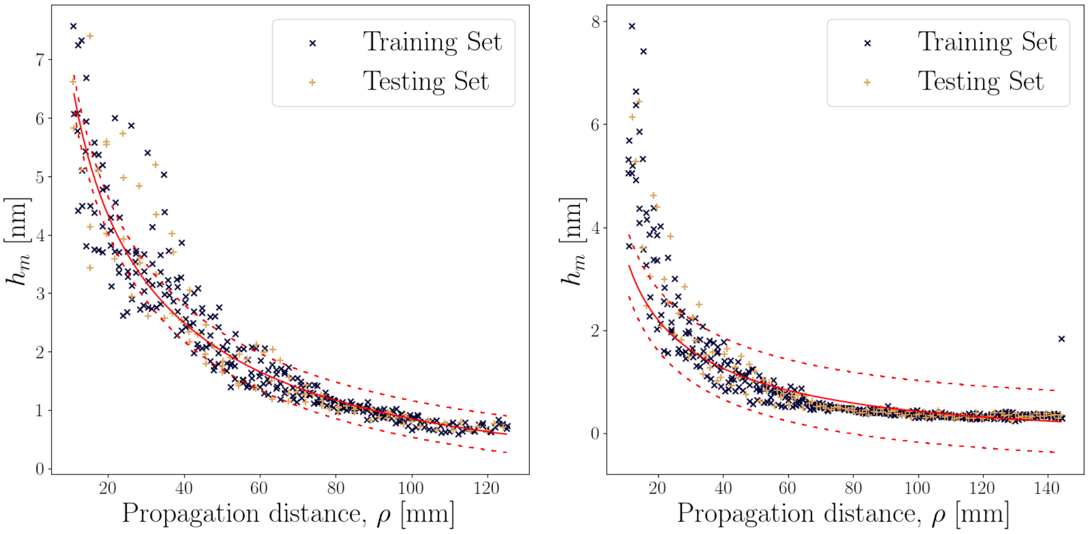

(a) (b)

Figure 5.3: Models of attenuation of the energy of the first antisymmetric mode using model Φ_3 for propagation directions (a) along the fibres and (b) across the fibres. The estimated mean function is plotted with a solid red line and the 95% confidence interval is shown with dashed red lines.

(A_0 in equations (3.26) and (3.27)) and some constant α, and β_2 represents the viscoelastic attenuation coefficient (ζ_i in equation (3.27)). For both propagation directions, there is a similar pattern in the estimated parameters:

- When only damping is included, there is a lower $A_0\alpha$ product and a larger attenuation coefficient
- When only geometric spreading is included, there is a higher $A_0\alpha$ product estimated than for model $\mathbf{\Phi}_1$
- When both mechanisms are included, there is a higher $A_0\alpha$ product estimated than for models $\mathbf{\Phi}_1$ and $\mathbf{\Phi}_2$, and a lower estimated attenuation coefficient than for model $\mathbf{\Phi}_1$

For both propagation directions, the values of β_1 are similar for both models which include damping; however, the initial estimated energy is lower for propagation across the fibres. As the viscoelastic damping will mostly result from material properties of the epoxy matrix, the ζ_i should remain similar for all propagation directions. However, the $A_0\alpha$ product increases when both attenuation mechanisms are included; this could be because of the need for both mechanisms to be included in order for the model of decay to encapsulate all data points from an initial starting energy.

	β_1	β_2	σ^2	$\sigma_{\mathbf{w}}$	NMSE$_{tr}$	NMSE$_t$	PLL_i
				Along fibres			
Φ_1	5.917	0.01983	0.1731	1.360e-04	4.724e+04	1.465e+04	1.595e+05
Φ_2	12.441		0.3577	3.188e-01	3.495e+04	1.136e+04	1.100e+05
Φ_3	23.834	0.01034	0.1565	1.109e-04	5.413e+04	1.669e+04	1.263e+05
				Through fibres			
Φ_1	2.807	0.01866	0.3784	4.851e-04	4.611e+04	1.530e+04	8.259e+04
Φ_2	5.340		0.5098	6.481e-01	4.107e+04	1.356e+04	4.759e+04
Φ_3	12.110	0.0106	0.2996	3.041e-04	4.970e+04	1.626e+04	1.411e+05

Table 5.3: Table of results from 1D attenuation modelling using BLR; β_1 & β_2 are linear-form model weight parameters, σ^2 is the estimated variance of the function, $\sigma_{\mathbf{w}}$ is the estimated variance of the weights, NMSE$_{tr}$ is the *normalised mean squared-error* between the model and the dataset used for training, NMSE$_t$ is between the model and the independent validation set, and PLL_i is the independent log-likelihood.

As can be seen in Table 5.3, the confidence in the mean weights (which increases as $\sigma_{\mathbf{w}}$ decreases), is similarly large for model Φ_1 but shows much less confidence for model Φ_2. The confidence in the mean weights is increased again for model Φ_3, indicating that for this model, one is most certain about the parameters. However, the confidence in the weights is decreased when modelling attenuation of propagation across the fibres.

5.3 Two-dimensional feature-space model

So far, it has been shown how physical attenuation phenomena can be modelled via a Bayesian linear regression along one dimension (the propagation direction). Now, attention turns to modelling the two-dimensional input feature space. If such a plate were homogeneous, modelling of the features along any one direction would provide an adequate model of the two-dimensional feature space. However, in more complex materials – such as composites – this is no longer sufficient. Instead, the attenuation changes with direction, and therefore the model of the space must be able to capture changes in behaviour across the two-dimensional field. For waves propagating from a point source, it can be helpful to think that there is a radial and angular component to the *function* over the space which describes the feature of interest.

To build such a model, it is necessary to have a tool which can model data across a two-dimensional space on the basis of observed data and which can be guided by belief about the physical phenomena. For this purpose, a machine-learning approach is adopted; the tool chosen for the job is a *Gaussian process* (GP). The kernel used in the GP is a significant modelling choice, and modifications of these provide structure via embedding prior belief in the model. Prior belief can also be introduced by inclusion of a mean function $m(\mathbf{x})$, although this can be considered a more constrictive approach to imposing prior beliefs, as only residual information is then determined by the GP.

An important characteristic of GPs is that standard stationary kernels operate based on the Euclidean distance between two points, and so map covariances well when using Cartesian space input. However, the physics and behaviour of guided waves is described here using the polar coordinate system, as they are emitted from a point source. Therefore, this attribute must be considered when utilising GPs for modelling the feature-space of guided waves. A method of applying Gaussian processes on a polar input space has been outlined in Section 4.2.2, where separate kernels are applied to the angular and radial dimensions separately, before combining to generate an overall covariance function.

5.3.1 Kernel choice and design

The kernel used in the GP is a significant modelling choice, and modifications of these provides structure by embedding prior belief in the model. In this work, several approaches to modelling the h_m feature space over the surface of the plate are applied. Firstly, two general nonlinear kernels are applied; the SE kernel (equation (4.13)) is applied to the Cartesian input space and the generic polar kernel (equation (4.18)) is applied to the polar input space. Secondly, a non-zero mean function is included with the generic polar kernel and then the kernel as modified to assume the prior belief embedded via the mean function is accurate. Finally, novel kernels are introduced which embed physical knowledge via kernel design.

General nonlinear kernels

The simplest and perhaps most obvious choice for mapping the features across a composite plate would be to set $\mathbf{x} = \{x, y\}$, the Cartesian coordinates of a location on the plate. This method imposes the prior belief that the feature being modelled across the plate will vary smoothly in a nonlinear manner with respect to the x and y coordinate. In many senses this is the simplest model that could be chosen, it is also the most flexible, as it imposes very little restriction on the form of the functions that can be modelled.

However, since it is known here that the waves are generated from a point source in the centre of the plate, and that these will propagate from that point, the behaviour would be better modelled in a set of polar coordinates. For the general case, here the work of Padonou and Roustant [127] is followed, and a detailed description is provided in Section 4.2.2. The general polar kernel is defined as,

$$k_2(\mathbf{x}, \mathbf{x}') = \sigma_f^2 \left(1 + \sigma_{f,r}^2 k_{\text{mat}}(\rho, \rho')\right) \left(1 + \sigma_{f,a}^2 k_{\text{W}}(\theta, \theta')\right) \tag{5.3}$$

where $\sigma_{f,m}$ and $\sigma_{f,a}$ act as weights representing the influence of changes in each dimension on a change in the output.

Since the GP is a generative model over functions, it is possible to sample realisations of possible functions from the distribution, allowing the user to understand the type of functions that the kernel will generate. If this is done without conditioning the model on any data points, it is possible to see what realisations from the *prior* may look like. This strategy can be helpful, as it allows the user to understand heuristically the type of functions that the kernel they have chosen will generate. In this case, it will be used to show how the models can generate behaviour which appears closer to what would be expected physically *a priori*. Using this method, four

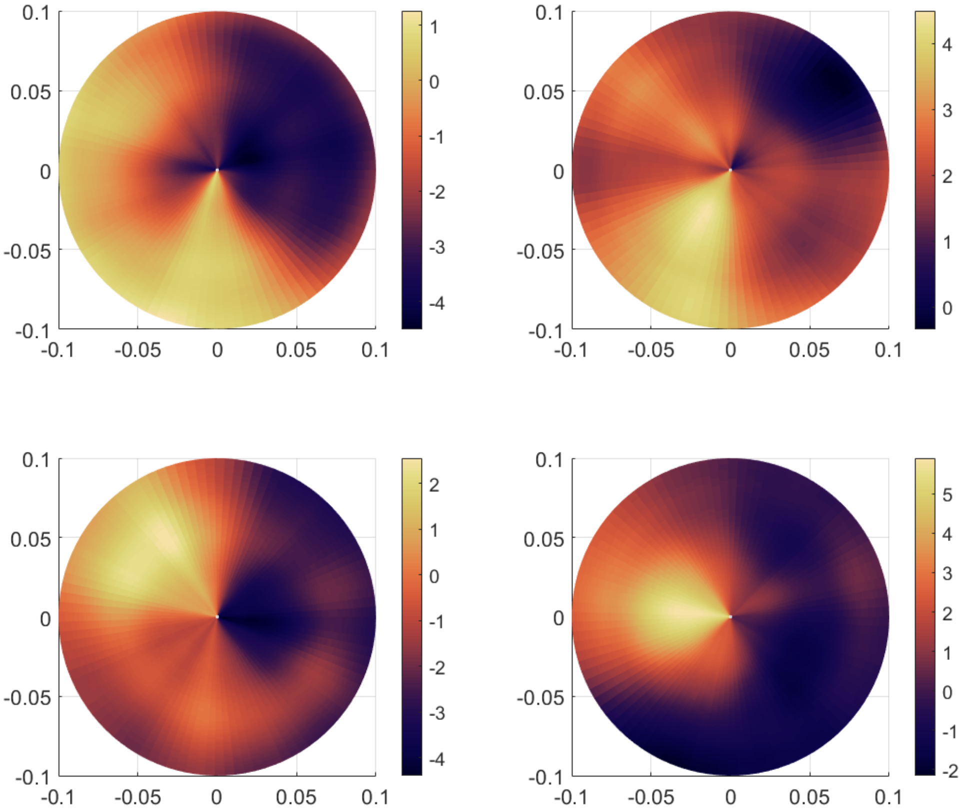

Figure 5.4: Selection of four random polar space functions randomly generated from covariance function represented in equation (5.3), with hyperparameter values of $\tau = 4$, $l = 1$ and $\sigma^2_{f,m} = \sigma^2_{f,a} = 1$.

prior realisations were generated from the polar kernel shown in equation (5.3), and can be seen in Figure 5.4. The functions generated appear to operate separately on each dimension ρ and θ. A key characteristic to note, is that there is no discontinuity as θ moves through 2π to zero in the angular direction; this is as a result of choosing the Wendland-C^2 function kernel (equations (4.15) and (4.16)). Further discussions on the characteristics of such a kernel can be found in [127]. For this work, the polar kernel will serve as an alternate model where there is very little restriction placed on the functions that can be modelled. It can also be considered to embed minimal knowledge of the physics of the process except that the function can be well represented in a polar coordinate space. The knowledge this kernel embeds is periodicity on θ, which for systems described by polar coordinates is inherent in their physics.

Mean function modelling of attenuation

From this point onwards, the model learning will make use of prior knowledge of guided-wave propagation. This informed model learning will begin by considering how a mean function $m(\mathbf{x})$ can be used to introduce a physical basis to the model. There is no restriction on this mean function, given that it is known. Mathematically, it is trivial to include the mean function (if known), by simply subtracting the expected mean function from the target data and training on the residuals,

$$\tilde{\mathbf{y}} = \mathbf{y} - m(\mathbf{x}) \tag{5.4}$$

This can be interpreted as learning the difference or discrepancy between this chosen mean function and the generating function of the data. In this scenario, the mean function $m(\mathbf{x}) = \mathbf{w}^{\top}\phi(\mathbf{x})$ is the model described in Section 5.2, the one-dimensional Bayesian linear regression model. Since the weights of the model vary depending on the propagation direction with respect to fibre orientation, it is necessary to simultaneously learn the distribution of $\mathbf{w}$ – the weights of the BLR – and the hyperparameters of the GP. Therefore, the linearised form shown in equation (5.2b) is used, and the target data become,

$$\tilde{\mathbf{y}} = \ln(\mathbf{y}) - \ln(\rho^{-1/2}) - m(\mathbf{x}) \tag{5.5}$$

and the step for training and finding expected values of the mean and variance can be followed as in [125]. This solution can be interpreted as finding the mean one-dimensional behaviour across all propagation directions. This mean behaviour is then compensated by the GP to fit the observed data and learn the latent function which describes it.

Functional priors via kernel design

An alternative to using the mean function to include what is known about guided waves, is to modify the kernel. It is possible to restrict the *family of functions a* *priori* to generate only functions which are plausible, given physical understanding of the guided waves. This restriction is the key advantage of the proposed Bayesian approaches presented here.

All of the models which are generated from this point onwards will consider the propagation of the guided waves to occur in a polar coordinate system, where the source is located at radius $\rho = 0$, i.e. the source is at the origin. These kernels will build upon the work of [127], by also incorporating prior belief about the physical form of the guided-wave feature space. Since the kernel which defines the process will be composed of the ANOVA combination of the radial component and the angular component, it is possible to consider how to modify each of these components individually. In other words, it will be shown how expected radial and angular behaviour can be embedded in isolation from the other. This separation of dimensions in modelling is especially useful, since varying amounts of information may be available for each of these.

Imposing rotational symmetry in the feature space It can be seen in Figure 5.2, that the energy of the wave exhibits a symmetry on the plate. Physically, this makes sense, given what is known about the symmetry in the orientation of the fibres in the lay-up; it is therefore desirable to exploit this in the kernel. equation (5.6) was designed to model this symmetric behaviour. The strictly-periodic kernel is applied to the angular dimension, where n can be altered to include the number of axes of symmetry,

$$k_{\text{sym}}(\theta, \theta') = \left(\alpha_1 + \alpha_2 \cos(2nd_2)\right), \qquad n \geq 1 \tag{5.6}$$

$d_2 = \arccos(\cos(\theta - \theta'))$ is the geodesic distance, n the number of symmetry axes required, α_1 is the offset term, and α_2 the amplitude hyperparameter.

Sample functions from this prior are shown in Figure 5.5. These samples show the strict periodicity that this kernel imposes. Notably, this form of kernel does not enforce the phase of the function. Instead, as data are observed, the posterior distribution — or function that is learnt — adapts to the phase information in the

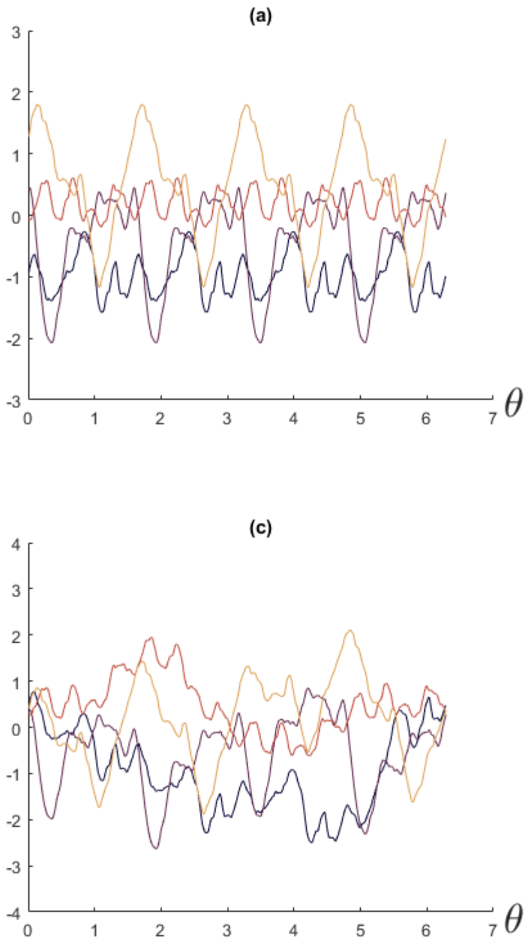

Figure 5.5: Samples of random prior functions for the angular kernel designs, over a full circle range, for (a) strictly-periodic kernel (equation (5.6)), (b) squared-exponential kernel (equation (4.13)), (c) multiplied combination and (d) additive combination of the kernels (equation (5.7)). Each line represents a different random function drawn from these priors.

data. This adaptability is a benefit, since enforcing phase within the kernel may lead to issues if the fibre orientation is not known exactly.

The primary issue with the strictly-periodic kernel is the assumption of consistent rate of variation in the function with θ, which may make equation (5.6) too restrictive to model accurately the guided-wave feature space. It is clear to see in Figure 5.2, that the energy of the wave decays rapidly in the transition between propagation along fibres and across fibres, as the angle θ varies. Therefore, flexibility was introduced by an additive combination of the strictly-periodic kernel and the squared-exponential kernel previously shown in equation (4.13).

As well as allowing a varying rate of change with θ, a combined kernel also reduces some of the restrictions that are imposed with the pure strictly-periodic kernel of equation (5.6). An additive combination was used as opposed to multiplicative, as this does not generate large variations in amplitude between period peaks and allows for the kernel to capture the symmetry, while still allowing some variation to take place. The additive combination can be considered an 'OR' operation [133], the resulting kernel applied to the angular dimension is given by,

$$k_{\text{ang}}(\theta, \theta') = \sigma^2_{f,\text{sqe}} \exp\left(-\frac{d_2^2}{l_1^2}\right) + \sigma^2_{f,\text{sym}} \left(\alpha_1 + \alpha_2 \cos\left(n d_2\right)\right) \tag{5.7}$$

An important property of the resulting kernel is that it is *stationary*, as it is only proportional to the distance between points, rather than their values. This fact means that the kernel is unaffected by translation or rotation of the coordinates, a key advantage when modelling in the angular dimension.

Kernel forms for radial attenuation As discussed in Section 3.4, two known and documented attenuation mechanisms can be modelled; these are shown in equations (3.26) and (3.27). Attenuation effects resulting from viscoelastic damping of a material can be embedded into the priors by the use of an *exponential decay* (ED) kernel, where propagation distance represented by the vector ρ,

$$k_{\text{ed}}(\rho, \rho') = \exp\left(-\rho\ell\right) \cdot \exp\left(-\rho'^{\top}\ell\right) \tag{5.8}$$

Attenuation effects from geometric spreading can be modelled by the use of a polynomial kernel (equation (5.9)), where $p = -1/2$, in order to represent equation (3.26).

$$k_{\text{pol}}(\rho, \rho') = (\rho \cdot \rho'^{\top})^p \tag{5.9}$$

Prior draws from both the ED and polynomial kernels can be seen in Figures 5.6(a) and 5.6(b) respectively. Both kernel functions embed decay with respect to

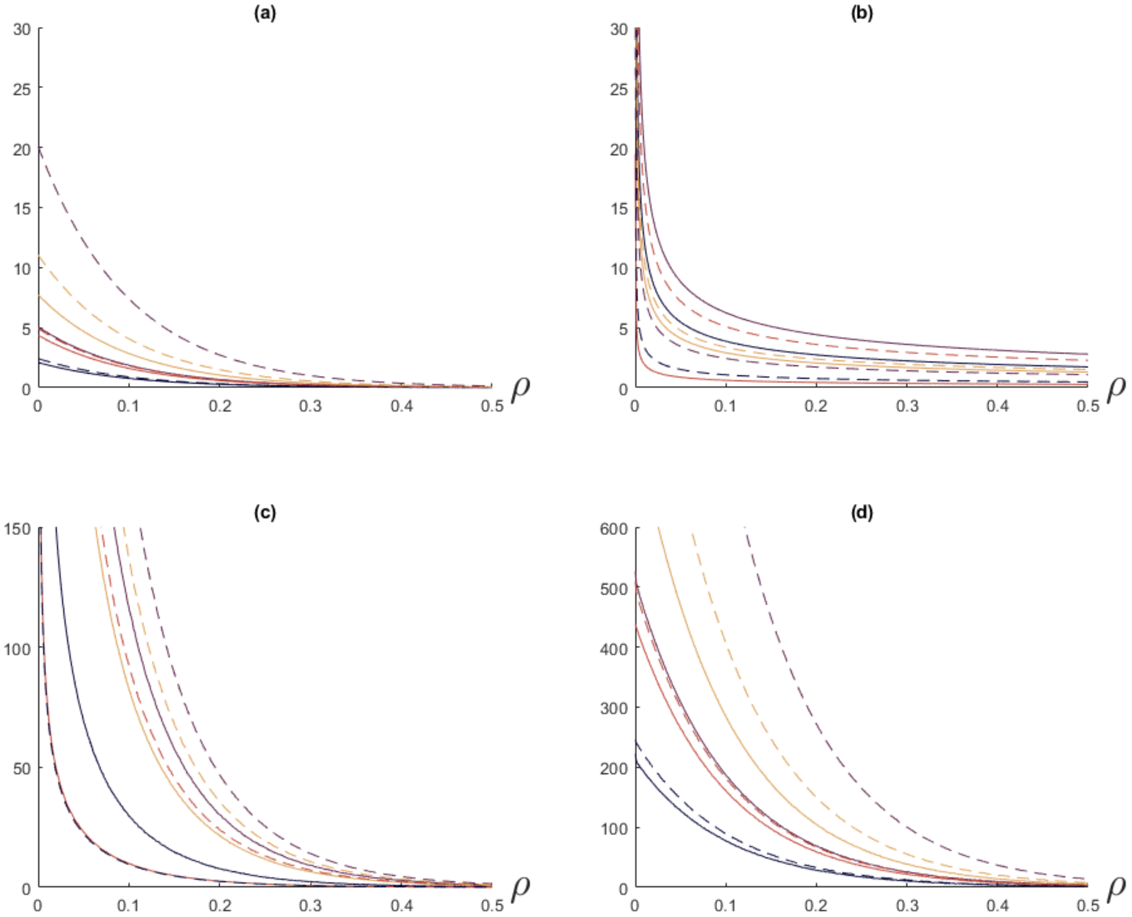

Figure 5.6: Samples of random prior functions for the radial-kernel designs, for (a) exponential decay kernel (equation (5.8)), (b) square-root decay (equation (5.9)), (c) multiplicative combination (equation (5.10)) and (d) additive combination of the kernels. Each line represents a different random function drawn from these priors.

propagation distance ρ, but each model shows a different mechanism for this decay. The kernel chosen to represent decay from geometric spreading will always tend to infinity as $\rho \to 0$ and this limitation should be considered.

To illustrate the use of these kernels, multiplicative and additive combination of these two attenuation mechanism kernels can be seen in Figures 5.6(c) and 5.6(d) respectively. A multiplicative combination of the attenuation mechanisms aligns more closely with physical understanding and the discussion presented in [120], since the kernels operate to reduce the energy in the wave simultaneously and do not subtract energy, but rather reduce it multiplicatively. As such, a kernel to model attenuation along the radial direction is proposed as the multiplicative combination of the exponential decay (equation (5.8)) and polynomial (equation (5.9)) kernels; thus,

$$k_{\text{rad}}(\rho, \rho') = \sigma^2_{f,r}(\rho \cdot \rho'^{\top})^p \ \cdot \ \left(\exp\left(-\rho\ell_2\right) \cdot \exp\left(-\rho'^{\top}\ell_2\right)\right) \tag{5.10}$$

Combined two-dimensional kernel It has been shown how understanding of the physical processes involved in the attenuation of guided waves can be used to impose prior belief in the GP machine learning model along each of the radial and angular dimensions. It remains to explain how these may be combined to form a meaningful prior over the two-dimensional feature space.

Following closely the approach of [127], for the general nonlinear kernel in polar coordinates, the two kernels described in equations (5.7) and (5.10) will be combined using an *ANOVA* approach,

$$k_3(\mathbf{x}, \mathbf{x}') = \left(1 + \sigma^2_{f,a}k_{\text{ang}}(\theta, \theta')\right)\left(1 + \sigma^2_{f,r}k_{\text{rad}}(\rho, \rho')\right) \tag{5.11}$$

where $\mathbf{x} = \{\{\theta, \rho\}_1, ..., \{\theta, \rho\}_m\}$.

Again, it is possible to draw samples of the functions, now in the two-dimensional space, to visualise the restrictions which have been placed on the functions that can be modelled. Four prior draws from a GP with zero mean and the covariance defined in equation (5.11) can be seen in Figure 5.7. It should be noted at this point, that the input units and output values are non-dimensional, and the figures showcase key characteristics imposed by the kernels, by displaying functions that are samples from an arbitrary prior. It is reassuring that these prior draws match, at least visually, the behaviour that would be expected in the data being modelled. This type of *prior predictive checking* can be invaluable for confirming that the assumptions built into the model are reasonable. A key feature that can be seen is the symmetry that is introduced in the angular dimension without requiring a fixed phase to be specified. It can also be seen that slight variations from this symmetry are possible via the inclusion of the squared-exponential kernel in equation (5.7). The decay in the radial direction as a result of the kernel shown in equation (5.10), is also clearly seen. As a result of these characteristics, it has been shown how a GP kernel can be designed in such a way that it is applicable to modelling the attenuation of guided waves in a two-dimensional space.

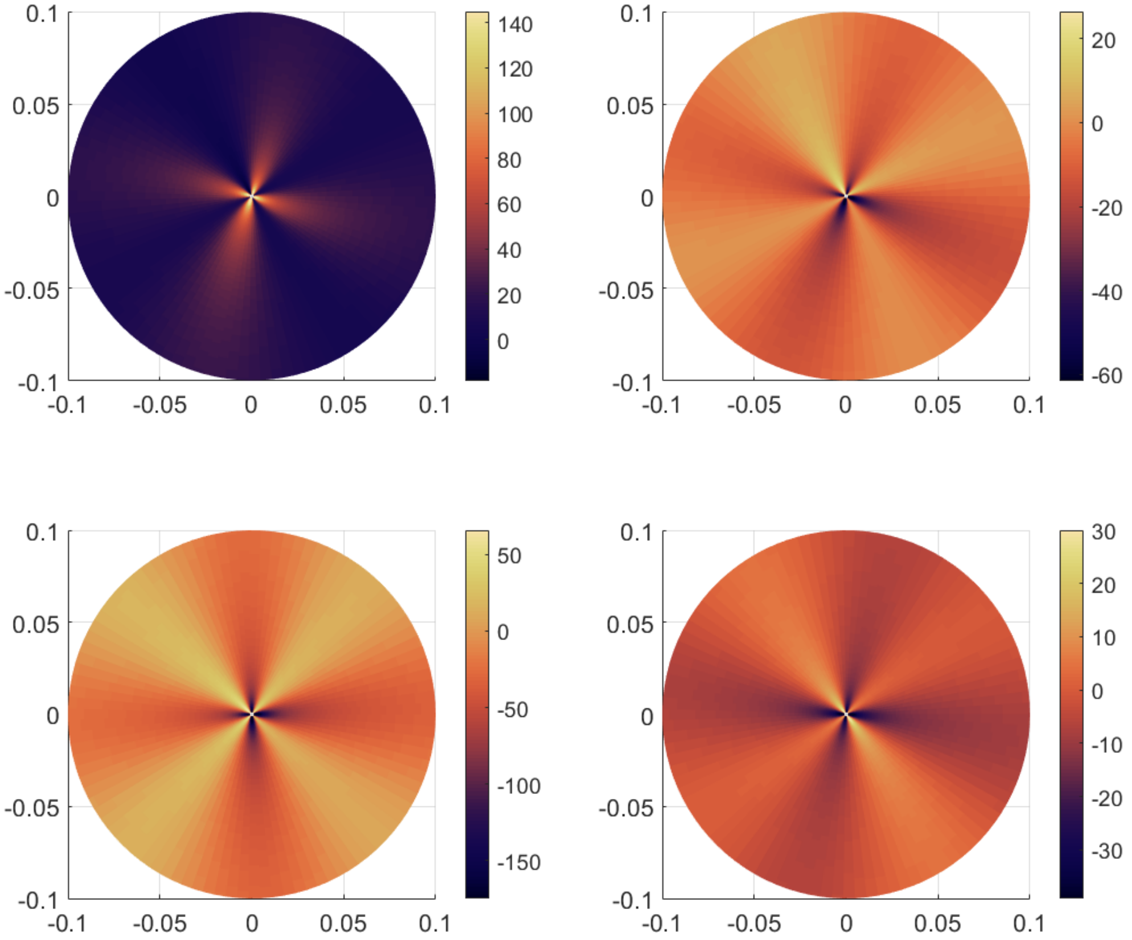

Figure 5.7: Four samples of random polar space functions, selected from 1000 random functions generated from the covariance function represented in equation (5.11), with hyperparameter values of $\boldsymbol{\Theta}_k = \{1, 10, 10, 1, 1, 1, 1, 1, 0.001\}$. Here the functions are non-dimensional as the functions are samples from an arbitrary prior.

A second kernel was also tested with the same radial component as described in equation (5.10), but with an alternative angular kernel. For this method, $k_{\text{ang}}(\theta, \theta')$ becomes a modified version of equation (4.16), where the geodesic distance is instead

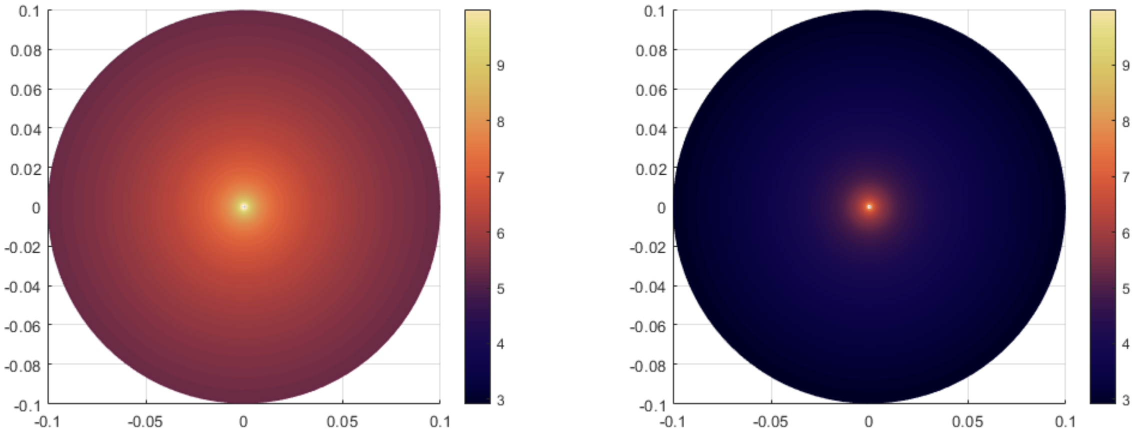

Figure 5.8: Prior variances over polar coordinate space from kernel E (left) and kernel F (right), represented by equations (5.11) and (5.12) respectively. Variances are plotted in $\log_{10}$-scale for viewing purposes.

defined as $d_2(\theta, \theta') = \arccos(\cos(2n(\theta - \theta')))$, where n is again the number of symmetry lines required. This alteration was made to still enforce symmetry, but allow a more flexible modelling of the functions being considered in the angular dimension. This kernel has the form,

$$k_4(\mathbf{x}, \mathbf{x}') = \left(1 + \sigma_{f,a}^2 k_{\mathrm{W}}(\theta, \theta')\right) \left(1 + \sigma_{f,r}^2 k_{\mathrm{rad}}(\rho, \rho')\right) \tag{5.12}$$

So far, only samples from each GP have been shown. However, it is possible to recover the distribution over the model in closed form. Since the mean function chosen in most models is simply zero across the complete space, the prior mean is not very informative. The prior variance, however, is of interest to consider. In Figure 5.8 the prior variances of equations (5.11) and (5.12) are shown. It is important to remember that this is the variance in predictions made by the model before the information from any data has been included. The variance for both of these kernels is seen to decay as the distance from the source increases. The model will tend towards infinity at $\rho = 0$ for two reasons; the kernels are non-stationary [125], and because of the exponential decay included via equation (5.8), the function values themselves will tend towards infinity as seen in Figure 5.7. This limitation of the models should be considered, and care should be taken if predicting close to $\rho = 0$.

However, in the experimental data used in this study the waves are generated by means of a piezoelectric actuator. This means that the source of the guided waves is not a point source and the models should not be used within the region covered by the piezoelectric actuator.

5.3.2 Overview of modelling approaches

Up to this point, it has been discussed how one might construct a GP kernel which can represent the behaviour of guided-wave attenuation. It is worth reviewing the models which will be compared when results are shown on experimental data. Table 5.4 shows a summary of all six models which will be compared in this study.

As a baseline, model A is the archetypal Gaussian-process model, with a zero-mean function and the use of the squared-exponential kernel operating on two inputs, the x and y coordinates on the plate. This choice provides a benchmark, where no knowledge of the guided-waves is included.

The second model (B) is a demonstration of the use of the polar coordinate GP of [127]. This model also contains no specific reference to the physical mechanisms in guided-waves, but does make use of the knowledge that the guided-waves propagate radially from a source. The use of a polar coordinate system in this case is a sensible choice, given the structure of the data being used. This method serves as another benchmark demonstrating an approach which requires very little understanding of the physical mechanisms involved in guided-wave propagation.

Model C is the first model where a specific physical process is included. In this case, the model of wave attenuation $A_3(x)$ (Table 5.2), is used along the radial direction as the mean function. The kernel used is the same flexible polar kernel as in model B — that proposed in [127]. Importantly, this kernel remains flexible to influence the model in both the radial and the angular dimensions, potentially correcting for any unmodeled phenomena along the radial dimension in the mean function.

Model D restricts the flexibility of Model C by removing the dependence of the kernel on the radial dimension. The GP used here relies on the mean function to capture all of the radial behaviour via $A_3(x)$, and the covariance to capture all the variation in the angular dimension. This GP model form implies that the data can be generated by some function, offset from the mean, which is only dependent upon the angle being considered. This model should be considered with care, since it is highly restrictive.

Model E removes the use of the mean function; instead the knowledge of the guided waves is embedded directly in the kernel as a *functional prior*. This model enforces periodicity in the angular dimension and embeds the physical attenuation models in the radial direction by means of the kernel described in equation (5.11). Model F is very similar to Model E, but with the kernel defined as in equation (5.12), with the modification to the angular component described previously.

Model	Mean $m(\mathbf{x})$	Covariance $k(\mathbf{x}, \mathbf{x}')$	Input space
A	0	$k_{\mathrm{SQE}}(\mathbf{x}, \mathbf{x}')$	Cartesian
B	0	$k_2(\mathbf{x}, \mathbf{x}')$	Polar
C	$A_3(\rho)$	$k_2(\mathbf{x}, \mathbf{x}')$	Polar
D	$A_3(\rho)$	$k_{\mathrm{W}}(\theta, \theta')$	Polar
E	0	$k_3(\mathbf{x}, \mathbf{x}')$	Polar
F	0	$k_4(\mathbf{x}, \mathbf{x}')$	Polar

Table 5.4: Table of GP strategies tested for feature-space mapping, showing the properties and characteristics of each model.

?? provides a reference in which each of these kernel forms can be compared and in which the hyperparameters are listed. The reader may find this a useful companion if planning to reproduce the methodology from this work.

5.3.3 Results

In this section, the various approaches to modelling the two-dimensional feature space summarised in Table 5.4 will be compared. Models are compared visually and based upon a number of metrics as described in Section 4.2.4. The quantitative assessment of the models is discussed in Section 5.3.4. The first of these metrics is the log marginal likelihood LML, which is a measure of how well the model fits the training data. Next, the predictive log likelihood of an independent test set, considered in the case where every prediction is assumed independent PLL_i, and when the predictions are assumed correlated PLL_c. Finally, the normalised mean-squared error NMSE of the mean fit to the independent test set is also computed. This final metric should be treated with care, since it does not represent the quality of the uncertainty quantification in the model fit. The most rigorous test of these models can be considered to be the correlated predictive log likelihood which captures the full correlation of the predictive model, including the mean, variance and covariance predictions. For all graphical representations shown, the data are presented in a $\log_{10}$ scale, but the models were all trained directly on the values of h_m. Therefore, the units for the figures are in $\log_{10}$(mm).

Uninformed Gaussian-process models

Figure 5.9 shows the mean predictions of the two uninformed GP models (A and B in Table 5.4). It can be clearly seen, that even without specific prior knowledge, the use of polar coordinate system (Model B), offers a significant improvement over the Cartesian approach (Model A). Model A appears to be an ‘out-of-focus’ copy of the original data, whereas Model B has generated a smoother function, which is more likely to represent the physical mechanisms by which the wave operates. Even this simple consideration of the structure of the data being modelled leads to far more consistent results from the model. The quality of the fits for each of these models is compared qualitatively in Table 5.5, along with the other GP models.

Since the wave attenuation data naturally follow (approximately), a polar behaviour, one could envisage this problem as the GP trying to learn the mapping of Cartesian to polar spaces as well as the mapping from the polar to the feature-space. This two-stage mapping is being attempted with a single kernel and significantly complicates the modelling problem, thus, it is likely to underperform a model specified in the correct space. Further to this, it is concerning that the Cartesian model may have attempted to model some of the structure in the measurement noise. This is again a topic of further investigation for the future.

However, as can be seen in Figure 5.9(b), by learning the model via an uninformed kernel operating on the polar coordinates, a more believable model of the feature space is learnt. These results show that, even when implementing machine learning methods with no direct embedding of the physical process, the space in which the function operates must still be taken into account.

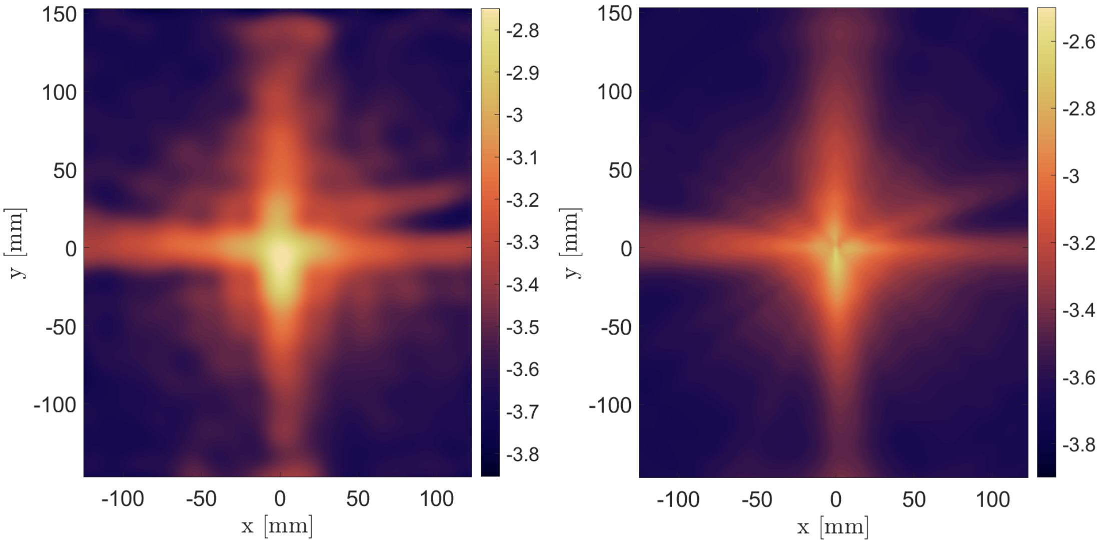

(a) (b)

Figure 5.9: Results of uninformed ‘black-box’ GPs; (a) Model A and (b) Model B. The units are in $\log_{10}$(mm).

Guided wave mean functions

Models C and D in Table 5.4 show the two approaches where mean-function behaviour is included in the model to capture the expected behaviour of the guided waves. Both of these models make use of the third one-dimensional attenuation model from Section 5.2, which includes both geometric spreading and viscoelastic damping. Model C couples this mean behaviour in the radial direction with the flexible polar kernel used in Model B; this allows the GP to learn functional behaviour in both the radial and angular dimensions. Model D is more restrictive and it is assumed that the mean function captures all of the radial behaviour and the GP only models functional behaviour in the angular dimension.

The resulting mean predictions on an independent test set for each of these models are shown in Figure 5.10. Considering the prediction shown in Figure 5.10(a), a ‘banding’ effect is seen as a circular structure centred on the origin. This ‘banding’ is most prominent in areas of propagation across the fibres, and less prominent in the central region, around the wave source. This banding can be explained by considering how the mean function is included in the model. The mean function $m(\mathbf{x})$ is likely to fit the mean of the ρ dimension well as the two dominant attenuation mechanisms are captured in the function. The inclusion of the mean function in a Gaussian process can be imagined as subtracting this function from the relevant dataset. When the mean function captures most of the behaviour, only unstructured data should be left to be modelled by the GP covariance, i.e. the noise in the system. In the results shown here, the mean function fits the data well and the unstructured data along the radial ρ dimension is still modelled in equation (4.14). The GP can still attempt to find structure in unstructured data. An interesting note from this result is that, if there were functional information in the data still to be inferred, this would be picked up by the covariance kernel. In this case, it is believed that the banding artefact may be a result of the GP modelling structure in the noise on this realisation of the measurement; it is expected that if further training data were included, this effect would diminish.

To avoid this issue, and assuming that the mean function models well the radial attenuation behaviour, Model D does not include the radial component in its covariance kernel, so it has covariance given by equation (4.15). The results of training the model with exclusion of the radial kernel can be seen in Figure 5.10(b), in which it can be seen that the banding artefacts are no longer evident. However, the model also appears to lose accuracy as the value of h_m attenuates much more quickly away from the source than is seen in Figure 5.2. The loss of the banding artefacts demonstrates that it is the inclusion of this radial dimension in the kernel which leads to this phenomenon. These models will also be compared quantitatively once all models have been shown qualitatively.

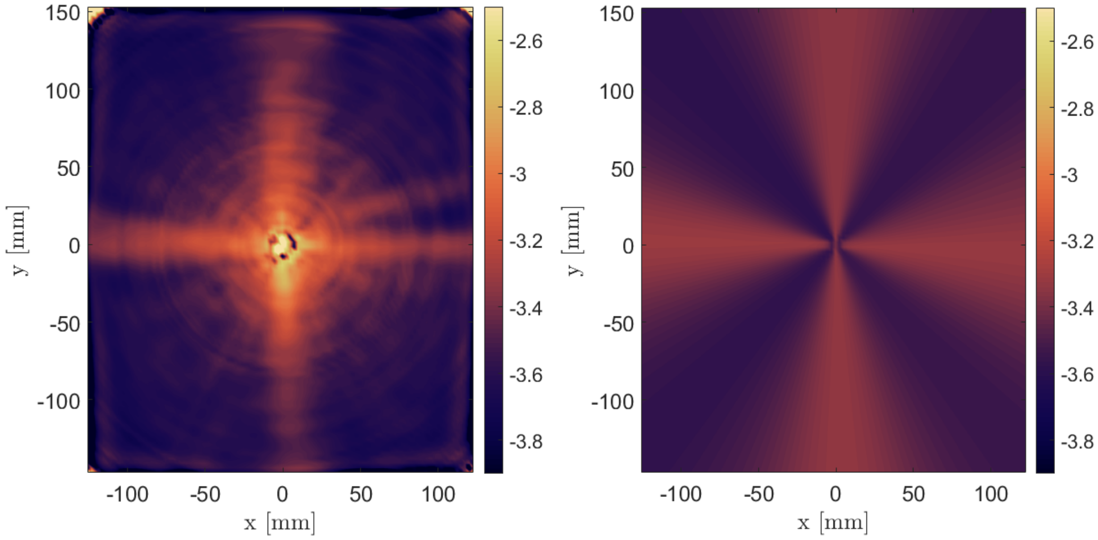

(a) (b)

Figure 5.10: Results of informed model generated using generic kernels and inclusion of a mean function in the GP, with (a) Model C, the full polar kernel, and (b) Model D, the GP only modelling angular behaviour. The units are in $\log_{10}$(mm).

Kernels capturing guided-wave behaviour

The final two models (E and F), attempt to embed understanding of the guided-waves by directly modifying the prior belief in the model via kernel design.

The estimated mean predictions on an independent test set for each of these models are shown in Figures 5.11(a) and 5.11(b). It is clear in these results, how even the small changes between the two kernels can significantly impact the function space that is learnt. Comparatively, Model E (Figure 5.11(a)) leads to a much 'smoother' result in comparison to Model F (Figure 5.11(b)). Fewer high-frequency components are seen in the angular dimension, leading to this appearance. This difference is because of the differences in the prior belief imposed in the angular kernels for each of these models.

An interesting result seen here, is the spreading of energy away from the fibre orientation. This spreading could be physically explained by acknowledging the secondary-guiding characteristics of the fibres themselves. As the waves travel along

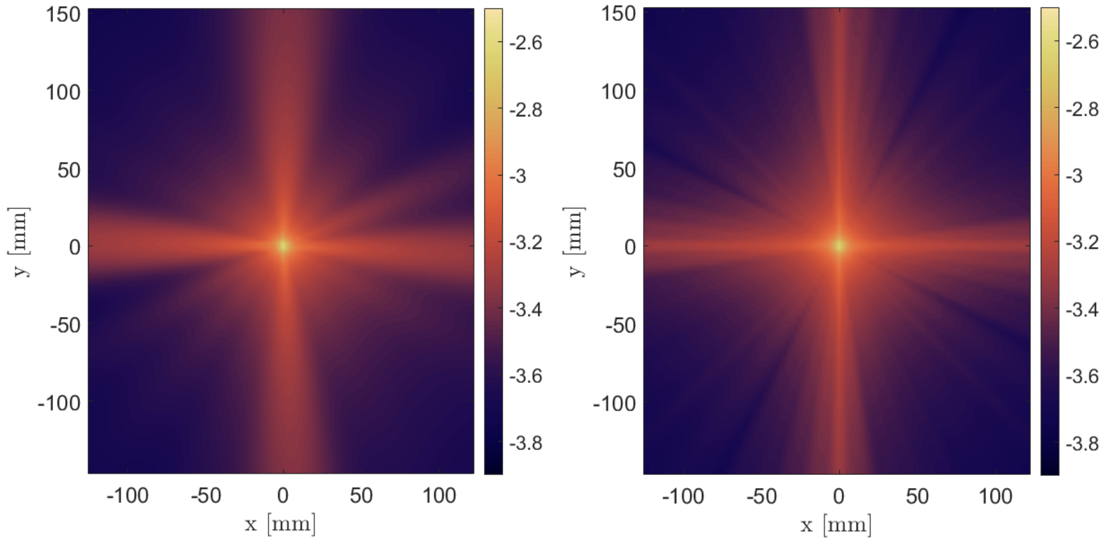

(a) (b)

Figure 5.11: Results of informed model generation using non-generic kernels, here indicating the expected mean function over the entire space when modelling with (a) Model E and (b) Model F. The units are in $\log_{10}$(mm).

the fibres independently, they will lose some energy into adjacent media (i.e. the epoxy matrix). This mechanism will manifest itself as energy spreading in a different direction to the fibre orientation.

Visually, Model E appears to allow the capture of the spreading of the wave energy better. In Figure 5.11(b) it appears that the decay of energy is not captured well and that energy is only propagating along the fibres, not across. The periodicity enforced in Model F is obvious to see in the significantly lower value 'band' at approximately $\theta = \{20°, 110°, 200°, 290°\}$. The kernel used in Model E offers greater flexibility in symmetry, as a result of the additive combination of the SE kernel along the angular dimension. For both kernels, the predictive mean has less variation in the function modelling wave propagation along the fibres, and is a less smooth function when propagating through the fibres. This difference could be improved by increasing the signal-to-noise ratio of the experiment. This alteration will help model areas of high attenuation (i.e. low energy); since the energy of the wave decreases significantly away from the fibre orientation, the value of h_m may not exceed the noise floor.

Currently, in regions with large ρ, the data become unstructured and it is difficult to infer the function with as much confidence.

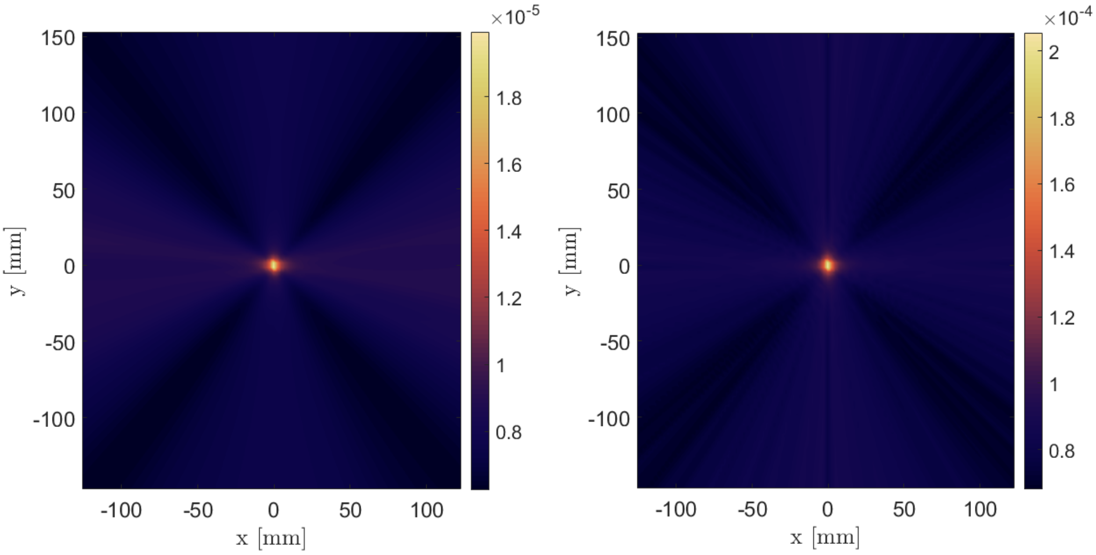

(a) (b)

Figure 5.12: Results of model generation using informed kernels, here indicating the expected variance over the entire space when modelling with (a) Model E and (b) Model F.

For both models E and F, the estimated variance over the surface generates similar results; this can be seen in Figures 5.12(a) and 5.12(b). Both models see a sharp increase in variance towards the centre; this can be explained by examining the one-dimensional attenuation kernel proposed in equation (5.10). The polynomial-kernel equation (5.10) included in these models will result in functions that tend to infinity with $\rho \to 0$. This kernel is used in multiplicative combination with the exponential-decay kernel of equation (5.8), resulting in functions with the same characteristic. The second kernel design results in a slight increase in variance at approximately $\theta = \{50°, 140°, 230°, 320°\}$. From physical interpretation of how fibres affect the energy of the waves, the variance should not increase at this orientation if not also at $\theta = \{40°, 130°, \text{etc.}\}$. For both kernel designs, there also appears to be a greater variance in the energy of the wave when propagating along the fibres; this is likely a result of the short range of θ in which the wave has directly propagated away from the source along a single fibre.

5.3.4 Quantification of model performance

Until now, the modelling approaches for guided-wave features have been compared in a qualitative manner. It has been discussed how certain models give rise to desirable characteristics in the latent functions being learnt, which may obscure the physical behaviour.

Model	$m(\mathbf{x})$	$k(\mathbf{x}, \mathbf{x}')$	LML	PLL_i	PLL_c	NMSE
A	0	$k_{\text{SQE}}(\{x,y\},\{x,y\}')$	24,301	3,745.1	3,770.9	4.424
B	0	$k_2(\{\rho,\theta\},\{\rho,\theta\}')$	50,012	9,964.4	9,975.40	**4.0567**
C	$A_3(\rho)$	$k_2(\{\rho,\theta\},\{\rho,\theta\}')$	19,872	13,047.7	4,221.4	1,037.7
D	$A_3(\rho)$	$k_{\text{W}}(\theta,\theta')$	14,950	11,176.6	3,326.9	29.9
E	0	$k_3(\{\rho,\theta\},\{\rho,\theta\}')$	**96,952**	**21,013.6**	**22,727.4**	9.9422
F	0	$k_4(\{\rho,\theta\},\{\rho,\theta\}')$	75,682	16,274.9	16,291.3	9.9133

Table 5.5: Table of quantitative assessment values for 2D GP modelling strategies tested: the *log-marginal likelihood* (LML), *independent predictive log likelihood* (PLL_i), *co-dependent predictive log likelihood* (PLL_c), and *normalised mean-square error* (NMSE). Best values for each metric are highlighted in bold.

Table 5.5 shows the results of the GP models tested against the metrics previously described. These metrics allow insight into the accuracy and validity of the models, and also provide an opportunity to discuss what might be meant by a "good model". It is important to consider that any given model is only as good as what it will ultimately be used for. In the context of engineering, specifically in NDE and SHM, these models will be used to make operational decisions about the system. As such, it should be considered whether the end user is most interested in the point-wise prediction accuracy, in which case the NMSE is the most appropriate metric. If instead, the models will be carried forward into a risk-driven assessment, then capturing the full uncertainty in the model is important and the correlated predictive log likelihood will be the most appropriate metric. In this work, a number of possible assessment criteria are presented; the onus is on the end user to choose the model which best captures the characteristics of the data/function which are most important to them. It is the opinion of the author that the most robust measure of how well the functional behaviour of the feature space is captured, is the correlated predictive log likelihood PLL_c.

Turning attention to specific results from these experiments, the results for each of the six models under each metric are shown in Table 5.5. It can be seen that models A and B result in the lowest NMSE scores, in other words that their point-wise predictions are closest to the observed test data. This result may be expected since they are the most flexible models. Interestingly, Model B, the informed polar coordinate model, also recovers the highest independent predictive log likelihood. Interpreting this result; if one wants to predict only the behaviour at single points on the plate and is not concerned with the correlation between these predictions, then this is the optimal model (from those tested). It is also seen in the log marginal likelihood LML that Model B captures the behaviour in the training data much better than Model A.

The inclusion of the guided-wave attenuation models as mean functions in the GP (models C and D), appears not to produce desirable effects. These models perform worst in their representation of the training data LML and their point-wise prediction capability NMSE. For this dataset, this is compelling evidence that the inclusion of the guided-wave attenuation mechanisms via a mean function does not lead to a useful model. As discussed, the models may be finding too much structure in the noise of the data used for training, especially Model C. This hypothesis is evident in the very high NMSE score, which would indicate that the model performs considerably worse than taking the mean of the prediction data. However, it is also important to note the exceptionally large NMSE for Model C (representing an error of $\sim$1038%), which is a result of the estimated mean function resulting in a 'singularity' towards the centre of the plate; $m(\mathbf{x}) \to \infty$ as $\rho \to 0$.

Finally, considering models E and F, where the knowledge of the guided waves is used to modify the prior belief in the model via the covariance kernel; both of these models perform very well when considering their ability to model the training data assessed through the LML. When examining their performance on the independent test set, it is seen that the NMSE score is around 9% compared to the 4% of models A and B; this, along with their poor independent predictive log likelihoods PLL_i are indicators that the point-wise predictions from these models are not as good as models A and B. However, in terms of capturing the complete function space, they far exceed all the other modelling strategies. These approaches appear to best capture the underlying functional behaviour of the guided-wave attenuation. For this reason, these models can be considered to be the most suitable for de-noising or spatially up-sampling the data. These two approaches may also be considered the most robust methodologies for modelling the guided-wave behaviour not currently described by governing equations, e.g. outlying behaviour. This advantage has been achieved via incorporation of the physical mechanisms driving the attenuation in the prior specification of the model, via modification of the covariance kernel.

The results from this dataset and model would support the use of Model E for modelling the feature-space of h_m for a guided wave in a CFRP plate. However, when using this strategy, users should consider all models and the system being modelled, as well as the level of physical knowledge that is currently available for said system.

5.4 Chapter Summary

This chapter has presented a methodology for modelling the feature-space of guided-wave propagation in fibre-composite materials using a physics-informed data-driven learner. Initial analysis on the model forms was done by modelling a one-dimensional attenuation model in directions along and across the fibres, the results of which directly influenced the design of the two-dimensional models. The methodology was presented by modelling an energy-based feature, with the models and kernels designed using knowledge of attenuation mechanisms, with varying levels of prior knowledge embedded into the strategy. Based on the probabilistic metrics, the results indicate that modellng the feature-space using a Gaussian process with physical knowledge embedded into the kernels is a promising method. The advantages of using such a method include the models being more extrapolable and generalisable. Though the method was presented on experimental data, it could also be applied to data collected from other methods such as simulation or finite-difference models.

6

Probabilistic Wave Mode Decomposition and Localisation

As the wavelength of ultrasonic guided waves is small, using them for an SHM or NDE strategy would allow one to move up Rytter's hierarchy [1, 2], going from damage detection to assessing location or extent [53]. As discussed in Section 2.4, when Lamb waves interact with damage, they will reflect and scatter [134], causing additional waves to propagate from the damage location. Therefore, any wave captured by a sensor at a given location on a plate with damage, will contain information on the waves directly received from the actuation source, here named *nominal waves*, and any reflections or conversions that are caused by the presence of damage. The received signal will be a superposition of the nominal waves – of which there will be multiple modes – and reflected waves. By decomposing this multi-mode signal into the nominal waves at three given propagation distances, a signal can be constructed which contains only the contents of the signal from reflections. The difference in arrival times of these reflections can be used, along with known wave velocities, to determine the location of the source of the scattering.

Here, a method is proposed, which utilises prior knowledge of the nominal symmetric and antisymmetric modes to obtain reflection signals at a sensor location and use this to triangulate for the source of reflection. Lamb waves were simulated in an isotropic plate using the *local interaction simulation approach* (LISA) [69, 70], for an undamaged plate and a damaged plate. The choice of simulating an isotropic material using LISA was made for several reasons; firstly, as discussed in Section 2.2, LISA has the capability to model complex multi-mode interactions, which presents similar issues for decomposition as some of the unique phenomena in composites. Additionally, the use of an isotropic material creates a simpler approach to the triangulation step by removing the angle-dependent velocity, and this particular step is not the novel contribution of the work. Therefore, using a LISA simulation to model complex multi-mode wave propagation is a suitable method of presenting the overall methodology of probabilistic multi-mode decomposition for damage localisation.

In order to obtain the individual nominal signals of a Lamb wave as it propagates through space, first a full-field multi-mode separation technique was applied, which utilises a forward-backward, two-dimensional Fourier transform (2DFT) method [118] and dispersion-curve information. The simulation is then used to obtain several 'sensor' signals at various locations over the plate, which are treated as *single-source* signals. These decomposed signals are then used to represent the expected nominal wave shape at a given location and are used as the basis for decomposing an individual signal into the nominal and *residual* signals. The reflected waves are contained in the residual signal, determination of the onset of which, gives the time of arrival of the reflection at the sensor. Various combinations of three single-source signals are used to triangulate the location of the reflection source. By using this methodology, it is shown here how damage location in a plate can be determined using a computationally-efficient strategy, and simple equipment.

A Bayesian approach is used for the single-source decomposition stage, which gives a distribution of solutions, and the mean is used as the solution. This probabilistic approach gives a number of advantages:

- The predicted distribution of possible signals allows for improved analysis of residual signals.
- Uncertainty quantification is done at an early stage of the localisation procedure and can be propagated through to the determined location.

- The results produce inherent parametric features which are indicative of energy-based features of UGWs.
- Likelihood estimates can be given to assess the quality of the decomposed signals.

The novelty of the method shown here, in comparison to previous methods is twofold: the determination of a *nominal-wave dictionary*, and the probabilistic approach to the single-source decomposition. The nominal-wave dictionary approach allows the method to be applied to materials where accurate analytical models cannot be formed, such as fibre-composite materials. Previous single-source decomposition strategies rely on a full-field analytical model of the waves as they propagate in a known material, limiting applicability to relatively-simple materials (the most complex being layered composites) and known material properties. The strategy presented in this paper requires only surface displacement along a single propagation path and so can be readily used in analytical, numerical or experimental regimes. The probabilistic approach inherently allows for health-monitoring frameworks to be applied during the localisation procedure; such as, novelty detection and uncertainty quantification. As one aim of the method is for applicability to complex materials, it is also useful to quantify uncertainty in the signal to determine whether residual signals are from additional waves, rather than more complex phenomena such as continuous mode conversion [75, 76].

The overall steps of the work presented here are as follows:

a) Using LISA, simulate propagation of a Lamb wave in a plate under damage-free conditions, giving a known wave field at all points on the surface.

b) Reduce this response data to a subset containing only data along a single propagation direction and use this to determine a ‘dictionary’ of individual wave modes at known propagation distances.

c) Simulate propagation of a Lamb wave in an identical plate under a known damage condition.

d) Extract from this full-field wave data, a subset of single-source signals at known locations.

e) Using a Bayesian linear regression (BLR), decomposition technique, determine the predicted nominal waves at the single-source signal location.

f) Assess the quality of the decomposed signal and determine the residual signal which contains reflected waves.

g) Use the time of arrival of reflected waves with known wave speeds to triangulate the location of the reflection source: i.e. the damage.

This chapter begins by outlining the multi-stage localisation procedure methodology and each stage is described in further detail. The multi-mode decomposition procedure is then shown, along with results of the Bayesian decomposition of the damaged-plate wave signals; discussion is made on the confidence of the decomposed signal, as well as the parametric features obtained. In Section 6.3, the localisation procedure is outlined and Section 6.3.1 shows the results of the one-dimensional localisation to demonstrate the concept of reflection-based localisation. The results of the two-dimensional localisation procedure using the full methodology for various sensor configurations are then shown in Section 6.3.2. The chapter finishes by discussing the results shown and the accuracy of the method, and concluding with how the method leads onto the following chapter.

6.1 Methodology

The overall methodology for the localisation technique presented here is shown in the flowchart in Figure 6.1. The first key process comprises a *full-field* decomposition, which uses the surface displacement data along the one-dimensional propagation path of the wave. Data for this stage can be collected from either simulation or experiment, the latter using a scanning-laser doppler vibrometer (SLDV). The second key process is the *single-source* decomposition, meaning decomposing a signal from one location, such as the voltage reading of a piezoelectric transducer. Section 6.1.3 begins here by explaining the details of the full-field multi-mode separation, which uses a forward-backward two-dimensional Fourier transform approach of masking the experimentally-determined dispersion curves. This stage produces a *nominal-wave dictionary* which provides the expected signal of individual wave modes for a given propagation distance. Section 6.1.4 details the single-source multi-mode separation method, which uses Bayesian linear regression (BLR) to attain a probabilistic distribution of the expected waves. Finally, Section 6.1.5 explains the triangulation procedure, and how the times of arrival of the reflected waves are determined using the Akaike Information Criterion (AIC).

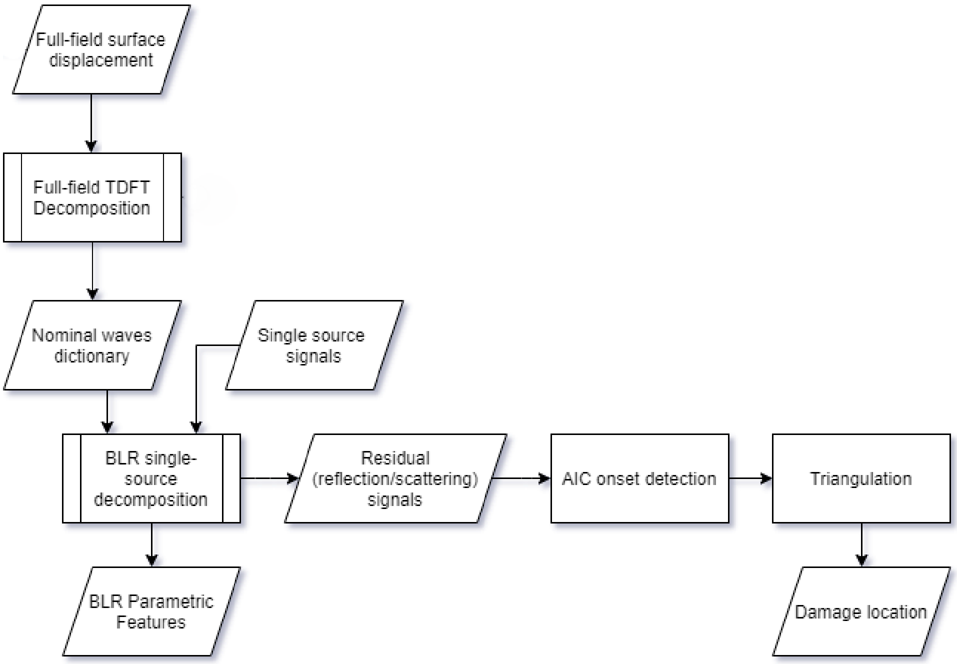

Figure 6.1: Localisation methodology.

6.1.1 LISA Simulation

For the work in this chapter, guided waves were simulated using the local interaction simulation approach (Section 3.6), as this captures the multi-mode wave signals well. Lamb waves were simulated in an aluminium plate, the details of which can be found in Table 6.1. First, a wave-field was simulated in an undamaged plate, then the simulation was repeated with a 1mm square, half-thickness notch at $x = 75$ mm, $y = 150$ mm. The choice of using a square notch, as opposed to a more physically-common circular notch, is the relatively large cell width in comparison to the wavelength, and so in the cell-width scale, a smooth shape is not possible.

The location of the notch was chosen based on allowing analysis of the wave in propagation directions collinear with the source and at various reflection angles. By having the damage in a propagation path directly along cell edges from the source, this allows both more and less complex simulation interaction. For all simulations, the actuation source is a 20mm diameter piezo-electric transducer placed at the centre of the plate, with a 1MHz, five-cycle, Hanning-windowed sine wave. This source is represented using a linear systems model [70]. The results of the damaged and undamaged plate simulations can be seen in Figure 6.2.

Material	Aluminium
Density, ρ	2710 kg/m^3
Longitudinal sound speed, c_L	6420 m/s
Transverse sound speed, c_T	3040 m/s
Width x Length	300 mm × 300 mm
Plate thickness	1 mm
Cell dimension, ε	0.25 mm
Time step, τ	0.01496 µs

Table 6.1: Properties of Lamb wave in plate simulation performed using LISA approach.

Figure 6.2 shows how the LISA simulation accurately models the effect of damage on the wave propagation, as the reflections of the A_0 mode can be clearly seen. It can also be seen how the boundaries reflect the waves; this is an important consideration in the method, as this can have effects on the technique, as will be discussed later.

6.1.2 Data sources

The aim of this subsection is to detail the source of the data used in this work at each stage of the methodology. All data used here are taken from the LISA simulations described in Section 6.1.1. The simulation provides the full wave-field information for all points on the surface of the plate, then data are extracted at each stage to represent the minimum data required for this stage. For the full-field multi-mode

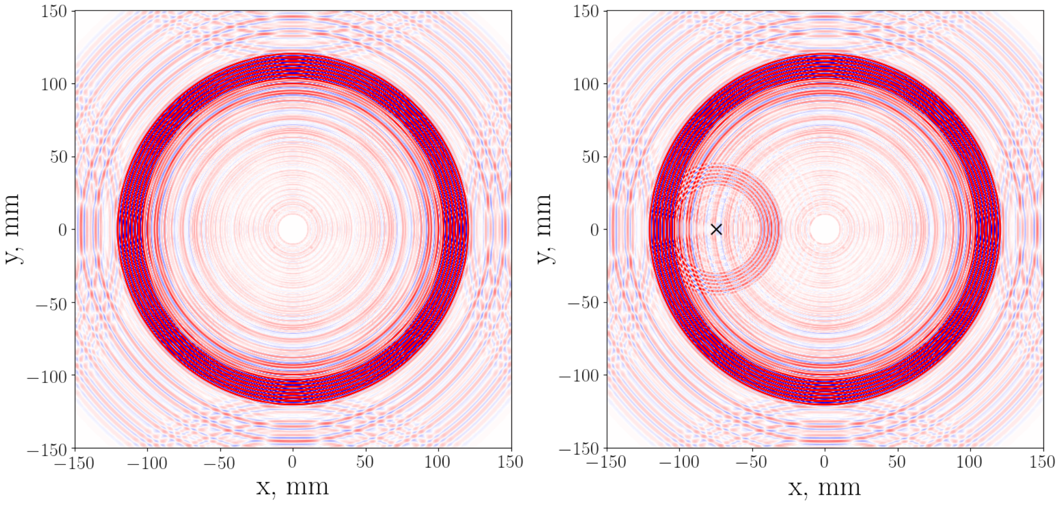

(a) (b)

Figure 6.2: Surface displacement results of LISA simulation for: (a) an undamaged plate and (b) a damaged plate (on which the location of damage is indicated by the black cross), 35µs from the beginning of the actuation signal. Dimensions are shifted to place the actuation source at the origin.

separation stage, surface displacement is taken from the undamaged plate simulation at regularly spaced intervals of 0.25 mm along the propagation path -90° from the origin (refer to Figure 6.3). This subset gives full-field propagation data of the wave as it travels along one direction. For the single-source decomposition, the 'sensor signals' are the surface displacements taken from the damage-state simulation at single points. These data are referred to as 'measured signals', as they represent what would be recorded using PZT sensors in application. Figure 6.3 shows the locations of the sensor signals on the plate simulation outlined in Section 6.1.1. The sensor locations were chosen to give a variety of propagation and reflection angles, but not to be too close to the edge of the plates, as boundary reflections will interfere with the signal. For the purposes of sensor location description, the direction of the path between the actuation source and the damage is herein referred to as the actuator-damage direction, and the direction of the path between a sensor and the actuator is the incident direction of that sensor. The angle between these two directions is referred to as the reflection-incident angle (RIA). Sensor A has an RIA of 0°, sensors B and C have an RIA of 45°, sensor D has an RIA of 30°, sensor E has an RIA of 135°, and sensors F, G and H have an RIA of 60°. In order to localise a reflection source over a 2D plane, a minimum of three sensors is needed [102], so during the localisation step various combinations of three sensors from the eight possible were chosen.

The plate simulated in this paper is relatively small, and so there is a quick superposition of reflected waves within the signal at points further from the damage. In practice, the user must take careful consideration of reflective characteristics of the system, such as complex geometrical features, though this is a consistent trait of guided-wave based systems [102].

6.1.3 Full-field multi-mode separation

Separation of multi-mode signals of a Lamb wave over its propagation in space is carried out by a forward-backward method using the experimentally-determined dispersion curve. First, the dispersion curve must be obtained by spatially sampling the surface displacement of a Lamb wave as it propagates through a bounded medium; then one performs a *two-dimensional Fourier transform* (2DFT) along time and distance sequentially [118],

$$U(f,k) = \int_{-\infty}^{\infty}\int_{-\infty}^{\infty} u(t,x)e^{-i2\pi(ft+kx)}dtdx \tag{6.1}$$

where $u(t,x)$ is the surface displacement with respect to time t and distance x. In the discrete form, this approach uses a *two-dimensional fast Fourier transform* (2DFFT) algorithm,

$$U[m,n] = \sum_{m=0}^{M-1}\sum_{n=0}^{N-1} u[m,n]e^{-i2\pi(fm/M+kn/N)} \tag{6.2}$$

where M and N are the number of data points in time and distance respectively. From the simulation data described in Section 3.6, surface displacement data were extracted along a single propagation path. The spatially-sampled signals are normalised, based on dividing each signal by the maximum amplitude of the signal, and then passed through the 2DFFT algorithm to generate the [f-k] space. The resulting image data,

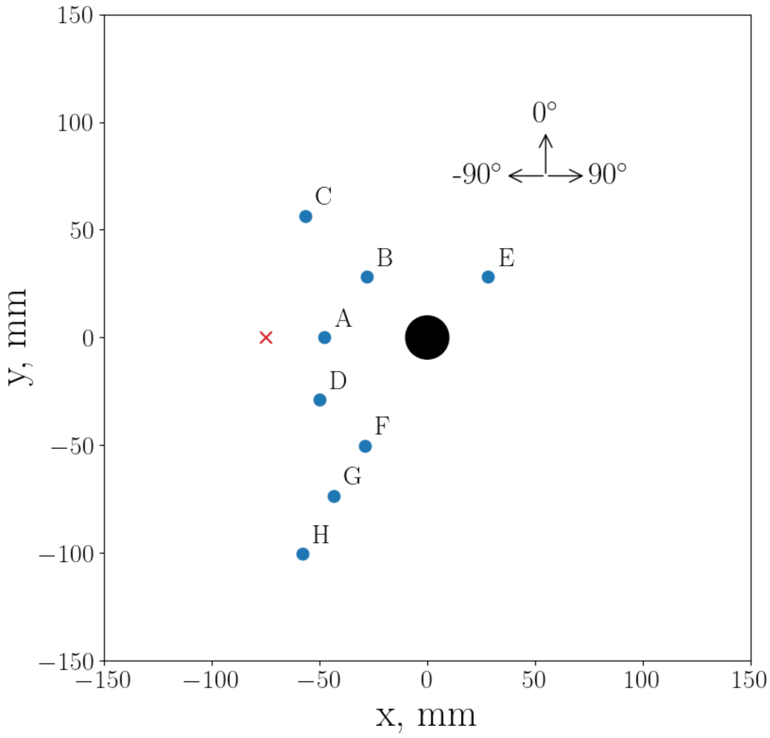

Figure 6.3: Sensor locations used for two-dimensional localisation; the black circle indicates the location of the PZT actuator, the blue circles indicate the locations of the 'sensors' and their labels, and the red cross indicates the location of the damage. The arrows show the references for the direction of wave propagation from the actuator.

which show dispersion-curve information, are shown in Figure 6.4. For the purposes of visualisation and ridge extraction, the [f-k] space is expressed in terms of its magnitude, using a log transformation,

$$P(f,k) = 20\log_{10}(1 + |U(f,k)|) \tag{6.3}$$

Several distinct modes can be seen in the experimentally-determined dispersion curve in Figure 6.4(b). In order to separate the modes, the equivalent curves must first be extracted from the image data. The extraction was done here using a simple ridge-picking algorithm, which extracts local maxima as points of the curve. The algorithm considers each pixel in the image and subtracts the mean of the surrounding

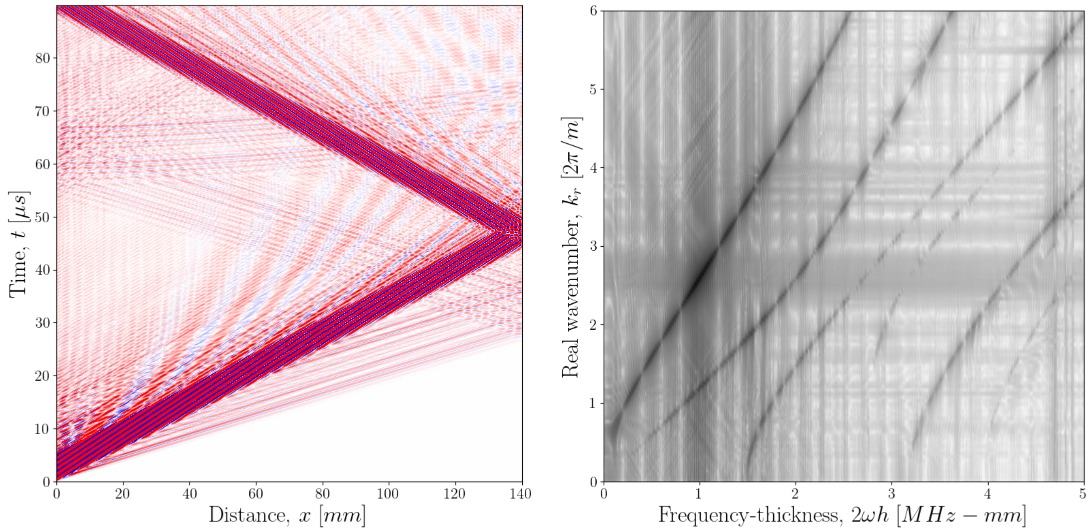

(a) (b)

Figure 6.4: Example of dispersion information determined from a 2DFT by extracting an example of the [t-x] data from the LISA simulation, shown in terms of (a) $u(t, x)$ and (b) $P(f, k)$

L^2 pixels; it then normalises the data and sets any point with a value below or equal to 50% to 0, and any above 50% to be 1. The resulting Boolean image data, D, are then used to extract the curves from the complex 2DFFT data by simply performing an element-wise multiplication,

$$U_* = D \circ U \tag{6.4}$$

In order to reduce loss of information as much as possible from the [f-k] space, a buffer of $\pm a$ and $\pm b$ additional data points, in the horizontal and vertical directions respectively, are set to be 1 in D. The Boolean mask D must be the same size as U, and it is important to select modes that appear on the full 2DFFT data which represent the negative frequencies and wavenumbers in the transform; this can be done by simply returning the mirrored indices from the ridge selection process. D can also be tuned to include any number of selected modes, to determine which will be included in the reconstructed signal. Once these curves are extracted, they can be used to reconstruct individual, or selected, modes by applying an *inverse* *two-dimensional Fourier transform* (I2DFT) to the new image data,

$$u_*(t,x) = \int_{-\infty}^{\infty}\int_{-\infty}^{\infty} U_*(f,k)e^{i2\pi(ft+kx)}df\,dk \tag{6.5}$$

or in discrete matrix form using an *inverse two-dimensional fast Fourier transform* (I2DFFT),

$$u_*[m,n] = \sum_{f=0}^{M-1}\sum_{k=0}^{N-1} U_*[f,k]e^{i2\pi(fm/M+kn/N)} \tag{6.6}$$

The modes that are included in the reconstructed signals were chosen here based on comparison to numerical results of dispersion curves determined using DISPERSE [117]. The resulting decomposed waves were then stored as a *nominal-wave dictionary* (NWD) for use in the single-source decomposition stage. Although the signals are normalised at each distance, it is trivial to return the range of the decomposed signals to that of the measured signal by storing the normalisation parameters. For this work, the signal data are kept at the normalised values, as the decomposition method is focussed on just the *shape* of the expected nominal signals and not their amplitude. The full-field multi-mode stage is summarised in Algorithm 1.

6.1.4 Single-source multi-mode separation

After the *nominal-wave dictionary* was determined and stored, it was used to decompose a Lamb-wave signal from a single-source into the nominal and residual signals. This method uses a Bayesian linear regression (BLR) technique, as described in Section 4.1.

For the purposes of this work, the model of the form,

$$y(x,t) = \mathbf{w}(x)^{\top}\phi(x,t) + \varepsilon, \qquad \varepsilon \sim \mathcal{N}(0,\sigma^2) \tag{6.7}$$

uses basis form $\phi(x,t) = \{y_{A_0}(x,t),\ y_{S_0}(x,t)\}$, where $y_i(x,t)$ is the surface displacement of the normalised nominal wave, for mode i, at propagation distance x, and time point t. Here, $\mathbf{w}(x)$ is the vector of weights for propagation distance x, and ε is a noise parameter with normal Gaussian distribution $\mathcal{N}(0,\sigma^2)$.

The nominal waves are also re-normalised to their individual ranges in order to better compare the predicted weights between the wave modes. One could consider ϕ to

Algorithm 1: *Full-field multi-mode separation.*

```
Input  : Multi-mode surface displacement signals over propagation distance $u$,
         initial guess of lowest $FTP$ and $k$ on dispersion curve for each mode $g$.
Output : Individual nominal-wave dictionary over propagation distance $u_*$.

for Distance point $n$ do
    Normalise signal $u(:,n) \rightarrow \hat{u}(:,n)$, storing peak-to-peak range $PTP(i)$;
end
$U = 2DFFT(\hat{u})$ using equation (6.2);
Power transform of $U$: $P = 20\log_{10}(1 + \mathrm{abs}(U))$;
Ridge finding: get locations in $P$ where the normalised value is greater than 50%
  above the mean of the surrounding $L^2$ pixels;
for Wave mode $g$ do
    Curve selection: from initial guess of $\omega$ and $k$ for each mode, continuously
      select ridge points that are all less than $d_\omega$ and $d_k$ away in frequency and
      wavenumber respectively, set these locations in $D$ to equal 1;
    Flatten dispersion curve image using equation (6.4);
    Reconstruct time-distance data for individual modes using equation (6.6) and
      store in $u_*(g,:,:)$;
end
```

be the decomposition of the expected nominal signal into the selected modes. For this work, only the fundamental modes are used, although it would be trivial to use the same method on more selected modes. The expected weight parameters **w** will give relative amplitudes of the nominal waves, directly influenced by the range of y_i. For this method, any signal range can be used, although it is preferable to use a normalised signal for computational reasons. Normalising the signals also allows for accounting of attenuation effects, which would distort the dispersion image data resulting from the two-dimensional Fourier transform.

The signal is first normalised based on the range of the signal,

$$\mathbf{y}^* = \frac{\mathbf{y}}{\text{range}(\mathbf{y})} \tag{6.8}$$

where range($\mathbf{y}$) = max($\mathbf{y}$) − min($\mathbf{y}$), is the peak-to-peak range of measured signal $\mathbf{y}$. The value of range($\mathbf{y}$) is stored and the calculated weights are multiplied by this range to present them in terms of the signal amplitude in m. An example of the nominal-wave dictionary signals used to decompose a measured signal on the damaged plate is shown in Figure 6.5.

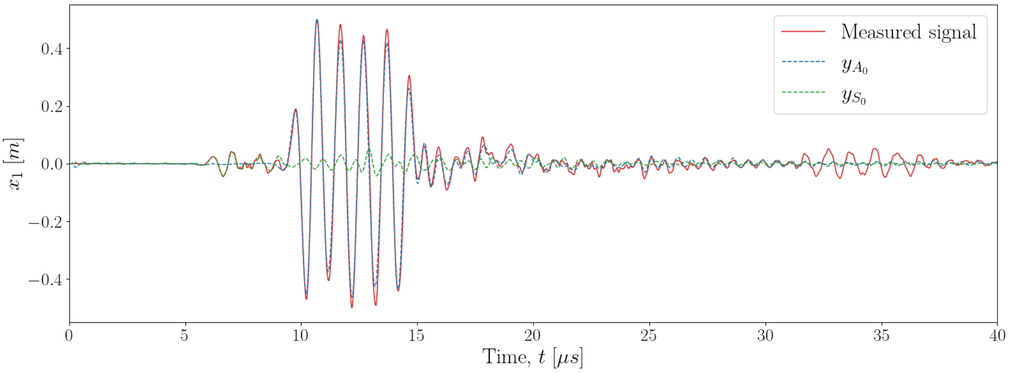

Figure 6.5: Example nominal-wave dictionary signals y_{A_0} and y_{S_0}, at a propagation distance x of 50mm, compared to the measured signal in the damage-state simulation. The dictionary signals are in their normalised values directly from the full-field decomposition and the measured signal is normalised using equation (6.8).

For this work, qualitative assessment is made of the predicted signal using the *predictive log likelihood* as described in Section 4.2.4. The single-source decomposition process is summarised in Algorithm 2.

6.1.5 Reflection source triangulation

Once the signals are decomposed into their individual nominal modes, the residual signal can be calculated,

$$\mathbf{y}_{res} = \mathbf{y} - \tilde{\mathbf{y}} \tag{6.9}$$

where $\mathbf{y}$ is the measured signal and $\tilde{\mathbf{y}}$ is the predicted nominal signal. This residual contains information on reflected/scattered waves because of damage. In order to

Algorithm 2: *Single-source multi-mode separation.*

```
Input  : Individual nominal wave dictionary over propagation distance $u_*$,
         measured signal $\mathbf{y}$ at propagation distance $\hat{x}$.
Output : Predicted nominal wave signal at measured signal location $\tilde{\mathbf{y}}$,
         predicted variance of nominal wave signal $\sigma^2$.
Normalise measured signal $\mathbf{y} \rightarrow \mathbf{y}^*$, storing peak-to-peak range $PTP$;
Load wave mode signals for distance point $\hat{x}$ from nominal wave dictionary
    $u_*(:, :, x_*)$ based on $x_* = \mathrm{argmin}(x - \hat{x})$;
Sum across modes to form the basis expansion $\mathbf{X} = \phi(x, :)$;
Calculate analytical solution of weights $\mathbf{w}$ and predicted variance $\sigma^2 = \mathrm{diag}(\mathbb{V})$;
Reconstruct predicted nominal signal $\tilde{\mathbf{y}} = \mathbf{w}^\top \mathbf{X}$
```

triangulate the source of this reflection, the time of arrival at each sensor must first be determined. Previous work [135], has shown a simple, yet effective technique using the Akaike Information Criterion (AIC) [136] to determine arrival times. The AIC function compares signal entropy before and after each time t in a time series. When time t is aligned with the signal arrival, the similarity between the high-entropy uncorrelated noise prior to t, and the low-entropy structured signal after t is at its lowest and the function returns a minimum. Therefore, a simple minimum-finding function can be used to determine the location of the onset of a signal. The AIC of a signal x, for a given time point t, is given by,

$$AIC(t) = t \log_{10}(\mathbb{V}[x_{1:t}]) + (T - t - 1) \log_{10}(\mathbb{V}[x_{t:T}]) \tag{6.10}$$

where $\mathbb{V}[x_{j:k}]$ is the classic variance of x from point j to point k, and T is the final time point in the series. For detection of reflection onset only, the portion of the signal after arrival of the slowest nominal wave was used. This selection is because onset detection by AIC is based on a change in entropy ratio in the signal before and after the onset, and there is increased structure in the residual at the nominal wave portions.

This onset then gives a reflection time of arrival at each sensor t_{ref}. It is useful to look at the problem of localising with a sensor along the propagation path between the actuation source and the damage. For this one-dimensional localisation problem, the distance of the reflection source from the sensor can be calculated simply as,

$$d_r = \frac{1}{2}\frac{t_{ref} - t_{A0}}{c_{A0}} \tag{6.11}$$

where t_{A0} is the time of arrival of the nominal A_0 mode at the sensor and c_{A0} is the group velocity of the A_0 mode. It should be noted that this may not be a useful method in practice, as it is unknown whether the sensor, actuator and damage are collinear. Furthermore, equation (6.11) is only applicable when the sensor is earlier in the propagation path, because in locations after damage there are no additional waves, but only converted/reduced energy modes, as can be seen in Figure 6.2(b). The one-dimensional procedure is included to show a simple illustrative example of localisation, as well as providing an initial stage to assess the decomposition-based approach to localisation. This stage is also included to allow the reader to gain intuition on the procedure, and how a usable algorithm could be developed on this basis; a two-dimensional example of which will be demonstrated later.

Now consider the problem of locating using reflected signals in a 2D plane, a diagram which aids in understanding this procedure is shown in Figure 6.6. As the Lamb wave is propagating in an isotropic, homogeneous structure, the difference in time of arrival between the sensors and wave velocity c (prior knowledge), can be used to triangulate for the source of the wave [101,102]. For three sensors, first the reflection time of arrival for sensors 1, 2 and 3 are denoted as $t_{r,1}$, $t_{r,2}$ and $t_{r,3}$ respectively. The exact time of the reflection from the damage t_0 is unknown, and therefore so is the time taken for the reflected wave to travel from the damage to the sensors. These unknown times are denoted t_1, t_2, t_3 and the distance from the damage to each sensor is given by,

$$d_i = c \times t_i \tag{6.12}$$

As t_i is unknown, d_i cannot be calculated from equation (6.12). However, the difference in time of arrival (dTOA) between two sensors t_{ij} provides the difference in distance between the damage location and sensors i and j,

$$d_{ij} = c \times t_{ij} = c \times (t_i - t_j) \tag{6.13}$$

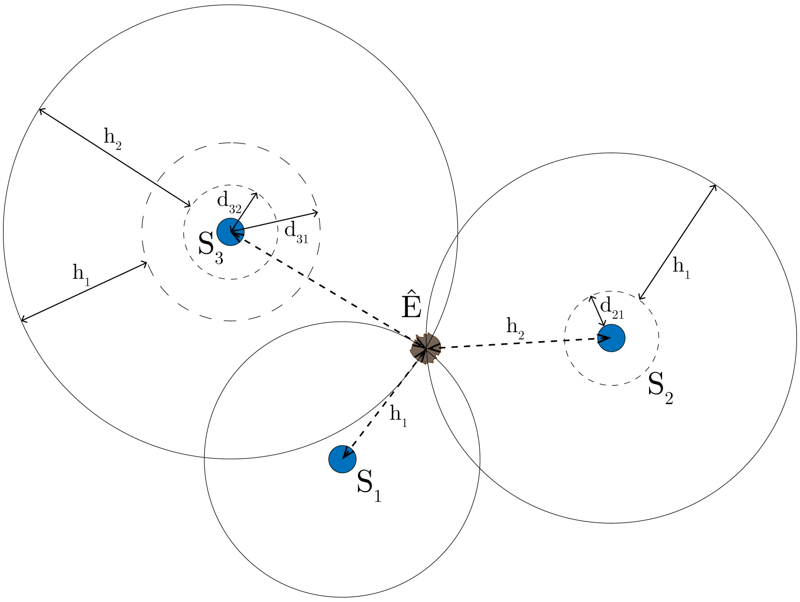

Figure 6.6: Diagram showing distances which are used in triangulation via wave signals reflected from damage.

In this work, the triangulation of the reflection source is framed as an optimisation problem, as shown in [137]. In this sense, the source location is estimated by minimising the difference between the recorded dTOA and a calculated value originating from a trial source position. In practice, this was done by defining a cost function,

$$J = \sum_{i,j} \left(t_{ij} - \frac{|E - S_i| - |E - S_j|}{c} \right)^2 \tag{6.14}$$

where E is a trial location of the reflected signal source and $|E - S_n|$ is the Euclidean distance between this trial location and the location of sensor n. An estimate of the location of the reflection source was then determined by,

$$\hat{E} = \text{arg min}(J) \tag{6.15}$$

In this work, this minimisation uses the Nelder-Mead method [138]. The reflection triangulation process using various sensor locations is summarised in Algorithm 3.

The algorithms are shown individually here for each stage, but work concurrently in practice and data are fed from through each in order. Firstly, the full-field wave

Algorithm 3: *Reflection source triangulation.*

```
Input  : Measured signal at various locations $\mathbf{y}$, nominal-wave dictionary over
         propagation distance $u_*$.
Output : Predicted location of reflection source $\hat{E}$.

for Measured signal of sensor $i$ do
    Decompose signal using algorithm 2 to retrieve predicted nominal-wave signal
      $\tilde{\mathbf{y}}$;
    Construct residual signal using equation (6.9);
    Determine onset of reflection using AIC $\rightarrow t_i$;
end
Minimise equation (6.14) using Nelder-Mead method to determine predicted
  location $\hat{E}$;
```

propagation data are fed into Algorithm 1, from which the nominal-wave dictionary u_* is returned. This dictionary is then fed into Algorithm 2, along with the single-source signals from each sensor $\mathbf{y}_i,\ i = 1, 2, 3$, and the predicted nominal signals $\tilde{\mathbf{y}}_i$ are returned. The predicted nominal signals are then used in Algorithm 3 to return the predicted location of the damage, $\hat{E}$.

6.2 Multi-mode decomposition

To begin, it is useful to analyse and evaluate the probabilistic decomposition of the full-field propagation and single-source signals. This section initially looks at the decomposition of the full-field signal as shown in Section 6.2.1, and then at various distances along the propagation path collinear with damage, the results of which are shown in Section 6.2.2. Decomposition results at other propagation angles are then explored at the same distance, all from the damaged plate, in Table 6.2.

6.2.1 Full-field decomposition

The results of passing the data shown in Figure 6.4(b) through the ridge-picking algorithm are shown in Figure 6.7(a). By comparing the dispersion curves generated using equation (6.1) to those generated with 'DISPERSE', it can be seen which individual wave modes correspond to each ridge. The dispersion curves seen in the image data taken from the 2DFFT show mostly good correspondence with those calculated numerically, discrepancies between them are a result of the cells per unit wavelength [70].

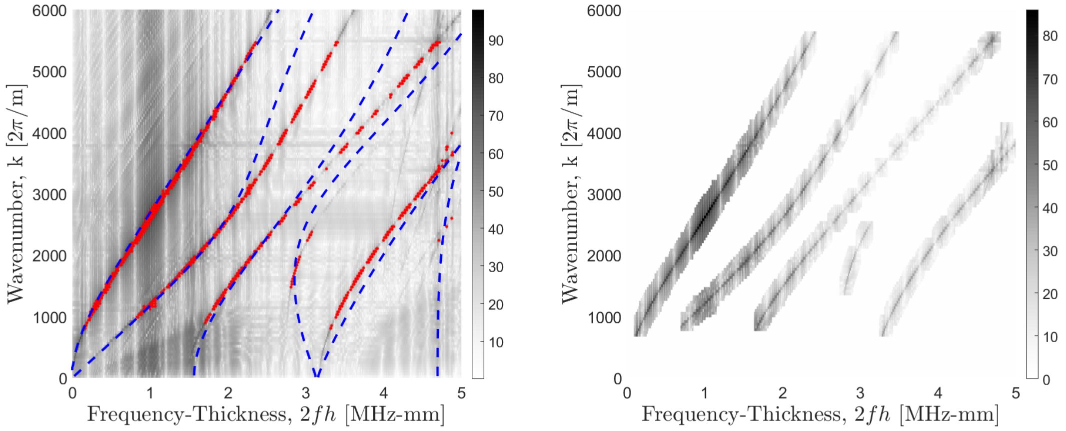

(a) (b)

Figure 6.7: (a) Point data of individual modes found using the ridge-picking algorithm (red circle markers), and compared to data from 'Disperse' (blue dashed line). These lines are representative of (in order of appearance with increasing $2fh$), the A_0, S_0, A_1, S_1, S_2 and A_2 modes. (b) Separated dispersion curves, extracted using a buffer of $a = 11$ and $b = 3$.

After comparing the extracted ridges with the numerically-determined dispersion-curve data to label the curves selected, the image data are flattened for each mode using equation (6.4). The separated mode data, H_*, are shown in Figure 6.7(b) in terms of $P(f, k)$, with the A_0, S_0, A_1, S_1, S_2 modes selected.

The full-field wave dictionary u_* was then generated by passing each flattened mode through equation (6.5) in series. The total reconstructed time-distance space can be seen in Figure 6.8, and individual time signals at a propagation distance of 10mm in Figure 6.9. In comparison to the original data in Figure 6.4(a), the reconstructed $[t\text{-}x]$ space is missing a larger wavelength component which is likely to be a mode that is not visible in Figure 6.7(a). From Figure 6.9, it can be seen that the relative amplitudes of the individual wave modes are preserved throughout the separation. As the amplitudes of the A_0 and S_0 modes are significantly larger than the higher-order modes, it is reasonable to only take these two modes forward to be used in the separation. The amplitudes of the A_0 and S_0 modes are larger because the excitation frequency is tuned to only capture these modes on the dispersion curves. Practically, this is also reasonable as the reflected signals will be from the fundamental modes also, and will be of larger amplitude than the additional modes. Thus the nominal-wave dictionary u_* is reduced to $u_*\{A_0, S_0\}$.

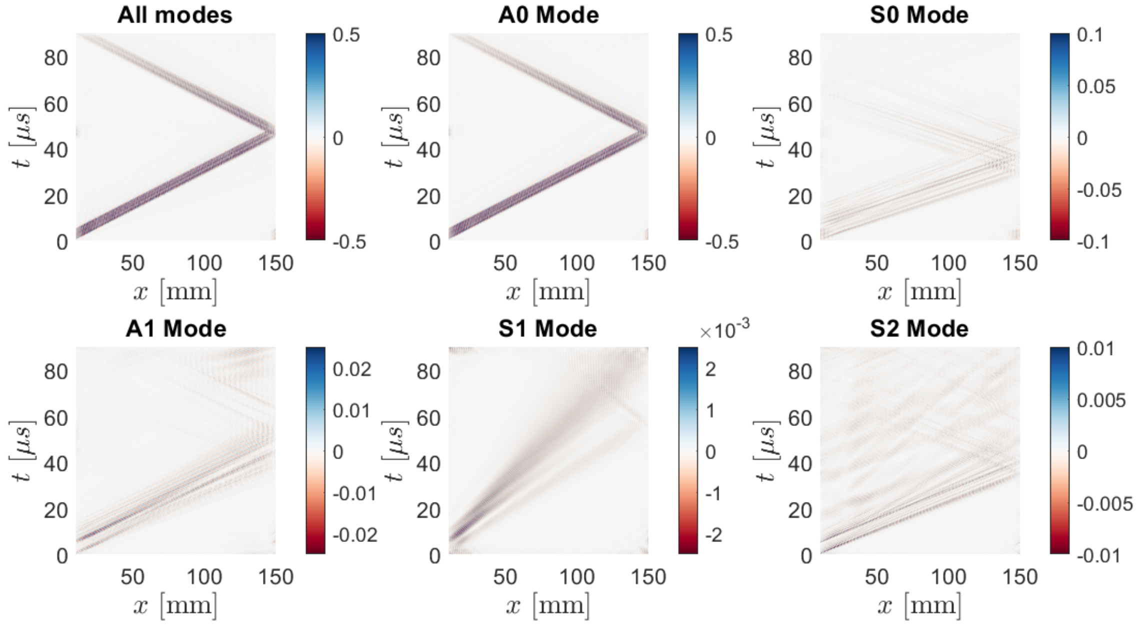

Figure 6.8: Reconstructed normalised time-distance spaces using inverse 2DFFT for all modes together, and each mode individually.

Figure 6.9 also shows that the A_0 mode is the most influenced by the actuation signal, and is the signal which retains the shape of this most. This observation can be explained by examining the dispersion curves; the actuation source was driven at

300kHz-mm, at which there are only two solutions for the wavenumber, the A_0 and S_0 modes. Therefore, the actuation of higher-order modes is because of excitation of wavelengths of the fundamental modes.

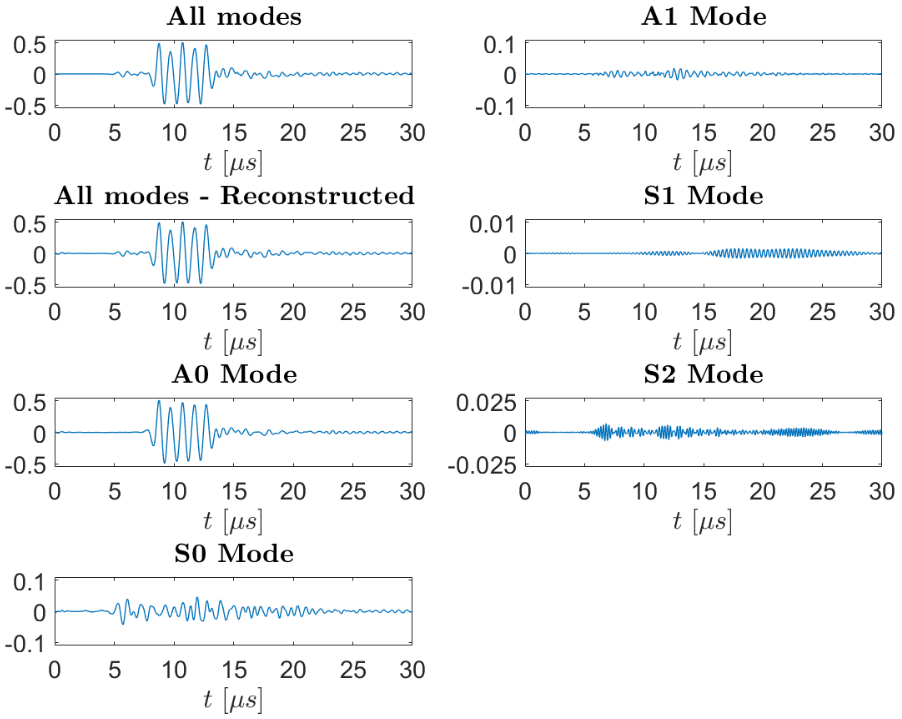

Figure 6.9: Individual normalised signals taken from propagation distance of 50mm for original data and reconstructed signals for all modes together and each mode individually.

In most Lamb-wave studies, in order to model or measure the behaviour of wave modes individually, the structures are excited with a tuned actuation (both in frequency and mode shape) to excite specific modes. Although this idea works well, it is much more difficult to excite higher-order modes individually, particularly in experimental regimes. This problem is because of the increased number of modes which have overlapping frequency-wavenumber bandwidths, as well as similar mode shapes. Using the method shown here, generating the signals for individual wave modes is both simpler and less costly (in terms of time and total computation), as less actuation models must be performed.

Other methods of wave-mode separation include using a physics-based approach of utilising amplitude ratios of anti/symmetric modes [107]; in order to use this however, accurate prior knowledge of the system is required. A particular advantage of the method proposed here is for use in the study of complex materials, for which models are difficult to obtain and validate to an accurate enough degree to reasonably use for the amplitude-ratio method. More on using this method for decomposing Lamb waves in composites is shown and discussed in Chapter 7. Another strategy for mode separation when no prior knowledge is available, is to use machine-learning methods, such as independent component analysis. This approach has been shown to work well, but data-based decomposition methods can present disadvantages such as reconstructed signals being 'down-sampled' in comparison to the originals, and lack of physical insight can limit applicability.

6.2.2 Single-source decomposition

At this point, it is useful to analyse and evaluate the probabilistic decomposition of a single-source signal. This section aims to do so by initially looking at the decomposition at various distances along the propagation path collinear with damage, the results of which are shown in Figures 6.10 and 6.11. Decomposition results at other propagation angles are then explored at the same distance, all from the damaged plate, in Table 6.2.

The calculated weights from the BLR decomposition are shown in Figure 6.10, where the weights are written as the corresponding weight for each mode, w_{A0} and w_{S0}. The propagation location in which there is damage is given by the filled red area in Figure 6.10(b). These weights can be interpreted as parameters relating the shape of the expected nominal wave to the range of the measured nominal wave. It is clear to see the attenuation of each mode as the propagation distance increases, although an interesting point to note, is the sharp drop in the antisymmetric parameter w_{A0}, after the wave has propagated through the damage. There is a periodic nature to the weights with respect to the propagation distance; this is likely to be because of reflected waves coming in and out of phase with the nominal waves. The superposition of these waves will affect the amplitude of the nominal waves as the phase differences

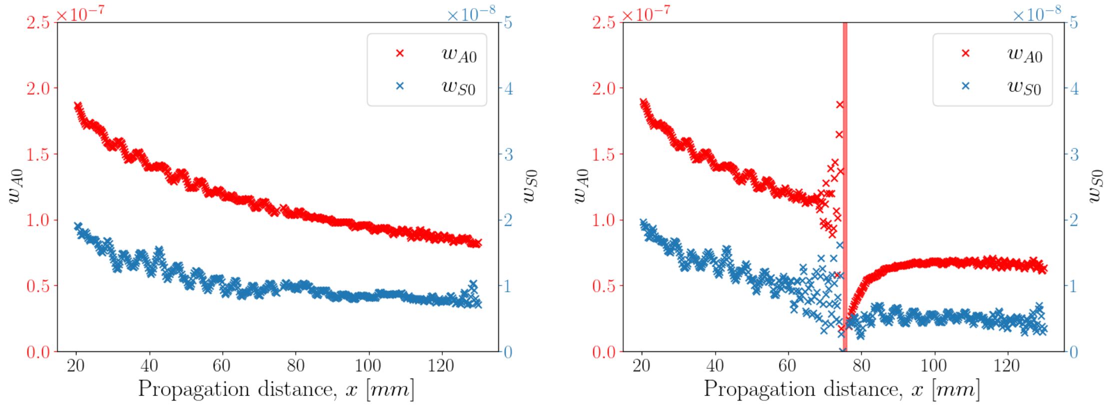

(a) (b)

Figure 6.10: Weights representing each mode extracted from BLR decomposition applied at various propagation distances for: (a) the undamaged plate and (b) damaged plate. In (b), the section of propagation in which there is damage is given by the vertical filled red area.

between the waves change.

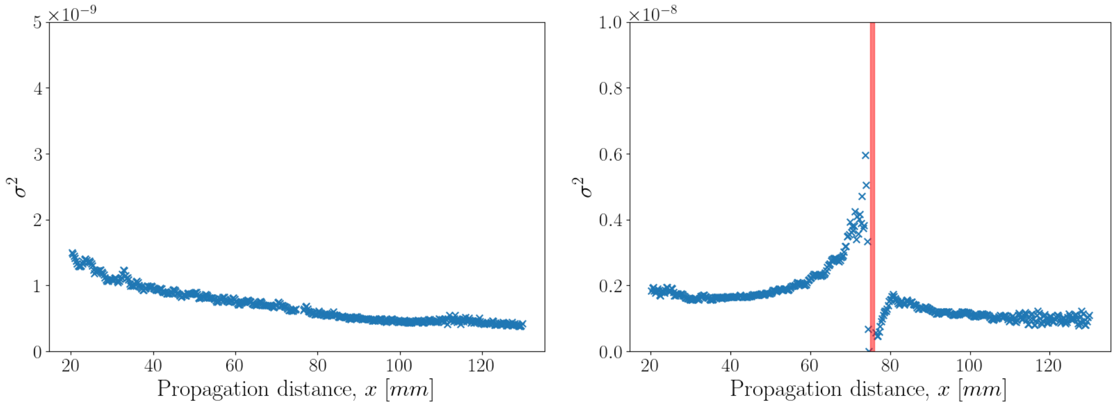

(a) (b)

Figure 6.11: Predicted variance of nominal waves extracted from BLR decomposition applied at various propagation distances for: (a) the undamaged plate and (b) damaged plate. In (b), the section of propagation in which there is damage is given by the vertical filled area.

Figure 6.11 shows the predicted variance of the decomposed signals at each propagation distance. An initial observation is of the increased predicted variance when decomposing signals in the plate containing damage. Furthermore, in Figure 6.11(b) the predicted variance appears to increase as one moves closer to the reflection source, and there is a sharp drop afterwards. This trend can be explained using the information viewed in Figure 6.10(b); as the amplitude of the nominal wave decreases closer to the damage, and any reflected waves will also attenuate further away from damage, the relative influence of the superposition of reflected waves will increase closer to damage. However, past the damage there is no reflection in one plane, instead there is mode conversion. Therefore, the predicted variance will drop along with the magnitude of the predicted weights as seen in Figure 6.10(a).

Angle	Distance	w_{A0}	w_{S0}	σ^2	PLL
-90°	50mm	1.397e-07	1.337e-08	1.645e-09	-1.946e+09
90°	50mm	1.396e-07	1.228e-08	9.624e-10	-4.207e+08
-45°	50mm	1.157e-07	1.073e-08	3.224e-09	-2.152e+09
-60°	50mm	1.184e-07	5.359e-09	2.773e-09	-6.516e+08

Table 6.2: Resulting metrics from the BLR decomposition of single-source signals at various locations over the damaged plate, noted by their propagation angle and distance. A propagation angle of -90° is the direction of damage from the actuation source. Here, w_{A0} and w_{S0} represent the weight parameters to construct the nominal signals of the A_0 and S_0 mode respectively.

Surface displacement signals were taken from the damaged plate at various propagation angles, and the decomposition technique was applied to each of these. The resulting metrics returned by the technique are shown for each signal location in Table 6.2. A notable observation from these results is of the increased uncertainty when decomposing signals not taken along the same propagation angle at which the full-field decomposition took place. This increased uncertainty is likely because of the change in spatial sampling; the data used for full-field decomposition was taken along the -90° propagation path, which will result in the smallest spatial-sampling step size equal to the cell dimension ε. An illustration of how the selected propagation angle influences spatial sampling is shown in Figure 6.12, where it can be seen that, when data are taken at a propagation angle of -45°, spatial-sampling step size is at a maximum.

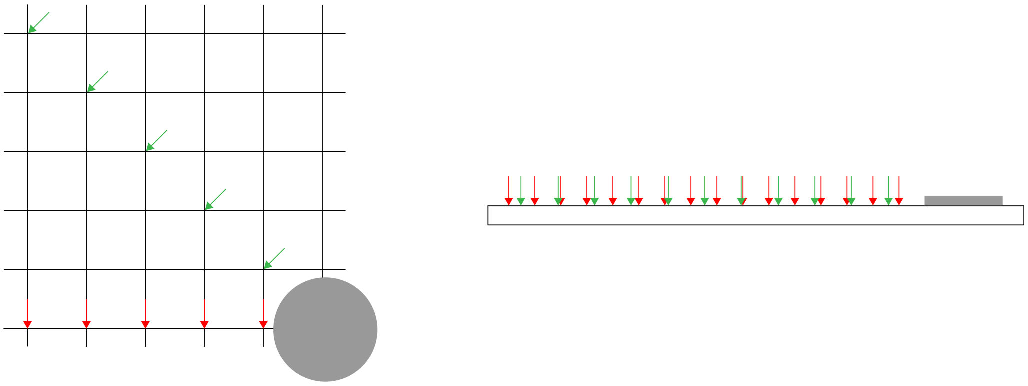

Figure 6.12: Illustration of how propagation angle influences spatial sampling of surface displacement along the propagation path. The grey circle represents the actuator source (not to scale). The left figure shows, with red arrows, the location in the LISA simulation of consecutive points at -90° from the actuation source and in green arrows consecutive points at -45°. The right figure compares the sampling pattern of the consecutive points at different angles.

Figure 6.13 shows an example of the nominal-dictionary wave $\phi(x)$, used to decompose the measured signal at a propagation distance and angle of 50mm and -45° respectively. The phase misalignment between the dictionary and measured nominal waves can be seen, which causes the increased predicted variance and decreased likelihood, when compared to the same propagation distance at -90°. By knowledge of simple geometry and analysis of the grid orientation in Figure 6.12, a propagation angle of -45° will offer the 'worst case scenario' in spatial-sampling misalignment. Even at a maximum spatial-sampling misalignment, the probabilistic decomposition works well to determine the predicted nominal waves, as shown in Figure 6.14(b).

Results of the decomposition of signals containing reflected waves, at different propagation angles, are shown in Figure 6.14, including their predicted variance. It appears in Figure 6.14(a) that the signal taken at a location collinear with the actuator and damage contains a reflection signal of larger amplitude. Although both

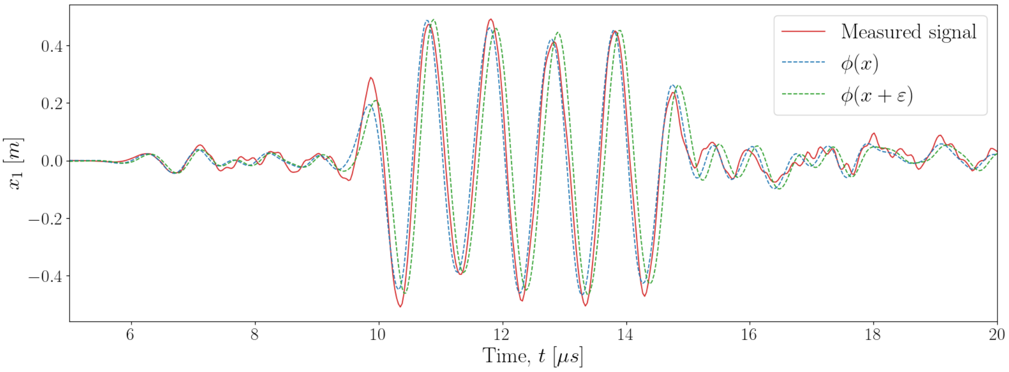

Figure 6.13: Comparison of the measured signal at a propagation distance and angle of 50mm and 45° respectively, and the dictionary wave $\phi(x)$ used for decomposition at this point. In addition, the dictionary wave at one distance point further $\phi(x+\varepsilon)$ is shown.

signals contain reflected waves, and those in the signal taken at -90° appear stronger, there is a larger predicted variance for the signal taken at -45°.

In Figure 6.14(b), the reflection because of damage can be seen at approximately $36 \leq t \leq 43 \mu s$, and is clearly separable from the predicted nominal-wave signal. There also appears to be a small phase difference between the measured signal and predicted nominal signals for each mode. This effect is a result of the dictionary-measured wave misalignment as shown in Figure 6.13. At a similar distance, the measured and predicted nominal waves appear to be a similar shape and amplitude, with the onset and amplitude of the reflected wave being the key difference.

The initial step of the *in-situ* stages of the methodology shown here is the decomposition of the single-source signal to obtain information of reflected-wave signals. The decomposition strategy employed here works well, and appears to provide the reflection signal needed for accurate localisation. Table 6.2 and Figure 6.14 demonstrated that there is increased uncertainty when decomposing signals at propagation distances different to those used for the initial full-field decomposition. As these are waves of short wavelength, small differences in propagation distance can result in significant phase differences between the nominal modes because of their dispersive characteristics. In this case, this spatial-sampling misalignment did not result in

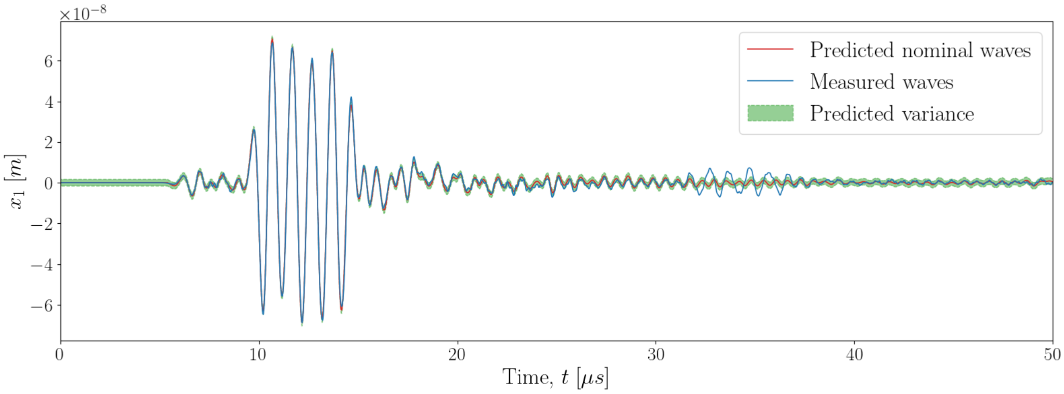

(a)

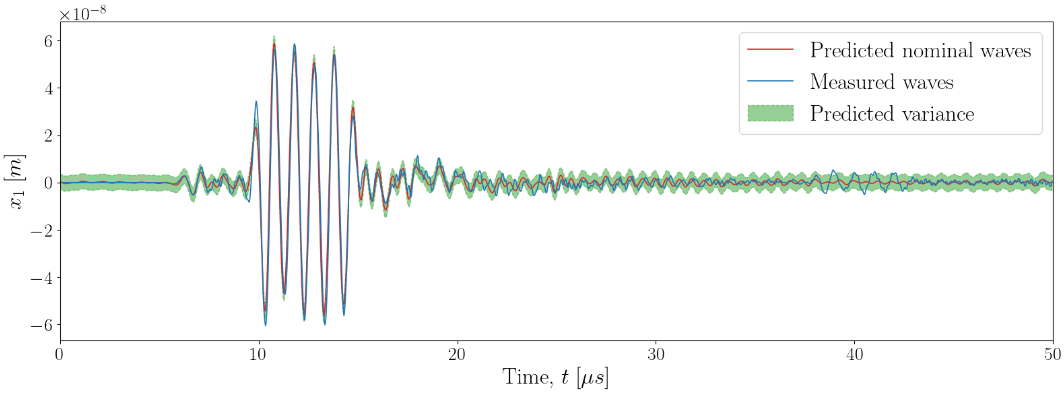

(b)

Figure 6.14: Results from the single-source decomposition applied to signals at a propagation distance of 50mm and propagation angles of: (a) -90° and (b)-45°. The blue line shows the measured signal, the red line shows the predicted nominal waves and the green boundaries show the expected variance.

a phase difference large enough to produce an overly-large predicted variance. As will be shown in Section 6.3.2, the dictionary misalignment did not strongly affect the localisation accuracy. In all cases, but particularly where spatial sampling is limited, or noise in the signal is comparatively larger – such as with SLDV methods – it is important to consider the wavelength with respect to the spatial-sampling step size. Subject to further work, the ability to capture the predicted variance of the nominal signals is a key characteristic of this method, as this can be used to better determine any ‘outlying’ signals, by only taking the difference when the measured signal exceeds the expected variance. Overall, the probabilistic approach works well to decompose the signal into selected modes, doing well to determine the nominal modes and predicted variance. The parameters resulting from the method follow what would be expected from the physics, showing that the method can also produce ready-to-use features that are individual to each mode.

6.3 Localisation

6.3.1 One-dimensional localisation

For illustrative purposes, and to assess the effect of the onset detection stage on the overall methodology, a one-dimensional localisation strategy along the propagation path containing the damage is shown here. An example of the signal-processing steps applied from a single source can be seen in Figure 6.15, showing the decomposed signal, reflected signal and onset determined for the incident A_0 mode and reflected A_0 mode. For both the incident and reflected waves, the onset is determined by the AIC method, and for the reflection, only the portion of the signal after the incident-wave arrival is used. The residual signal clearly shows the reflection signal, which is much stronger than noise present during the period in the signal containing the nominal waves. During the portion of the residual signal in which the nominal waves arrive, there is still some structure as a result of errors between the predicted signal and measured signal. As this structure would likely cause a drop in the calculated ratio of information, the AIC (equation (6.10)) is calculated for the residual signal beginning from the onset of the slowest incident wave, which is in this case the A_0 mode. By inspection of the simulation results in Figure 6.2(a) and the residual signal in Figure 6.15, it can be seen that the reflection signal observed is that of the reflected A_0 mode, as the S_0 mode reflection is of too little amplitude in comparison to the noise floor.

The detected onsets align well with the incident and reflected waves seen in the signals. There is also a drop in the value of the AIC at the end of the reflected wave, indicating a disparity in the entropy level before and after this point. The author

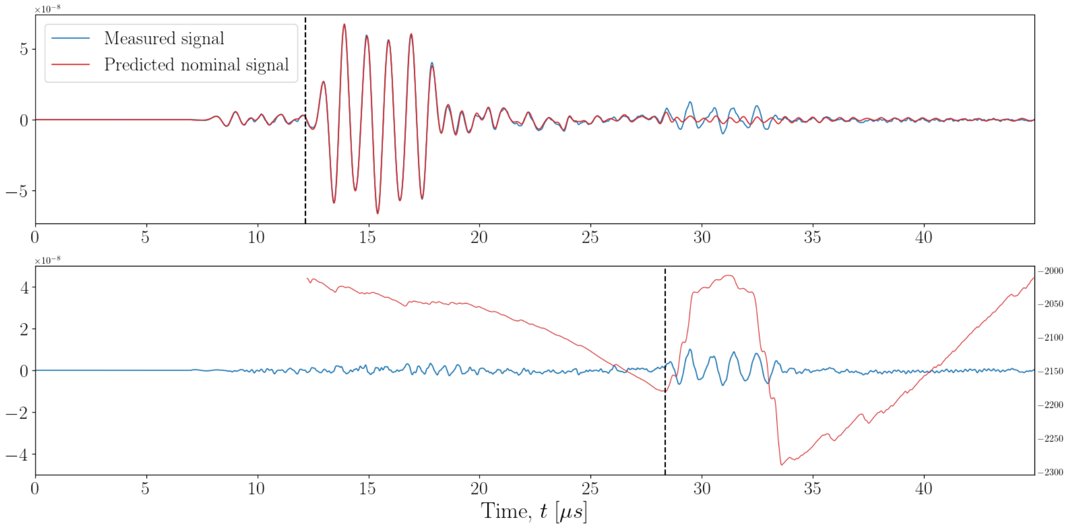

Figure 6.15: Results of the reflection onset-detection stage of signal processing. The upper graph shows the measured and predicted nominal signals, and the lower graph shows the residual signal in blue and the AIC value in red, with the detected onset indicated by the black dashed line. The signal shown is for a propagation distance of 55mm at an angle of -90°.

theorises that this is likely to be because there are no strong waves appearing in the signal after this point, therefore the signal will be of lower structure than the structured reflection signal.

The one-dimensional localisation technique outlined in Section 6.1.5 was applied to signals at various distances along the propagation path. Results of the estimated reflection source difference are shown in Table 6.3, as well as their error with respect to the true value. There does not appear to be a correlation between distance between the reflection source and sensing signal location, as the error values sharply increase between 10 and 20 mm but proceed to increase slightly at increased distances.

6.3.2 Two-dimensional localisation

By using the method outlined in Section 6.1.5, an estimated location of the damage on the surface of the plate was calculated for various sensor groups. The results of these predictions are shown in Table 6.4, where the error is calculated as the

Signal source $\{x, y\}$	True Distance	Estimated Distance	Error	% Error
$\{-65, 0\}$	10.0 mm	9.9 mm	0.1 mm	0.90%
$\{-55, 0\}$	20.0 mm	20.7 mm	0.7 mm	3.64%
$\{-45, 0\}$	30.0 mm	30.8 mm	0.8 mm	2.76%
$\{-35, 0\}$	40.0 mm	41.0 mm	1.0 mm	2.44%

Table 6.3: Results of damage location estimation along propagation path containing the damage, showing the true distance and estimated distance of the location of the signal and the damage.

Euclidean distance between the estimated $\hat{E}$ and true location of damage. As the reflected wave that is present in the signal is the A_0 mode, because of its larger energy than the S_0 mode, the group velocity of the A_0 mode was used for triangulation. From DISPERSE [117], a group velocity for the A_0 wave at 1MHz was calculated to be 3071 m/s. The predicted variance of the decomposed nominal waves is also shown in Table 6.4, and there do not appear to be any significant differences in this variance between sensors. Sensor groups with larger error do not appear to contain significantly-larger predicted variances than groups with low prediction error; indicating that any inaccuracies are not a result of the decomposition. Furthermore, all the predicted variances are greater than those for the decomposed waves in an undamaged plate (Figure 6.11(a)). As the predicted variances are all low in comparison to the signal amplitude, there is confidence in the predicted nominal signal matching the nominal waves. This confidence is extended to the confidence of the residual signal containing only reflected/scattered waves.

A visual representation of predicted locations for the sensor groups with the smallest error is shown in Figure 6.16. These figures show how accurate the predicted locations were in regards to the whole plate. It appears that relative orientation and distance of the sensors from the damage do not influence the accuracy of the method. As there appears to be no trend relating inaccuracy to sensor positions, some insight will be offered here into the results of the two most inaccurate sensor groups (3 and 5).

Figure 6.17(a) shows the predicted location from the sensor group with the largest

Group No.	Sensors			Signal Variance ($\times 10^9$)			Predicted Damage Location	
	S_1	S_2	S_3	σ_1^2	σ_2^2	σ_3^2	$\hat{E} = \{x, y\}$	Error (mm)
1	A	B	C	1.745	3.252	2.656	{-76.0, 0.00}	1.04
2	B	C	D	3.252	2.656	3.095	{-75.3, 0.35}	0.43
3	C	D	E	2.656	3.095	2.614	{-58.0, 3.00}	**17.30**
4	A	C	F	1.745	2.656	3.980	{-76.0, 0.00}	1.04
5	B	D	G	3.252	3.095	2.138	{-68.0, -0.92}	**7.00**
6	C	D	H	2.656	3.095	3.981	{-75.7, 0.32}	0.77

Table 6.4: Table of estimated locations for various sensor pairings, and the error defined as the Euclidean distance between estimated and true location. The predicted variance of the decomposed signal is also shown for each sensor used. The two sensor groups with particularly high errors (3 & 5) are highlighted in bold.

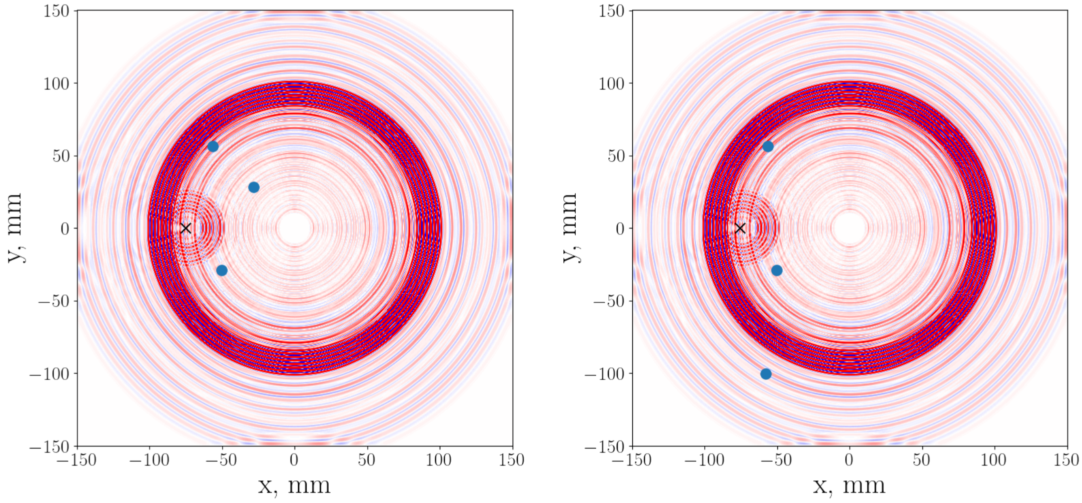

(a) (b)

Figure 6.16: Simulation of damaged plate at 35µs, the black cross shows the predicted location of damage for: (a) sensor group 2 and (b) sensor group 6. The blue circles indicate the locations of the sensors.

error. Sensor group 3 includes sensor E, which is a large distance from the damage source. However, there appear to be several reflected waves within the signal, and it is difficult to know which of these additional waves is reflected from the damage. The surface displacement at the time of the detected reflection onset for sensor E is shown in Figure 6.17(b). The detected onset appears to be the time of arrival of the S_0 wave reflected from the boundary, as this sensor is at 45° to the fibre direction, the boundary reflections from the upper and right sides of the plate arrive simultaneously. These boundary reflections arrive before the damage reflections, so it is difficult to determine the correct onset without significant prior knowledge. For structures of larger size with respect to the distance between sensor and damage, boundary reflections would not be as much of an issue in determining the correct reflection onset, as boundary reflections would arrive at the sensor later in time than reflections from damage.

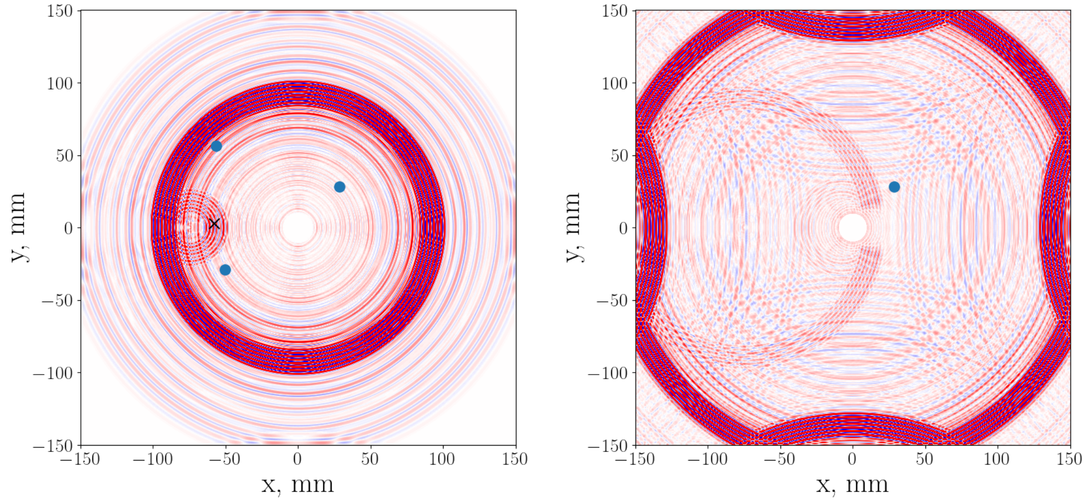

(a)

(b)

Figure 6.17: (a) Predicated location of damage from sensor group 3, superimposed on the surface displacement at 35µs and (b) surface displacement at 51.34µs, the reflection onset determined at Sensor E; the sensor location is indicated by the blue circle.

The predicted location from the sensor group with second-largest error is shown in Figure 6.18(a), as well as the reflection onset detected from the measured signal. As Sensor G is not in any of the groups that predicted the location with lower error, it is useful to look at the surface displacement at the time of reflection arrival at this sensor; this is shown in Figure 6.18(b). At this time point, there does not appear to be any other reflections arriving at the sensor; in fact, the damage reflection does appear to be arriving at this time. However, from visual inspection of Figure 6.18(b), it appears that the true arrival time of the damage reflection was earlier. The inaccuracy in the onset detection – much like with sensor group 3 – may be explained by the large number of incident/and reflected waves that are in the signal at the same time as the damage reflection.

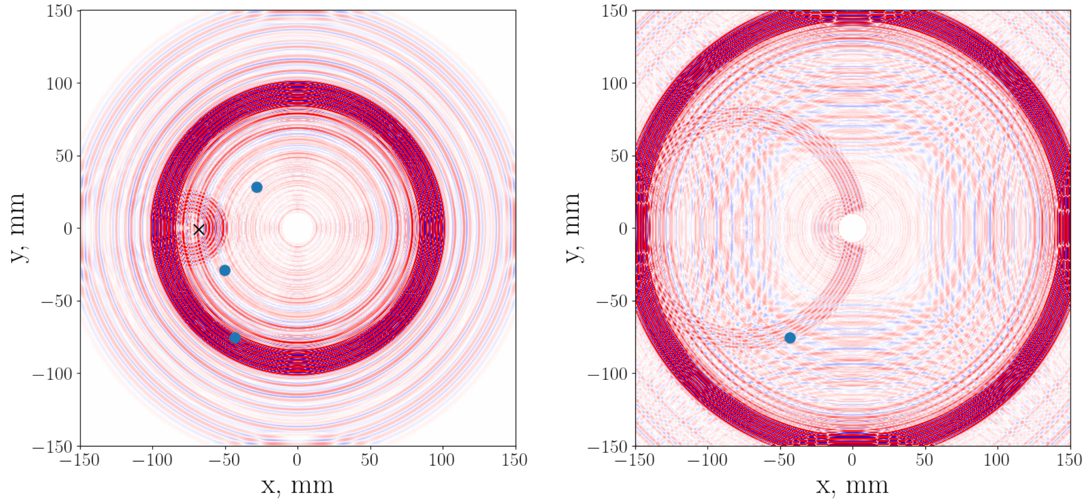

(a) (b)

Figure 6.18: (a) Predicated location of damage from sensor group 5, superimposed on the surface displacement at 35µs and (b) surface displacement at 47.48µs, the reflection onset determined at Sensor G; the sensor location is indicated by the blue circle.

6.4 Discussion

The localisation strategy demonstrated here shows strong capability, often locating damage accurately to within 1mm. By using a variety of sensor placements and groups to triangulate, it appears that sensor-group orientation does not influence accuracy of location. Errors in localisation from sensor placement is a result of the influence of boundary reflections. This independence is expected, as the plate was modelled with a homogeneous material and accurate wave speeds. This result can also be attributed to the quality of the decomposition remaining high at different propagation angles, as shown in Section 6.2.2.

The probabilistic decomposition method shown here contributes well to a damage detection strategy, as the returned parameters can be used to assess the deconstructed signal. The following is, in the authors opinion, one of the most important outcomes of the work shown in this chapter. All the single-source signals were decomposed with a reasonable level of confidence, shown by the relatively low σ^2 parameter. The ability to assess the confidence in nominal-wave decomposition is particularly important for multi-regime strategies; i.e. using SLDV data for the NWD and PZT sensors for single-source.

The strongest influence on inaccurate predicted location of damage was from reflections of the incident waves from the plate boundary and actuator. The plate simulated here was relatively small (limited by computational resources), which is useful in order to determine dispersion curves, as reflection signals are necessary to capture this information. However, for the purposes of damage detection, this size plate is not likely to be inspected and so the influence of boundary reflections may be minimal. In situations where reflections not caused by damage are expected, such as complex geometries or fasteners, models could be implemented utilising knowledge of initial wave propagation and reflection characteristics to increase the fidelity of the nominal-wave dictionary to include expected reflections.

An advantage of the method shown in this chapter is the applicability to more complex materials and structures, because its only prerequisite information is surface displacement data along the propagation path, rather than an accurate analytical model of the waveforms. The Bayesian approach to decomposition is another benefit, as it determines a distribution of predicted models rather than just the best fit. This uncertainty can be utilised to assess the predicted signal, and therefore confidence in the residual signal containing only reflected waves. Furthermore, the method is efficient in terms of computation, memory and storage, and can be used with low-cost sensors.

6.5 Chapter Summary

This chapter demonstrated a methodology for localisation of damage using ultrasonic guided waves by simulating Lamb waves in an aluminium plate. The overall strategy involves decomposing measured single-source signals, from which residual signals can be determined which contain reflected waves, which are then used to triangulate the reflection source. The decomposition stage uses a Bayesian approach in order to generate a distribution of possible nominal waves, allowing better determination of uncertainty. In particular, the full-field decomposition strategy has potential for use in systems where accurate physical models of signals are difficult to obtain. In this chapter, the accuracy of the decomposition and localisation methods have been shown. Inaccurate location was found to be largely because of the influence of boundary reflections, which is not likely to be an issue in application as the plate shown here was of small size. Discussion has been made here of the importance of prior knowledge on the localisation strategy, and how to improve the methodology if this information was not known.

7

A BAYESIAN APPROACH TO GUIDED-WAVE SYSTEM IDENTIFICATION

The localisation strategy shown in Chapter 6 requires prerequisite knowledge of the group velocity, which for given material properties can be determined by generating dispersion curves via solution of the governing equations (see Sections 3.3 and 3.5). A problem is presented where the properties governing the dispersion characteristics are not known; this can be a lack of system information, or where angle-dependent material properties are more difficult to calculate. For this case, a system identification procedure can be used to determine these properties. In addition to determining the predicted values of these properties, it is useful to retrieve the distribution of these parameters. In this chapter, experimentally-measured Lamb-wave data are used to recover the posterior distribution of the system properties which govern the dispersion curves.

Using known points on the dispersion curve, a maximum-likelihood estimate approach can be formulated, optimisation over the maximum of which returns the most likely parameters given point data [139]. However, as stated before, the distribution of the parameters – based on the points on the curve – is also useful to obtain. One way to do this is by using an iterative Markov-Chain Monte Carlo sampling procedure [140], which uses a probability assessment to generate samples from the posterior distribution of the parameters. For an isotropic material, the governing equations are computationally inexpensive to solve, so sampling procedures are viable. However, for complex materials – such as fibre-composites – the wave velocities/wavenumber are dependent on the propagation angle and have a more complex relationship with the central frequency.

Previously, an iterative sampling procedure would not have been practical for anisotropic materials because of the large computational cost. However, the Legendre-polynomial expansion solution outlined in Section 3.5 has a much decreased computational complexity.

The Legendre polynomial expansion approach has previously been shown to decrease cost using a symbolic programming approach [81]; however, as the equations form expansions of polynomials, the procedure has been adapted here to develop a programmatic method of solving the dispersion curves. This adaptation has allowed the computational cost to be reduced, providing a viable method for an MCMC system identification approach.

In this chapter, a scanning-laser Doppler vibrometer is used to record the propagation of Lamb waves in a glass-fibre-reinforced-polymer (GFRP) coupon which was manufactured using the same process as that in a wind turbine blade. Dispersion-curve image data were then calculated for various propagation angles. These dispersion curves are then fed into the MCMC system-identification procedure outlined in Section 7.2, to provide a Bayesian approach to determining system properties of Lamb-wave propagation at various angles in the plate. The distribution of these parameters at each angle is then discussed, including the inferred confidence in the predicted parameters.

As stated in Chapter 1, a WTB is an example of a fibre-composite structure which could benefit from a monitoring system. Therefore, the industry partner Siemens Gamesa Renewable Energy provided the coupon used here to test the tools developed and provide insight into UGW behaviour in a plate which is representative of the behaviour in the real structure. The experiment was then repeated on a carbon-fibre-reinforced-polymer (CFRP) weave plate, the same as used in Chapter 5.

The overall workflow of the methodology is as follows:

i Extract signal data along propagation path in direction from the source.

ii Pass propagation data through two-dimensional Fourier transform to retrieve the dispersion curve image data.

iii Use ridge-picking algorithm outlined in Section 6.1.3 to determine points along dispersion curve.

iv Sample over the posterior distribution of the parameters using a probabilistic simulation of the parameters.

v Return the mean of these distribution as the estimate of the parameters.

7.1 Influence of Material Properties

In this work, the method to solve dispersion-curve equations is that shown in Section 3.5, which for the antisymmetric and symmetric modes are governed by five parameters; four components of the stiffness tensor $(C_{11}, C_{13} = C_{31}, C_{33}, C_{55})$ and the density ρ. It is useful to explore the effect each of these parameters has on the shape and values of the dispersion-curve solutions.

Figure 7.1 shows the results of the dispersion curves calculated for the fundamental Lamb-wave modes of an orthotropic plate, along with the results after a change of ± 30% for each of the elastic constants which define the curves. It is clear that the parameters have varying levels and directions of effects on the curves, as well as the frequency range. Changes in all elastic constants appear to result in a consistently stronger change in the solutions for the S_0 mode.

An interesting point to note, is that changes in C_{13} and C_{33} appear to only affect the S_0 mode, and that the curves are relatively insensitive to changes in C_{13}. Adding further, changes in C_{11} appear to have a stronger effect on the S_0 curve than that of the A_0. For the S_0 curve, there is an obvious 'elbow' at ~10 Mrad/s, the sharpness of

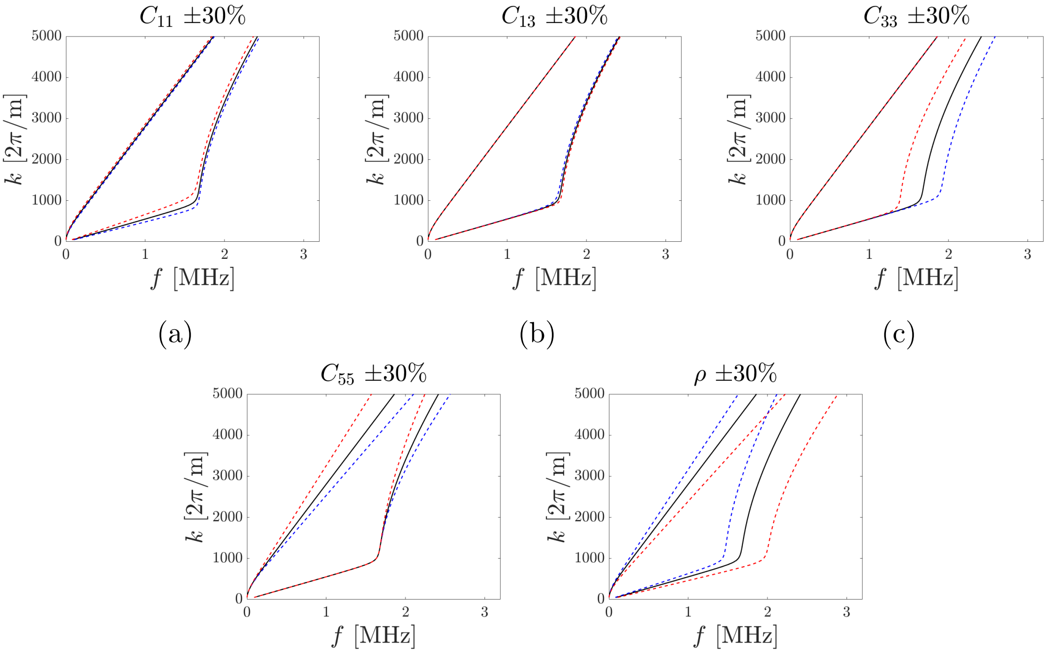

(a) (b) (c)

(d) (e)

Figure 7.1: Sensitivity analysis of material constants on dispersion curves of fundamental Lamb wave modes, for plate thickness of 1mm, and parameters (a) C_{11}, (b) C_{13}, (c) C_{33}, (d) C_{55}, and (e) ρ. With initial values $C_{11} = 160$GPa, $C_{13} = 6.5$GPa, $C_{33} = 14$GPa, $C_{55} = 7$GPA, and $\rho = 1200$kgm^{-3}. For all figures, the black line shows the solution with initial values, the blue line shows the solution with a change of +30% and the red line a change of -30%.

which is unique to more complex models and does not appear in isotropic dispersion curves. Changes in the parameters C_{33} and C_{55} appear to only have an effect on this curve *after* this elbow. For C_{55} and ρ, changes appear to be stronger at higher frequencies, whereas the changes appear more consistent across the frequency range for C_{11}, C_{13} and C_{33}.

7.2 System-Identification Procedure

This section outlines the methodology used for the Bayesian approach to material identification using dispersion curves. It begins by detailing how measured data on the dispersion curves were collected, then follows with a two-part explanation of how to estimate the material properties using these data. This explanation begins by introducing the idea of a maximum-likelihood estimate of the parameters, which is followed by an expansion of this to determining the posterior distribution of parameters.

7.2.1 Measuring dispersion curve observations

The first stage of the process here is to determine a set of measured values on the dispersion curve $\{\hat{\omega}, \hat{k}\}$, of the plate in question. Experimentally, this can be obtained by the use of a two-dimensional Fourier transform (2DFT) [118]. The surface displacement of a wave is measured at regularly-spaced intervals to form time-distance [t-x] data. The signals at each spatial location are then normalised and the matrix passed through a 2DFT to retrieve the frequency-wavenumber [ω-k] data. For the thin-plate coupon used here, Lamb-wave propagation data were measured for various angles for each plate.

7.2.2 Experimental Setup

For the wind-turbine blade coupon data, a similar experimental setup to Chapter 5 was used. The coupon in question is a unidirectional glass-fibre-reinforced polymer plate, which was constructed purposefully using the same stacking sequence as that which is in the blade. Lamb waves were actuated in the GFRP plate by excitation of a 20mm diameter piezo-electric stack actuator (Physik Instrumente P-016.20P) on the surface of the plate, as shown in Figure 7.2. The excitation signal used here was a chirp of length 1ms and upper frequency of 500kHz, allowing for broadband excitation. The out-of-plane surface displacement was measured at 0° and 90°, where 0° represents that in the direction of the fibres. Specific details of the experiment are shown in Table 7.1.

Plate dimensions	800 mm × 700 mm × 16 mm
PZT Location	400 mm × 235 mm
Signal record length	8ms
Sampling frequency	1.024MHz

Table 7.1: Details of experimental setup used to acquire Lamb-wave signal data on the GFRP blade coupon.

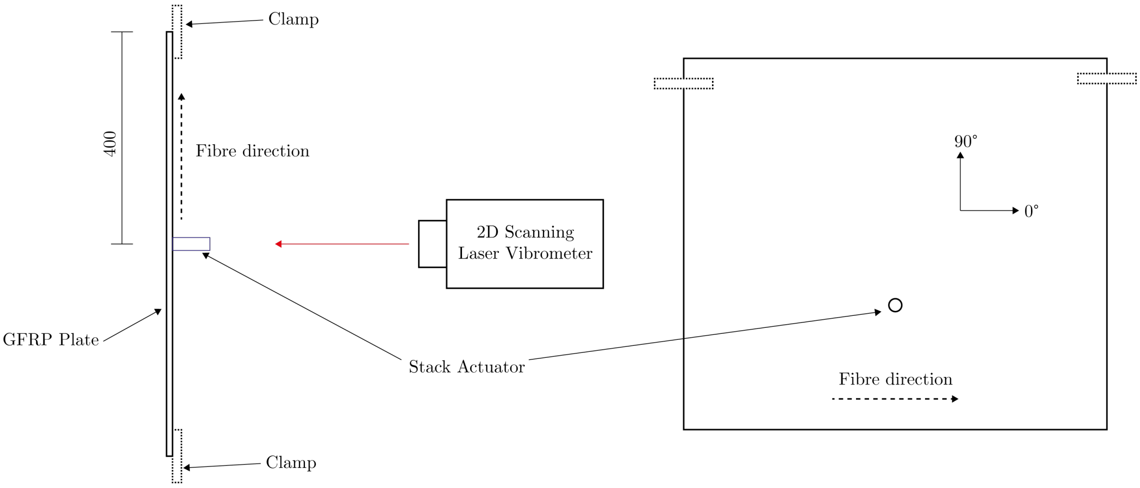

Figure 7.2: Diagram of the experimental setup and location of stack actuator on the 800 mm × 700 mm GFRP plate. The left diagram shows a top-down view, and the right a front view. The orientation of the fibres and the coordinate system used for naming conventions is also shown.

7.2.3 Maximum Likelihood Estimate

First, let one introduce the concept of a system-identification procedure to estimate a set of parameters given a set of n observations,

$$\mathbf{y} = \{y_1, y_2, ..., y_n\} \tag{7.1}$$

Here, the likelihood is defined from the maximum likelihood estimate [139], which is a popular and asymptotically-optimal statistical approach to fitting model parameters using data [141]. Assuming the model is of the form,

$$y_i = f(r) = r + \varepsilon_i \tag{7.2}$$

Figure 7.3: Photo of the GFRP plate experiment setup.

where r is the mean at point n, and ε_i is a white Gaussian noise process. The observations are distributed as $y \sim \mathcal{N}(r, \sigma^2)$. The likelihood is then defined as,

$$L(\mathbf{y}|r) = \prod_{i=1}^{n} \frac{1}{\sqrt{2\pi\sigma^2}} \exp\left(-\frac{1}{2}\frac{(y_i - r)^2}{\sigma^2}\right) \tag{7.3}$$

For determining the likelihood of some model, the mean can be replaced with a function of the input dimension $\mathbf{x}$ of the observations, and some parameters Θ,

$$r = f(x_i, \Theta) \tag{7.4}$$

so the likelihood becomes,

$$L(\mathbf{y}|\Theta) = \prod_{i=1}^{n} \frac{1}{\sqrt{2\pi\sigma^2}} \exp\left(-\frac{(y_i - f(x_i, \Theta))^2}{2\sigma^2}\right) \tag{7.5}$$

Now, consider the application of this maximum-likelihood-estimate (MLE) procedure for identifying the material properties using observations from the dispersion curve. In Section 7.2.1, it was noted that there is a much lower relative resolution in the wavenumber dimension of the dispersion image and in the resulting selected points on the curve. This implies that the Gaussian white-noise distribution is mostly in ω; thus, if one were to estimate the likelihood based on a model of $k(\omega, \Theta)$, the function would be of the form,

$$y_i = f(r + \varepsilon_i) \tag{7.6}$$

Therefore, the problem is formulated as one based of a model of $\omega(k, \Theta)$. The observations are taken as the points on the dispersion curve,

$$y_i = \{\hat{\omega}_i, \hat{k}_i\} \tag{7.7}$$

where $\hat{\omega}_i$ and $\hat{k}_i$ are the values of frequency and wavenumber respectively, at point i. Thus, the likelihood is defined as,

$$L(\mathbf{y}|\Theta) = \prod_{i=1}^{n} \frac{1}{\sqrt{2\pi\sigma^2}} \exp\left(-\frac{\left(\hat{\omega}_i - \omega(\hat{k}_i, \Theta)\right)^2}{2\sigma^2}\right) \tag{7.8}$$

In this case, $\omega(\hat{k}_i, \Theta)$ is determined using the methods outlined in Sections 3.3 and 3.5, depending on the material being modelled. For the case of an orthotropic material, the parameters are defined as,

$$\Theta = \{C_{11}, C_{13}, C_{33}, C_{55}, \rho\} \tag{7.9}$$

as $C_{31} = C_{13}$.

The likelihood can be adapted further by separating out the observed and calculated values of ω for each mode; in this case, the definition of the likelihood becomes,

$$L(\mathbf{y}|\Theta) = L(\mathbf{y}_{A_0}|\Theta)L(\mathbf{y}_{S_0}|\Theta) \tag{7.10}$$

where,

$$L(\mathbf{y}_\psi|\Theta) = \prod_{i=1}^{n} \frac{1}{\sqrt{2\pi\sigma^2}} \exp\left(-\frac{\left(\hat{\omega}_{i,\psi} - \omega_\psi(\hat{k}_i, \Theta)\right)^2}{2\sigma^2}\right) \tag{7.11}$$

for wave mode ψ. Maximising $L(\mathbf{y}|\Theta)$ provides an estimate of the most likely material properties; however, it is also possible to retrieve information on their *distribution*.

7.2.4 Estimating the posterior distribution

The objective at this stage is to determine the distribution of the parameters which define the dispersion curve. As the likelihood includes a noise variance term σ^2, the parameter vector is extended to include this, so that,

$$\theta = \{\Theta, \sigma\} = \{C_{11}, C_{13}, C_{33}, C_{55}, \rho, \sigma\} \tag{7.12}$$

The distribution of these parameters can be determined by identifying the posterior probability given a set of measured data, $p(\theta|\mathbf{y})$. However, this is not directly inferable, so a manipulation is done using Bayes rule,

$$p(\theta|\mathbf{y}) = \frac{p(\mathbf{y}|\theta)p(\theta)}{\int p(\mathbf{y}|\theta)p(y)p(\theta)} \tag{7.13}$$

where $p(\mathbf{y}|\theta)$ is calculated using equation (7.8), and $p(\theta)$ is the *prior*, which can be defined using initial knowledge of the parameters. For d parameters, assuming each parameter is independent, the prior is calculated as,

$$p(\theta) = \prod_{i=1}^{d} p(\theta_i) \tag{7.14}$$

Now, the problem is transferred, in that the normalisation term in the denominator is intractable. Instead, a procedure can be used to sample from the posterior with enough repetition that an estimate of the distribution over the parameters can be inferred. One such procedure is the Markov-Chain Monte Carlo (MCMC) method, where subsequent samples depend on assessing their probability with respect to the previous one.

A full outline of the derivation and procedure for MCMC is given in **??**; however, an overview and important characteristics are given here. MCMC is an iterative sampling procedure, where the subsequent samples depend on assessing their probability with respect to the previous one. The aim is to simulate the posterior distributions of the parameters θ, by sampling them based on the probability of the parameters given a set of observations $\mathbf{y}$. At each step, a random walk is made in each direction of θ, then an acceptance ratio is defined as,

$$\hat{\alpha} = \frac{p(\theta'|\mathbf{y})}{p(\theta_k|\mathbf{y})} \tag{7.15}$$

where θ_k is the previous guess and θ' is the current guess of the parameters. If $\hat{\alpha} > 1$, then θ' is accepted, but with the *Metropolis-Hastings* algorithm [142], a uniform random variable is included in order to allow movement to lower probability parameters in order to obtain the full distribution.

There is, however, a similar problem to that above, in that $p(\theta|\mathbf{y})$ is not known. This problem is overcome via a manipulation using Bayes rule, and the acceptance ratio becomes,

$$\hat{\alpha} = \frac{p(\mathbf{y}|\theta')p(\theta')}{p(\mathbf{y}|\theta_k)p(\theta_k)} = \frac{\hat{p}(\theta'|\mathbf{y})}{\hat{p}(\theta_k|\mathbf{y})} \tag{7.16}$$

and so only the likelihood $p(\mathbf{y}|\theta)$ and prior $p(\theta)$ must be defined. In practice, for computational stability, the probabilities are calculated in the log space, so the marginal likelihood becomes,

$$\log(\hat{p}(\theta|\mathbf{y})) = \log(p(\mathbf{y}|\theta)) + \log(p(\theta)) \tag{7.17}$$

where,

$$\log(p(\theta)) = \sum_{i=1}^{d} \log(p(\theta_i)) \tag{7.18}$$

Now, consider how to define this problem for the application to dispersion-curve material identification. The first step is to define the likelihood, which is done using equation (7.8). Which in the log space is,

$$\log(p(\mathbf{y}|\theta)) = -n\log(\sigma) - \frac{n}{2}\log(2\pi) - \frac{1}{2}\sum_{i=1}^{n} \frac{\left(\hat{\omega}_i - \omega(\hat{k}_i, \Theta)\right)^2}{\sigma^2} \tag{7.19}$$

During sampling using MCMC, the size of the random step taken for each parameter is important, as too large a step will cause stall, and too small a step will require a large number of iterations. An improvement is made on the standard MCMC procedure, which incorporates Hamiltonian mechanics, to adapt the step size for an optimal simulation, and is so called Hamiltonian Monte Carlo (HMC) [143, 144]. For this work, the probabilistic programming language Stan [145] was used.

Next, consider the definition of the priors, which can be done using reasonable knowledge of the application. As the prior is a combination of the individual probabilities of each parameter, prior belief on the distribution of these parameters can be used to define each $p(\theta_i)$. In this case, the density of the plate is supplied, but no other material properties were provided. Therefore, a tight prior can be given on ρ and priors on the elastic constants are defined to capture reasonable values for the material. The types and definitions of the priors used here are shown in Table 7.2 and their probability density functions are shown in Figure 7.4.

Parameter	Distribution	Definition	
C_{11}	Gamma(α, β)	$\alpha = 2$	$\beta = 0.02$
C_{13}	Gamma(α, β)	$\alpha = 1.5$	$\beta = 0.05$
C_{33}	Gamma(α, β)	$\alpha = 1.5$	$\beta = 0.05$
C_{55}	Gamma(α, β)	$\alpha = 1.5$	$\beta = 0.025$
ρ	$\mathcal{N}(\mu, \sigma)$	$\mu = 1600$	$\sigma = 300$
σ	Gamma(α, β)	$\alpha = 2$	$\beta = 2 \times 10^{-5}$

Table 7.2: Definitions of priors for parameters in θ.

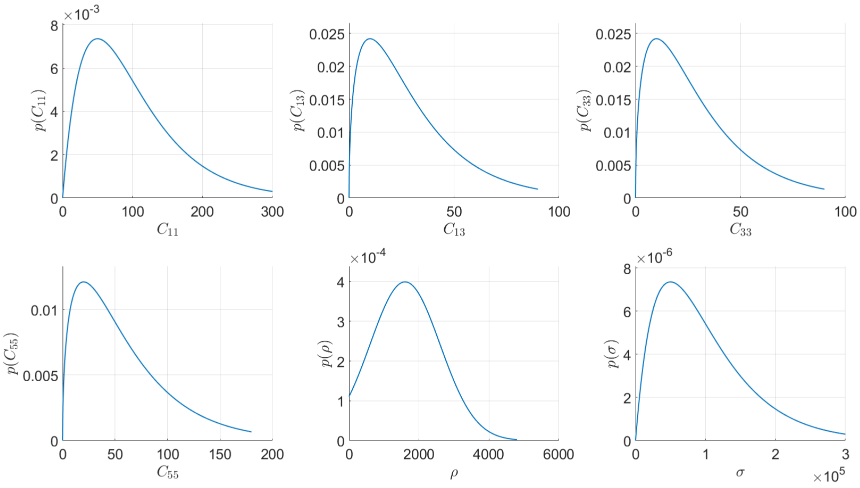

Figure 7.4: Prior distributions of parameters for the MCMC simulation procedures performed.

The calculated prior for each of these distributions is,

$$\mathcal{N}(x|\mu,\sigma) = \frac{1}{\sigma\sqrt{2\pi}} \exp\left(-\frac{(x-\mu)^2}{2\sigma^2}\right) \tag{7.20}$$

$$\text{Gamma}(x|\alpha,\beta) = \frac{\beta^\alpha}{\Gamma(\alpha)} x^{\alpha-1} \exp(-\beta x) \tag{7.21}$$

where x is the value over which the distribution is applied, μ is the mean, σ is the standard deviation, α is the shape parameter, β is the rate parameter, and $\Gamma(x)$ is the Gamma function of x. In the log space, these definitions become,

$$\log(\mathcal{N}(x|\mu,\sigma)) = -\log(\sigma) - \frac{1}{2}\log(2\pi) - \frac{1}{2}\left(\frac{x-\mu}{\sigma}\right)^2 \tag{7.22}$$

$$\log(\text{Gamma}(x|\alpha,\beta)) = \alpha\log(\beta) - \log(\Gamma(\alpha)) + (\alpha-1)\log(x) - \beta x \tag{7.23}$$

7.2.5 Parameter Estimation

After sampling over the parameters using the procedure outlined above, an estimate of the distribution of these parameters is returned. In practice, there is also an initial 'burn-in' period where the chain begins to converge to a stationary distribution. During 'burn-in', the algorithm draws samples from a range not indicative of the posterior distribution, and instead will continually move towards parameter-space locations of higher likelihood. These movements may not always be in the same direction, one will often see during this stage that the sample values will vary greatly and jumpt to either side of the stationary posterior distribution. The portion of values returned during this phase is ignored in the final distribution of each parameter. Taking the iterated values of each parameter, some arithmetic statistical measures can be calculated. Here, the first two statistical moments are calculated; the mean and the standard deviation.

For the purposes of system identification here, the mean of the distribution of each parameter is taken as the estimated value. From these values, the dispersion curves can be calculated, showing the wave-propagation behaviour in the material. By taking the second moment as one standard deviation of each parameter, the confidence interval of the dispersion curve, given each parameter, can be determined.

7.3 Results

In this section, results for the material-identification procedure applied to both coupons are shown. Each subsection will show and discuss the results in the same format; samples from the posterior distributions of the parameters are shown in both univariate and bivariate distributions, as well as a kernel density estimate used to estimate the probability density function of the bivariate distributions. Also shown, are samples of dispersion curves drawn from the samples of the posterior distributions, overlaid onto the observed dispersion-curve image data taken from the two-dimensional Fourier transform. Each subsection is split into further subsections, one for each of the different orientations with respect to the fibres, followed by a subsection showing the arithmetic calculations of the first two statistical moments, for each parameter, for all propagation angles.

7.3.1 Wind turbine blade coupon

The first set of tests was performed on the unidirectional GFRP plate, for which an orthotropic model for the material is applicable. The experimental regime was adapted here to excite both fundamental Lamb wave modes within the wave-packet, and so for this section, the modified multimode likelihood in equation (7.11) is used.

Samples from the posterior

The results of 20,000 accepted samples of the sampling procedure for propagation angles of 0° and 90° are shown in Figures 7.5 and 7.6 respectively. The first observation that can be made is of the much tighter posterior of each of the parameters, thanks to including information on multiple wave modes. In both propagation angles, there is evidence of correlation between material parameters, whereas the distribution of the noise parameter appears to converge to a univariate distribution. This result is anticipated, as the elastic properties which form the stiffness matrix are described by a series of inseparable equations. One observation that can be made, is the strong correlation between certain parameters, such as between C_{11} and C_{13} for a 0° propagation. Another observation in the results is the independence of σ from all

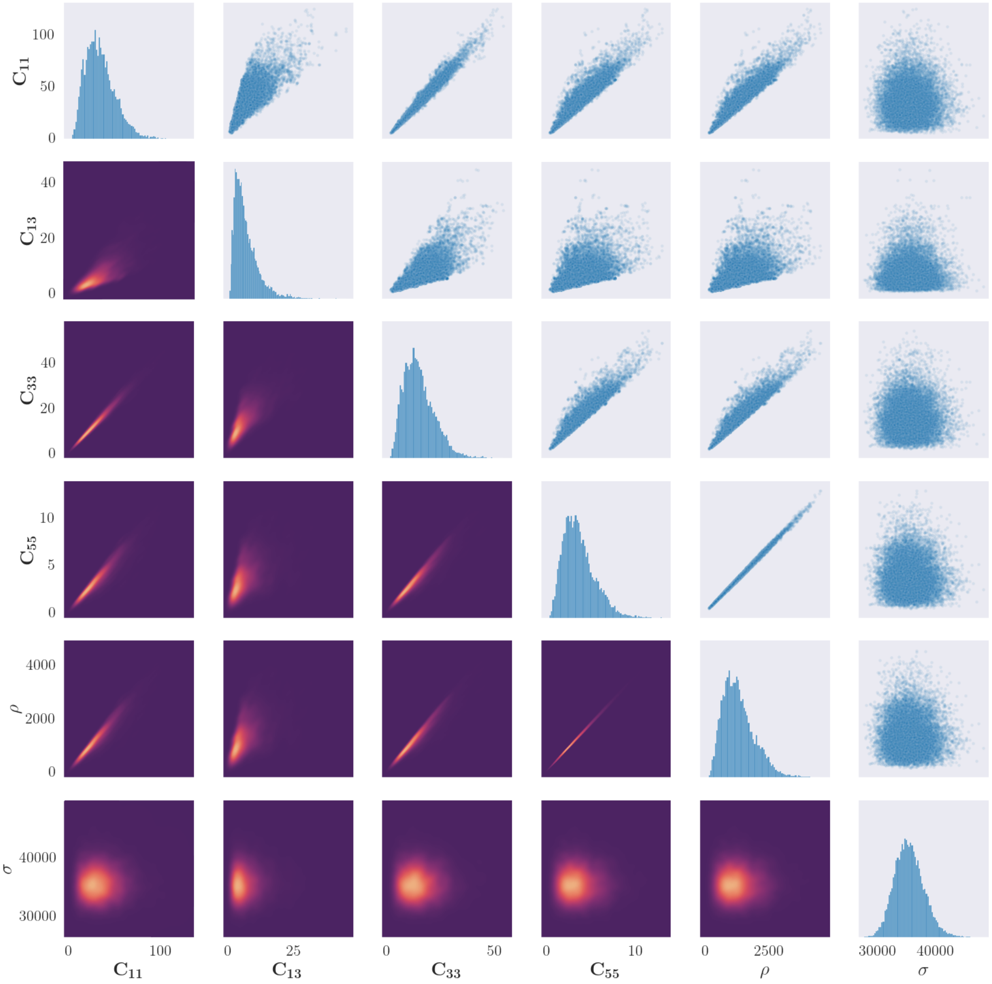

Figure 7.5: Results of the material property identification procedure applied to the blade coupon for the propagation angle of 0°. Figures along the diagonal show the histogram of the samples for each parameter. Figures in the upper-right triangle, show a scatter plot of correlation between two parameters. Figures in the lower-left triangle, show a bivariate kernel density estimate of the cross-correlation between parameters, where lighter colours represent a larger value of the density.

the other parameters, which is intuitive, as this is the noise and has no effect on the shape of the curve.

Figure 7.5 indicates the univariate and bivariate distributions for a propagation angle

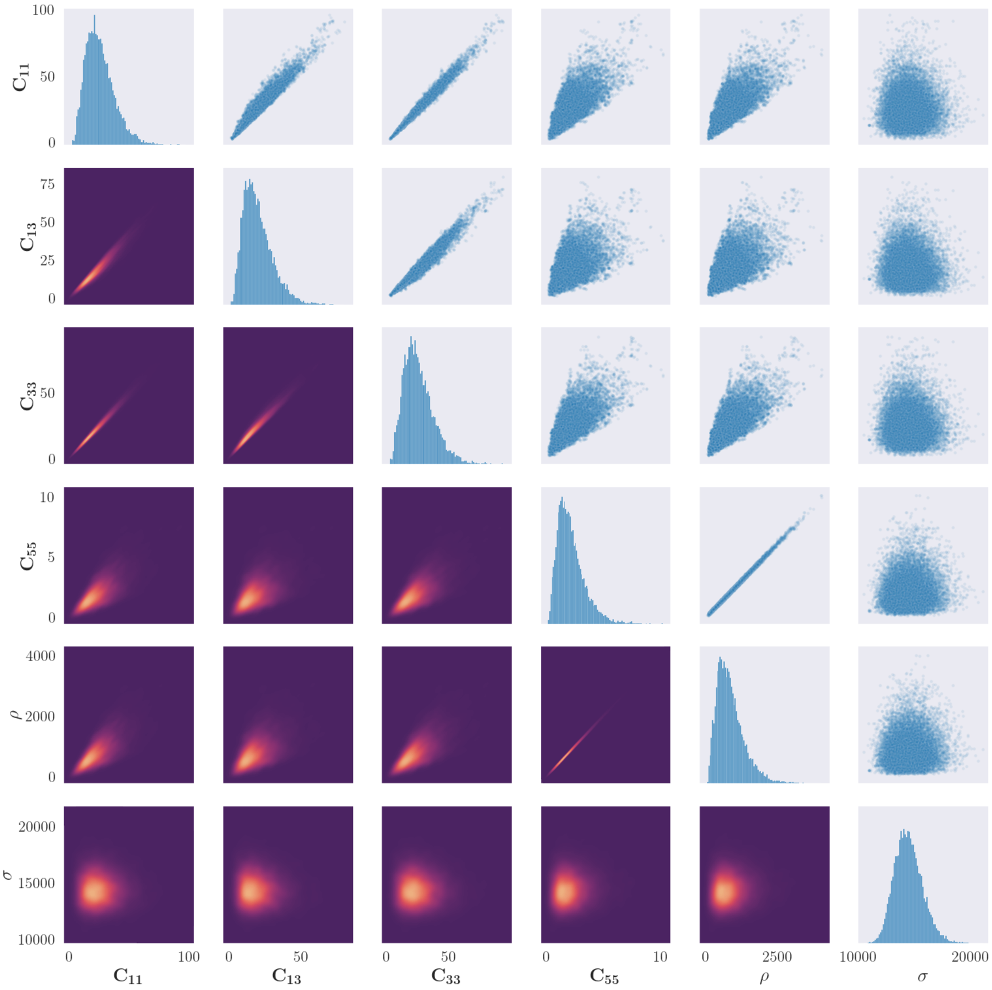

Figure 7.6: Results of the material property identification procedure applied to the blade coupon for the propagation angle of 90°. Figures along the diagonal show the histogram of the samples for each parameter. Figures in the upper-right triangle, show a scatter plot of correlation between two parameters. Figures in the lower-left triangle, show a bivariate kernel density estimate of the cross-correlation between parameters, where lighter colours represent a larger value of the density.

of 0°. Another observation from these plots, is the pronounced 'edge' on the scatter correlation plots; in particular, between C_{13} and all other elastic constants. There is again the hard 'edge' on the bivariate samples; in particular, between C_{13} and all other elastic constants, which is a result of the condition of rejection when $\lambda > 0$. As a condition of the solution to the dispersion curve equations is that $\lambda < 0$, any solutions where this is not the case are rejected. The edge may indicate a region of forbidden parameter combinations which cannot exist given a real elastic material.

There appears to be a strong correlation between C_{55} and ρ, which appears to be a linear relationship. This could be explained by comparison to the isotropic case; in Chapter 3 it was shown that for an isotropic material their relationship can be defined as $C_{55} = \rho c_T^2$. For an orthotropic material, the transverse wave velocity would remain the same when rotating around the axis in the direction of wave propagation. This property could be used to reduce the number of parameters, increasing performance of the simulation.

One observation made in the results of the sample plots for the 90° propagation, in comparison to 0°, is the less apparent hard edge caused by the rejection parameter. This may indicate that the posterior space of valid elastic constants is less discontinuous when modelling Lamb wave propagation through fibres. Another difference between the two sets of results is that there is a less strong correlation in the parameter pairs C_{11}-C_{13} and C_{13}-C_{33}. This could be a result of the fibres no longer acting as a secondary wave guide, and instead shear forces through the fibres have more of an influence on wave propagation.

As stated in the beginning of this chapter, a key advantage of the method shown here is the freedom in the posterior distribution, as no assumption is made as to its shape. In an engineering context, this allows freedom in the material type to be modelled, so long as the model of the dispersion curve solutions is accurate. For both propagation angles here, the univariate distributions of the parameters do not all appear to be of the same shape. In fact, the elastic constants and density appear to converge to a Gamma distribution of varying skewness, and the noise parameter appears to converge to a normal distribution. In comparison to the results of the CFRP plate, instead of the elastic constants converging to either Gaussian or Gamma distributions, all elastic constants converge to Gamma distributions here. As these results use more information and seem to be more reliable, this indicates that the true posterior of the elastic constants should converge to a skewed distribution.

Posterior distribution of dispersion curves

Using the parameters at each sample point, a distribution of the dispersion curves was also produced, and is shown in Figure 7.7, along with observation points taken from the $[\omega\text{-}k]$ image data. For the propagation angle of 0°, the darker areas of the image data, as well as the observation points, lie within the distribution well. This observation shows that the method works well for obtaining dispersion characteristics of Lamb waves.

Although the coupon used here has a unidirectional fibre, an orthotropic model was still used for the data at a propagation angle of 90° to test its applicability to all directions. Figure 7.7(b) indicates that, for determining dispersion curves of the A_0 mode, this model still provides a useful solution. However, the curves generated for the S_0 mode become mismatched from the image data, as well as the points taken from the ridge-picking algorithm, at a frequency-thickness greater than 1.2MHz.

In order to analyse the updated results with respect to the original objective – to determine an accurate model of the group velocity – the distribution of $[\omega\text{-}c_g]$ curve solutions are shown in Figure 7.8. For the propagation angle of 0°, the curves have no discontinuities and appear to have a low uncertainty. However, the curves for the 90° propagation angle have some discontinuities at $1.25 < fh < 1.8$ MHz-mm.

Quantifying the material-property posteriors

For each of the parameters, the expected value and variance are calculated for the samples from the posterior distributions for both angles, the results of which are shown in Table 7.3. There is quite a significant discrepancy in the mean value for density; where for a propagation angle of 90°; it is predicted to be much lower. This result, as well as the discrepancy between the sampled curve solutions and the image data, would indicate that the orthotropic model is not suitable when modelling propagation away from the direction of the fibres.

Relative to the mean values, the standard deviations of each parameter are similar, which aligns well with the observed posterior distributions that can be seen in Figures 7.5 and 7.6. This result can be interpreted as meaning that the level of

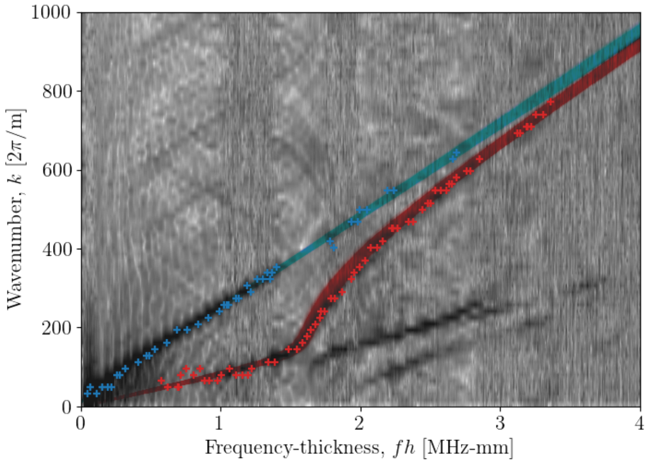

(a)

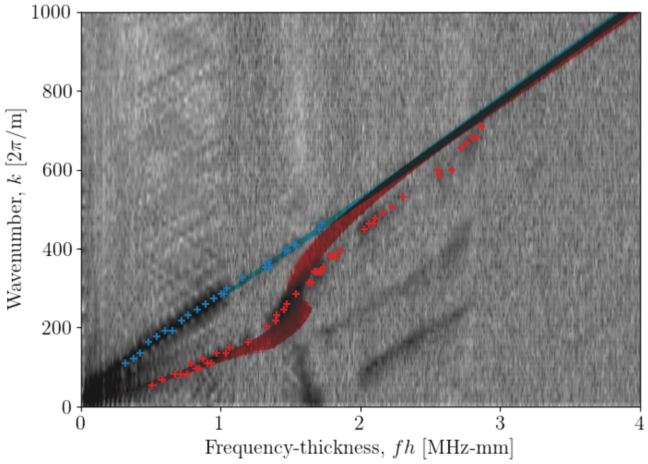

(b)

Figure 7.7: Distribution of generated dispersion curves for each sample taken for propagation angles of: (a) 0° and (b) 90°. The blue curves show the distribution of the A_0 mode and red curves show the distribution of the S_0 mode. The curves are overlaid on the image data taken from the 2DFT and the '+' markers indicate the points taken from the ridge-selection algorithm which were used in the procedure as $\{\hat{\omega}, \hat{k}\}$.

uncertainty is similar for each parameter, meaning that discrepancies are not confined to a single parameter, but instead in the *combination* of parameters. It is important to note that, in the prior, each parameter is treated as independent, whereas the

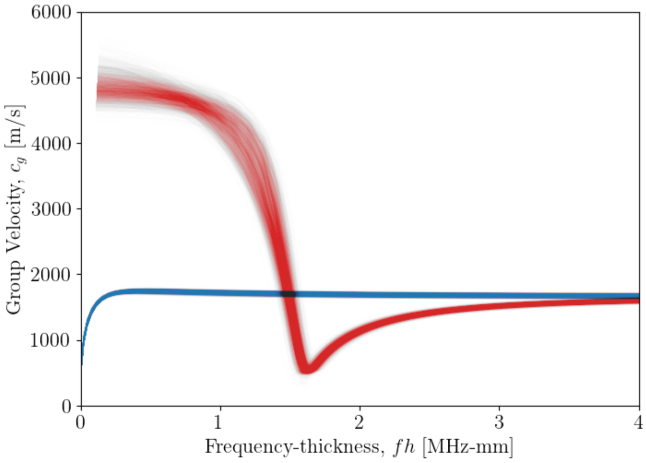

(a)

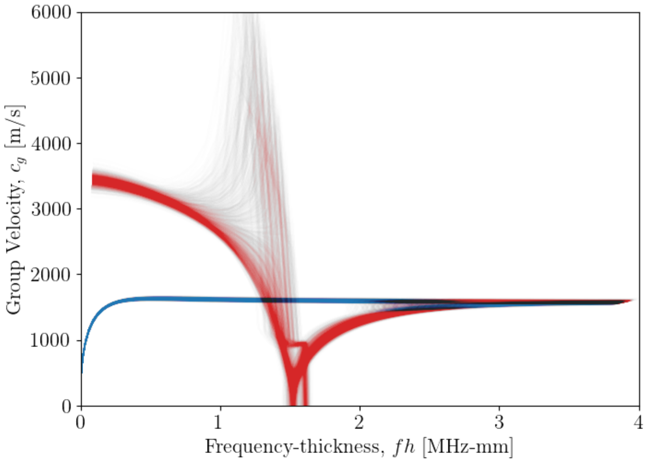

(b)

Figure 7.8: Distribution of calculated $[\omega\text{-}c_g]$ curves for each sample taken for propagation angles of: (a) 0° and (b) 90°. The blue curves show the distribution of the A_0 mode and red curves show the distribution of the S_0 mode.

posterior shows that there is a strongly co-dependent relationship between the parameters and dispersion-curve solutions.

7.3.2 Thin multi-directional fibre-composite plate

From the work above, the method is shown to be return reliable information for accurately determining dispersion curve information – with the caveat that the model

Parameter	0°		90°	
	$\mathbb{E}[\theta]$	$\mathbb{V}[\theta]$	$\mathbb{E}[\theta]$	$\mathbb{V}[\theta]$
C_{11}	34.69	265.9	26.19	150.6
C_{13}	6.917	21.67	20.12	103.3
C_{33}	15.24	51.39	25.874	149.1
C_{55}	3.649	3.052	2.141	1.426
ρ	1,320.9	396,661	874.45	232,668
σ	35,578	6.382e6	14,427	1.576e6

Table 7.3: Expected values (arithmetic mean) and variances calculated from the samples drawn from the posterior for each parameter and various propagation angles on the blade coupon.

used is suitable. In order to test the method on a system where the model is assumed simpler, but not totally unsuitable, it was applied to the CFRP weave plate used in Chapter 5. Due to the nature of the material and the strong attenuation associated with the S_0 mode, only the A_0 mode data were used for this section.

Propagation in the direction of the fibres

The results of 20,000 accepted samples of the sampling procedure for propagation angles of 0° and 90° are shown in Figures 7.9 and 7.10 respectively. Much like the results of the sampling for the GFRP plate, there is evidence of correlation between parameters. However, as a result of including only the A_0 mode in the procedure, the results are different. For 0°, there appears to be a strong correlation between C_{33} and both C_{13} and C_{11}, as well as a very strong correlation between the values of C_{55} and ρ. There is again the hard 'edge' on the bivariate samples; in particular, between C_{11} and C_{33} with both C_{55} and ρ.

In comparison to the results for the 0° propagation angle, there are some notable differences in the posterior distributions for the propagation angle of 90°. Firstly, the distribution of C_{11} converges to a lower expected value and C_{55} converges to a higher value – indicating that the elastic constants are lower and higher respectively. This

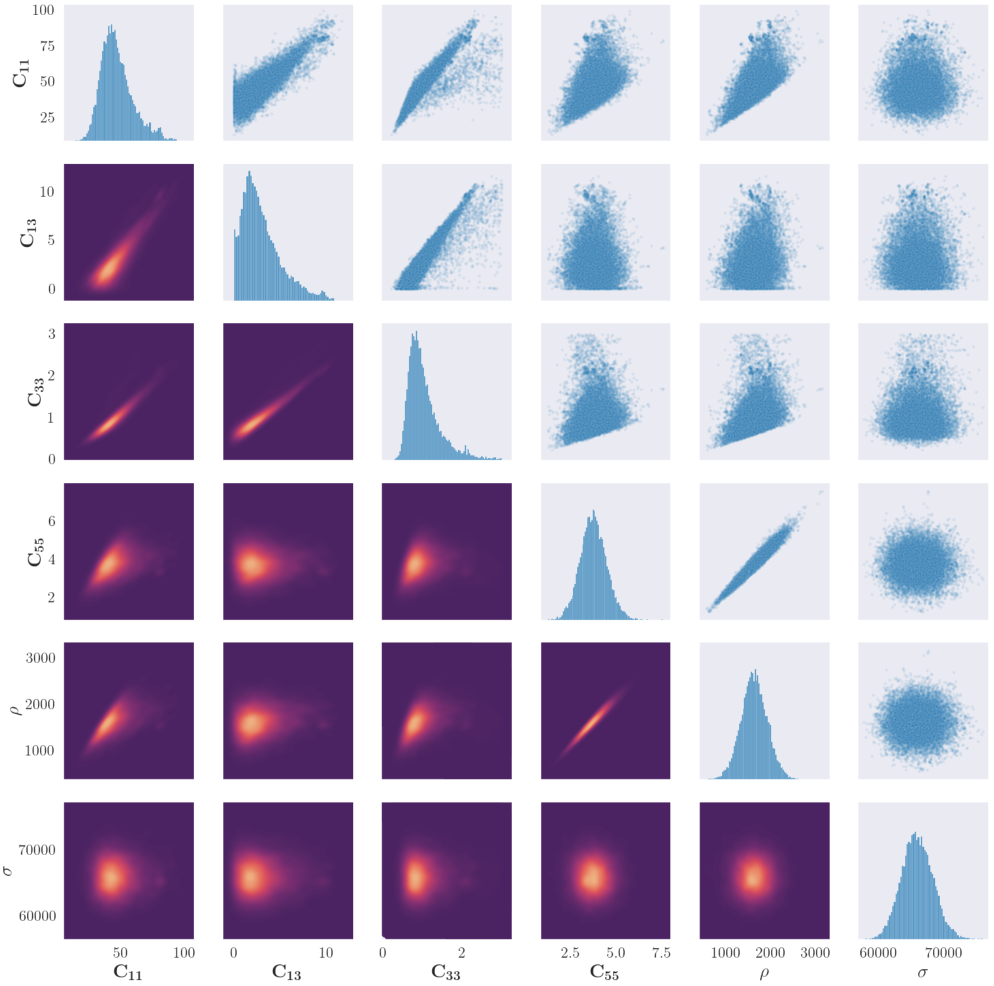

Figure 7.9: Results of the material property identification procedure for the propagation angle of 0°. Figures along the diagonal show the histogram of the samples for each parameter. Figures in the upper-right triangle, show a scatter plot of correlation between two parameters. Figures in the lower-left triangle, show a bivariate kernel density estimate of the cross-correlation between parameters, where lighter colours represent a larger value of the density.

observation indicates that, even with the carbon-fibre weave material, the energy of the antisymmetric mode is dominated by a particular fibre orientation; otherwise, it would be expected that for both fibre orientations, the posteriors would remain similar. Furthermore, the correlation between C_{55} and ρ appears to be weaker than at a propagation angle of 0°, and instead there is a strong correlation between C_{11} and ρ.

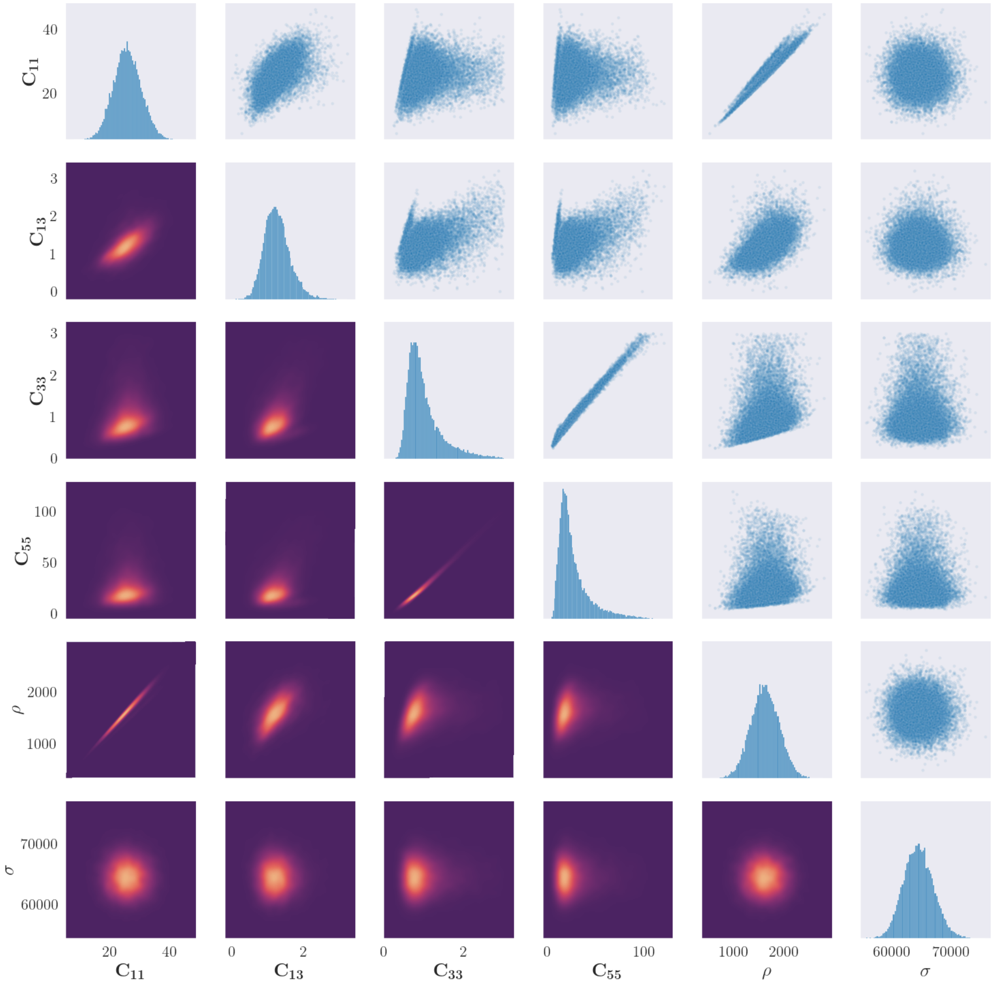

Figure 7.10: Results of the material property identification procedure for the propagation angle of 90°. Figures along the diagonal show the histogram of the samples for each parameter. Figures in the upper-right triangle, show a scatter plot of correlation between two parameters. Figures in the lower-left triangle, show a bivariate kernel density estimate of the cross-correlation between parameters, where lighter colours represent a larger value of the density.

When looking at the univariate posterior distributions, it appears that the shape of these distributions varies between parameters. For example, the posterior for C_{11} appears to converge to a Gaussian distribution, whereas that of C_{33} converges to a Gamma distribution. The skewness of the Gamma distributions also changes between parameters; this shows that it is important to give freedom in the posterior to converge to the true shape.

As with the GFRP plate, using the samples drawn from the posterior, a distribution of dispersion curves was generated, and is shown in Figure 7.11, along with observations taken from the $[\omega\text{-}k]$ image data. An initial observation is of the dissimilarity of the S_0 mode curves and their representation in the image data. In both cases, wavenumber is calculated to be higher for all samples drawn. For dispersion curves of unidirectional fibre-composite materials, the A_0 mode is mostly sensitive to the C_{11}, C_{55} at 0°, and additionally the C_{13} and C_{33} parameters at 90° (Section 7.1). As the distributions are only sampled based on observations of the A_0 mode, it will only be influenced by those parameters to which the curves are sensitive.

For all samples drawn, the model for the dispersion curve of the A_0 mode is very accurate, and the points lie well within the distribution of the curves. An interesting note relates to the additional observation points at $fh > 0.4$MHz-mm for the propagation angle of 0°. These additional points are likely the cause of the tighter distribution of curves for this propagation angle, and are likely to be a result of a clearer dispersion curve on the image data (i.e. more contrast in the image).

In this work, the dispersion curves are solved using an orthotropic model. For the objectives of the work here, the model provides accurate results based on comparison to the image data provided. It is important to note the restriction of the curves to the bandwidth available in the observations.

Propagation Through Fibres

The results of 20,000 accepted samples of the sampling procedure for propagation angles of 45° and 135° are shown in Figures 7.12 and 7.13 respectively. As with the results for propagation along the fibres, in both propagation angles, there is

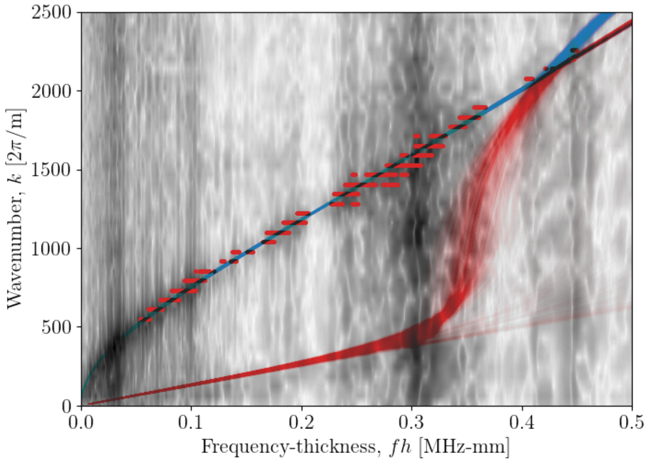

(a)

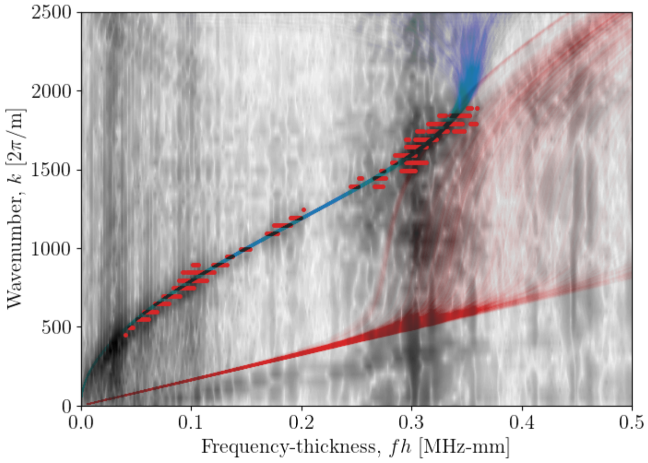

(b)

Figure 7.11: Distribution of generated dispersion curves for each sample taken for propagation angles of: (a) 0° and (b) 90°. The blue curves show the distribution of the A_0 mode and red curves show the distribution of the S_0 mode. The curves are overlaid on the image data taken from the 2DFT, and the red dots indicate the points taken from the ridge-selection algorithm which were used in the procedure as $\{\hat{\omega}, \hat{k}\}$.

evidence of correlation between material parameters, whereas the noise parameter appears to converge towards an independent univariate distribution. In comparison to the results from the propagation angles along the fibres, there appear to be more material parameter combinations that have a strong correlation.

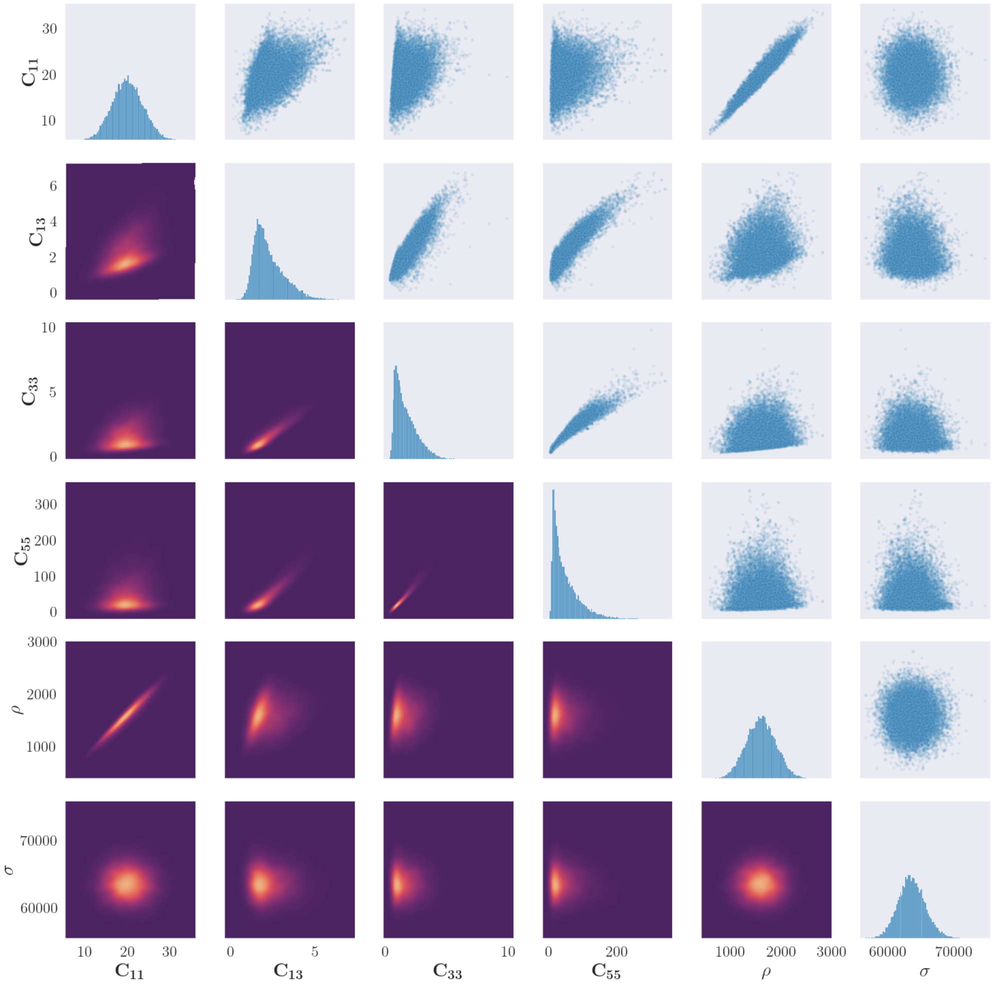

Figure 7.12: Results of the material property identification procedure for the propagation angle of 45°. Figures along the diagonal show the histogram of the samples for each parameter. Figures in the upper-right triangle, show a scatter plot of correlation between two parameters. Figures in the lower-left triangle, show a bivariate kernel density estimate of the cross-correlation between parameters, where lighter colours represent a larger value of the density.

Another repeated observation is of the pronounced 'edge' on some of the multivariate distributions; however, these edges are not as 'sharp' for these propagation angles. For a propagation angle of 135°, the posterior distribution for the C_{13} has a heavy skew towards zero, which may indicate that the curve solutions are too insensitive to this parameter to converge stably. More on the discrepancies of the results between these propagation angles can be deduced by looking at the distribution of the dispersion curves from the posterior samples.

Figure 7.14 shows the distributions of the curves taken from the posterior samples for the propagation angles which indicate propagation across the fibres. Because of the much larger attenuation of the S_0 mode when propagating through the fibres, there is no visible S_0 mode on the image data, so it is difficult to know whether the resulting S_0 curves are modelled well. However, for both angles it appears that the resultant curves for the A_0 mode are accurate. After the ridge-picking step, some additional points on the curve have been found for the propagation angle of 135°, which has clearly influenced the results of the sampling procedure. The horizontal blue lines that can be seen in Figure 7.14(a) are simply an artefact of the dispersion-curve solutions for material property combinations that are not possible. This would indicate that the method can benefit from observation of the curves at greater frequencies in order to better determine a valid combination of elastic constants.

Much like with the results of the procedure applied to propagation along the fibres, the univariate posterior distributions converge to different shapes, again indicating the important of the freedom in the posterior shape. In comparison to the results of the propagation along the fibres, all parameters appear to converge to a similar shape in the univariate posterior, although they have different statistical moments and expected values.

Statistical moments of the parameters

For each of the parameters, the expected value and variance are calculated for the samples from the posterior distributions for both angles, the results of which are shown in Table 7.4. The expected values of C_{33}, ρ and σ are similar for both propagation angles, whereas the expected values for C_{11}, C_{13} and C_{55} appear to change depending on the propagation angle. The largest of these changes is of the

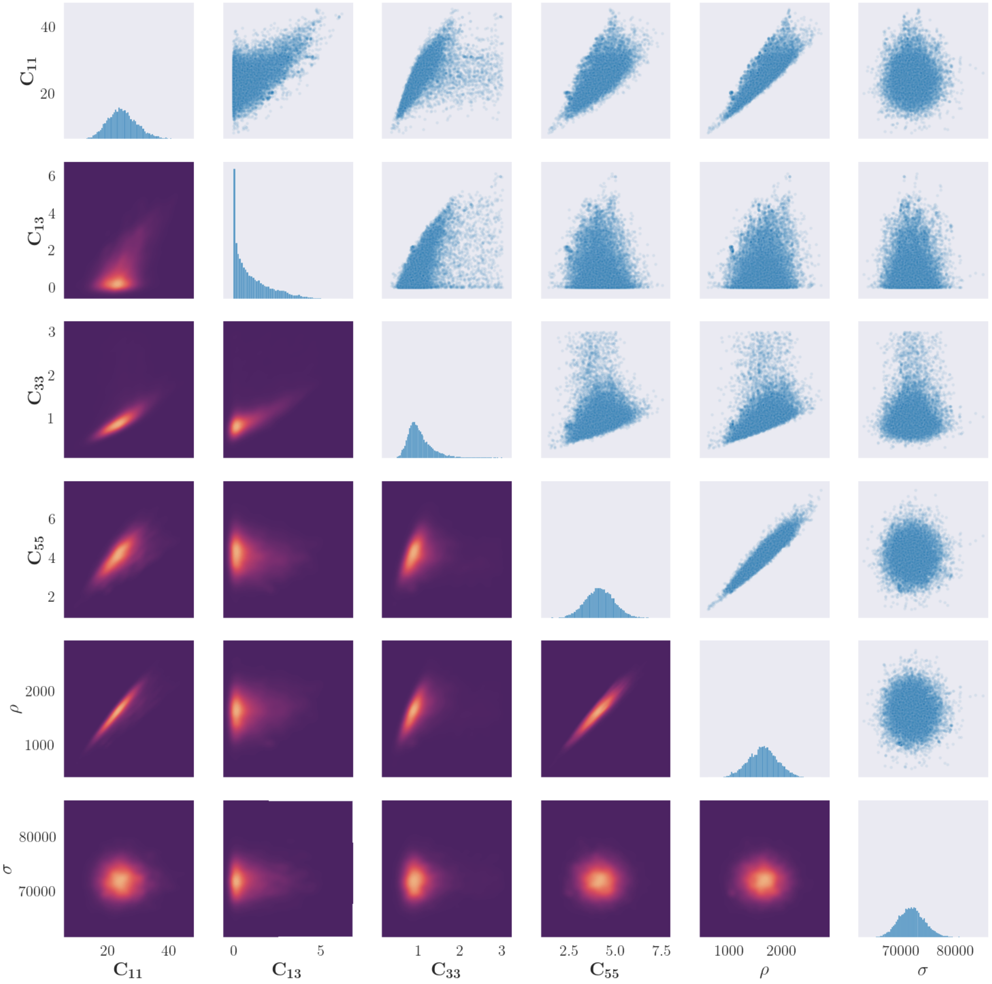

Figure 7.13: Results of the material property identification procedure for the propagation angle of 135°. Figures along the diagonal show the histogram of the samples for each parameter. Figures in the upper-right triangle, show a scatter plot of correlation between two parameters. Figures in the lower-left triangle, show a bivariate kernel density estimate of the cross-correlation between parameters, where lighter colours represent a larger value of the density.

value of C_{55}; however, this could be explained by looking at the distribution of curves in Figure 7.11. As there are additional points returned from the ridge-picking algorithm in the results for the propagation angle of 0°, the likelihood calculation

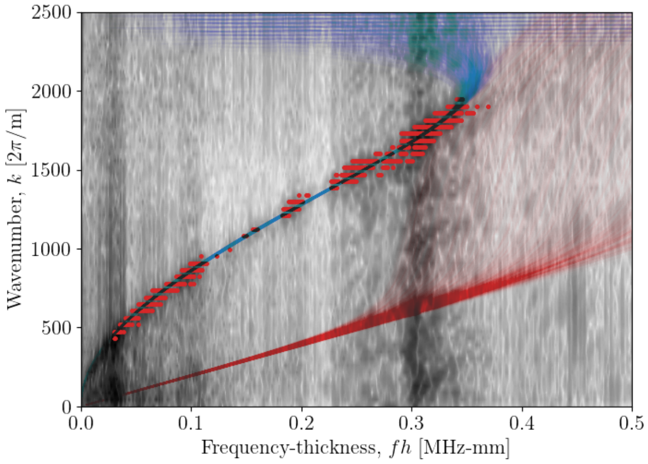

(a)

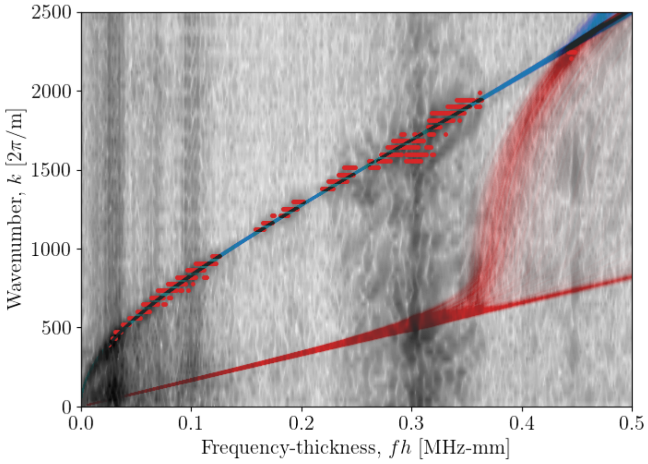

(b)

Figure 7.14: Distribution of generated dispersion curves for each sample taken for propagation angles of: (a) 45° and (b) 135°. The blue curves show the distribution of the A_0 mode and red curves show the distribution of the S_0 mode. The curves are overlaid on the image data taken from the 2DFT, and the red dots indicate the points taken from the ridge-selection algorithm which were used in the procedure as $\{\hat{\omega}, \hat{k}\}$.

is at a maximum when the S_0 curve has a shape which covers these points. The C_{55} elastic constant affects the S_0 curve past the 'elbow' (Section 7.1), and so these additional measured points will tighten the posterior distribution for C_{55}.

As the aim of the work here is to determine the dispersion characteristics useful for NDE/SHM strategies, a key motivation of which is to find the group velocity of the waves, it is also useful to look at the distribution of curves for this attribute. During the same curve sample-drawing procedure as above, the value of c_g was also calculated as the slope of the generated $[\omega\text{-}k]$ curves. The distributions of the $[\omega\text{-}c_g]$ curves for propagation angles of 0° and 135° are shown in Figure 7.15. Much like the curves seen in Figures 7.11 and 7.14, the distribution of the A_0 mode is much tighter than that of the S_0 mode. The shape of the c_g curves are similar for both propagation orientations; however, the velocity of the S_0 mode when propagating across the fibres is much lower.

From the results shown, the method presented here returns accurate and precise models of the dispersion curves for an arbitrary orthotropic plate. The objective problem of the work here was to determine dispersion-curve information on the A_0 mode, as this is the necessary information required for guided wave-based localisation. For the purposes of determining the dispersion characteristics from the data given to the procedure, it performs well. Without information on the S_0 curves, however, it does not seem to converge to a stable solution. This observation led to the adaptation of the procedure to include information from the S_0 mode, which was then applied to the wind-turbine blade coupon.

Parameter	0°		90°		45°		135°	
	$\mathbb{E}[\theta]$	$\mathbb{V}[\theta]$	$\mathbb{E}[\theta]$	$\mathbb{V}[\theta]$	$\mathbb{E}[\theta]$	$\mathbb{V}[\theta]$	$\mathbb{E}[\theta]$	$\mathbb{V}[\theta]$
C_{11}	47.06	156.8	25.79	21.91	19.92	13.54	24.87	24.57
C_{13}	3.005	4.486	1.255	0.132	2.252	0.797	1.048	1.111
C_{33}	1.051	0.185	1.018	0.206	1.699	0.846	1.064	0.160
C_{55}	3.746	0.513	27.03	272.1	49.76	1632	4.128	0.590
ρ	1,621.8	88,587	1,617.2	82,563	1,592.9	87,996	1,637.2	81,332
σ	65,946	5.67e6	64,551	5.99e6	63,653	4.05e6	71,987	5.72e6

Table 7.4: Expected value (arithmetic mean) and variance calculated from the samples drawn from the posterior for each parameter and various propagation angles on the CFRP plate.

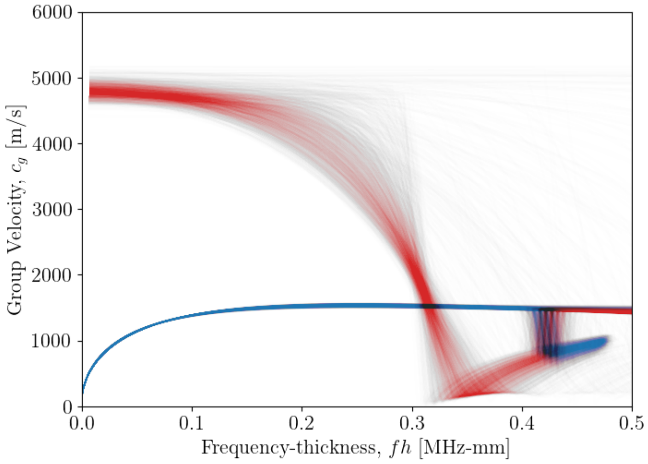

(a)

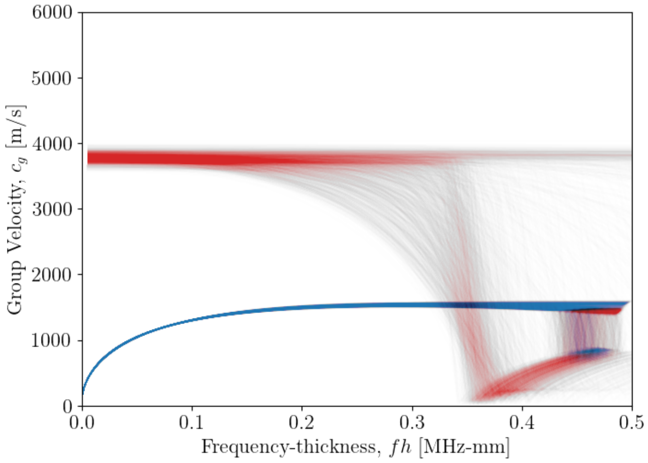

(b)

Figure 7.15: Distribution of calculated $[\omega\text{-}c_g]$ curves for each sample taken for propagation angles of (a) 0° and (b) 135°. The blue curves show the distribution of the A_0 mode and red curves show the distribution of the S_0 mode.

7.4 Chapter summary

This chapter has presented the novel methodology developed for a Bayesian approach to material identification using Lamb wave dispersion curves. The results show that the method has worked well for determining accurate models for dispersion curves, through material property identification. By comparing the results of the orthotropic model applied to a fibre-weave plate and unidirectional fibre plate, the importance of the model used for the solutions is apparent. Not only does this method work well for dispersion curve determination, it shows promise for full material identification. In comparison to previous methods, the work shown here allows for simulation of the posterior distribution in both a univariate and multivariate case. Further discussion on the conclusions and benefits of this method, and other work shown in this thesis, are discussed in the next chapter.

8

CONCLUSIONS

8.1 Concluding remarks on the work presented

The motivation behind this thesis was to develop modern, unique and novel tools which advance the understanding, and use of, ultrasonic guided waves in composite structures, with a context around SHM/NDE techniques. Ultrasonic guided waves were chosen as the topic of research, as they have distinct advantages over lower-frequency or more passive techniques. After researching and reviewing the current state-of-the-art for application of guided waves to fibre-composite materials, it was concluded that there is room for development of some novel tools which can overcome some of the difficulties of UGWs in complex materials. In particular, the use of probabilistic and machine learning methods were used to develop more generalised methodologies, which are readily expandable to other material/system types. Therefore, the aim of this work was to develop novel probabilistic tools for application of guided waves in damage detection of fibre-composite materials.

Firstly, Chapter 1 introduced the general concepts of NDE/SHM, ultrasonic guided waves, and the challenges that need to be overcome. Chapter 2 then reviewed the literature available on topics used in this thesis, highlighting the gaps in research that this thesis aimed to fill. Chapter 3 gave an overview of the physics of ultrasonic guided waves, and a brief overview of the numerical/analytical modelling methods used. Probabilistic methods were applied in all the novel work of this thesis, and the machine-learning methods which fall under this category were detailed in Chapter 4. Novel work is then shown in all the remaining chapters of the thesis. This portion begins with Chapter 5, which shows the informed Gaussian process tools developed for modelling features spaces of ultrasonic guided waves. Following this, Chapter 6 showed the multi-stage probabilistic approach to Lamb-wave signal decomposition, with the focus on damage localisation using reflected waves. The last chapter of novel material is Chapter 7, which shows the Bayesian approach to material identification of a plate using Lamb-wave dispersion curves.

The experimental portions of this work were in Chapters 5 and 7, where a scanning-laser Doppler vibrometer was used to record Lamb-wave propagation on the surface of the coupons being tested. Clearly, the aim here is not to generate the final-stage detection strategy, but instead to develop tools for the initial stages of strategy development, where prerequisite knowledge is determined. The advantage of using the SLDV is in the ability to measure with a large spatial density, which would otherwise be impossible using physical sensors. For the feature-space modelling work in Chapter 5, this characteristic is useful, as a large amount of information is needed for learning algorithms. However, as noted in Chapter 2, one benefit of including physics in the learning of a mapping allows for the use of fewer data points, and so the methodology could be applied to more sparse sensor arrays – such as a PZT pitch-catch matrix. For the material identification stage, the importance of the sensor density can be discussed with relation to the measured observations. The [ω-k] image data for the GFRP coupon appears to encapsulate the full range of the wavenumber for the modes present, and as the wavenumber range is proportional to the spatial density, this is a direct result of using the SLDV.

A continuing trend with difficult analytical/numerical modelling problems is to shift to a data-driven approach; this is useful for systems that are easily generalised or where the system/design does not change. However, the work in Chapter 5 showed that embedding physics into the learning improves the generation of guided-wave feature spaces. This also has other advantages such as extrapolability and better performance in learning.

A barrier to progress in of using guided waves in an NDE or SHM strategy, is the difficulty of modelling the behaviour of these waves in complex materials. The work presented in Chapter 5 shows promising steps towards generating a physics-incorporated, data-driven model for the feature space of guided waves in such materials. Several characteristics of such a strategy, which must be carefully considered to maintain robustness, have been discussed. This strategy provides a key framework for the development of guided-wave models for complex materials – such as those in a wind turbine blade – by allowing modelling of features which define the waves propagating throughout the material. The important distinction of this combined method, in comparison to physics-only or data-driven-only methods, is that it allows physics to guide the model, whilst allowing unknown or undescribed physical mechanisms to be incorporated via the data-driven aspect.

When initially looking at the kernels chosen to represent different learning strategies and levels of constraint, it is not clear which strategy will result in the optimal model output. By various quantitative assessment values, it is possible to see how each model fits in comparison to the validation data, in different aspects. By leaving the model uninformed, it is possible to get a closer fit to the training and validation data in terms of difference between the predicted and measured values. However, by guiding the learning process using physics-based implementation of the problem, it is possible to get a higher-likelihood model.

The localisation of damage using Lamb-wave reflections, requires the decomposition of received signals to determine the reflection arrival time. Chapter 6 presented a methodology for localisation of damage using ultrasonic guided waves, by simulating Lamb waves in an aluminium plate. The overall strategy involves decomposing measured single-source signals, from which residual signals can be determined which contain reflected waves, which are then used to triangulate the reflection source. The decomposition stage uses a Bayesian approach in order to generate a distribution of possible nominal waves, allowing better determination of uncertainty. In particular, the full-field decomposition strategy was designed for use in systems where accurate physical models of signals are difficult to obtain. In Chapter 6, the accuracy of the decomposition and localisation methods were shown. Inaccurate location was found to be largely because of the influence of boundary reflections, which is not likely to be an issue in future applications, as the plate shown here was of small size.

Discussion was made in Chapter 6, on the importance of prior knowledge on the localisation strategy, and how to improve the methodology if this information was not known. One such method for triangulation, when the prior knowledge is limited, or imprecise, is to use a probabilistic approach. In particular, fibre-composite materials causing propagation-angle-dependent wave velocities and unknown wave mode conversion. As the methodology shown here is probabilistic, it lends itself well to a probabilistic triangulation, as the uncertainty and likelihood calculations can be propagated through.

Previous decomposition methods required either instantaneous full-field information, or accurate physical models – which are only available for simple systems. Using a finite-difference method which can model complex multi-mode interactions, a probabilistic decomposition method was presented in Chapter 6. This method allows for a quantification of uncertainty, as well as returning parametric features which correspond with known physics of wave behaviour.

Chapter 7 presented a novel methodology developed for a Bayesian approach to material identification using Lamb-wave dispersion curves, which indicated the promise of the method for its application to, and use of, guided waves. A unique advantage of this method against others is the freedom in the estimation of the family or shape of the posterior of the parameters, for both the univariate and multivariate distributions. This freedom was shown to be necessary; the univariate posteriors appear to converge to different shapes, and there are clear and different correlations in the multivariate posterior.

To begin, the orthotropic model-identification procedure was applied to a carbon-fibre-weave plate, and showed the initial potential of the method. However, as only information on the A_0 mode was available, and sensitivity of the curves was not exhaustive on this mode, more information was needed to improve the procedure. Therefore, when applying the method to the wind turbine blade coupon, an alternative experimental approach, and updated likelihood, was used to include both the A_0

and S_0 modes. This addition showed great improvements to the identification results when applied to propagation along the fibres. When applied to propagation across the fibres, the converged parameter combination does not appear to be accurate, showing that consideration of the model being used is important for this procedure.

With respect to the objective of generating dispersion curves for a material in order to determine dispersive characteristics, in particular group velocity, this method was shown to work well. Using the procedure, a distribution of estimated dispersion curves was also generated, which, by observation, had low uncertainty and the measured data fit well within these distributions. This low uncertainty is useful for localisation purposes, as the small wavelength indicates that an accurate group velocity is required.

8.2 Future Work

As with any research, the work shown has opened up many other pathways for improvement, implementation, and testing of the work shown here. This section will detail future work which the author believes to be the next steps in the tools developed here.

8.2.1 Pathway to application on wind turbine blades

The work presented here was motivated by the possibility of using UGWs as a method for detecting damage in wind turbine blades. There are several steps that should be studied and researched to aid progression towards application of UGWs in wind turbine blades, using the tools developed in this thesis. With respect to the feature-space modelling, work can be done to test the method on structures that are more similar to that found in the construction of WTBs. The work shown here was to test and demonstrate initial capabilities of the method, but WTBs also include additional complexities, such as, embedded wooden cores, web joints across the internal structure, and discontinuous fibre orientations. Additional kernels could be designed which incorporate knowledge of how such features of WTBs affect the attenuation mechanisms (and other characteristics of UGW propagation).

For the wave decomposition and localisation methodology, the next key stage for application to WTBs would be to develop and test the determination of the nominal wave dictionary (NWD) for a known location on the WTB structure. A vital step would be the validation of this NWD model, in particular for allowing generalisation of the model to known parameters. Such parameters may be; relative fibre-orientation, local structural complexities, and material layup.

Finally, for the material identification procedure, it would be useful to verify the method on a variety of locations within the blade. The Legendre polynomial expansion approach is readily applicable to layered materials, and improvements to the methodology outlined in Chapter 7 is discussed later regarding more complex models for the dispersion curve solutions. For progression to application on WTBs, it would be beneficial to test the method on locations which have different material layouts. Furthermore, it may be useful to look into adapting the algorithm for on-line use, so that dispersion curve information can be updated during operation on the structure.

8.2.2 Additional tests and improvements of feature space learner

The feature-space model-generation strategy presented in Chapter 5 was employed on a dataset of energy-based features, which will follow an attenuation model. This forms the basis of the physics embedding, as the kernel designs were based on different attenuation mechanisms. The first potential avenue for expanding upon this method is to develop kernels for features which are described by different physical mechanisms – such as time of flight, central frequency, etc. Another alternate kernel design improvement could be to embed knowledge on complex multi-mode interaction and physics descriptions, e.g. amplitude ratio.

Improvements could also be made on the Gaussian process approach shown in this work. Some improvements could be to include additional an attenuation mechanism; namely, dispersive attenuation, which is associated with the central frequency of the wave. For this addition, an additional dimension of the input would be required to include the central frequency of the wave. There are many models available for solutions to dispersive attenuation, though these are numerical procedures –

they are modelled using dispersion-curve solutions. Work could be done on the feasibility of including this numerical definition of the dispersive attenuation into the Gaussian-process kernels.

From the results of the expected variance of the learned models, there is an enforced asymptotic behaviour from the equations governing the attenuation mechanisms. Further improvements could be made to the kernels by allowing for a finite value of these energy-based features. However, it may be argued that this is unnecessary as the feature space needs only be accurate further away where sensors will be deployed.

Another progression of this method would be to test the extrapolability of the learner using the physics, by reducing the radius of sensing and assessing its performance compared to a testing set of points outside of this radius. As well as extrapolation in the spatial dimensions, tests could also be done on extrapolation in additional dimensions discussed above, such as frequency. Furthermore, an assessment could be performed on the number of data points used in modelling, as an advantage of physics embedding is the lower number of training points required for accurate modelling.

8.2.3 Using feature-space models to better understand guided waves in composite media

As well as testing further adaptations and improvements on the feature-space model-generation method, the strategy developed here can be used to further understanding guided wave phenomena in fibre-composite materials. The results shown in Chapter 5 show that there are more than just the two attenuation mechanisms included in the model, and that any additional mechanisms vary over the propagation angle. From this initial set of results applied to this method, there are already some observations made. Via additional testing on varying fibre, layup and material types, using the feature-space learner applied here could allow for better understanding of these additional attenuation mechanisms.

As well as applying the learning method shown here, further work could be done to develop a parametric, physics-informed model generation strategy. By adapting the method in this way, in particular to make inferable parameters, additional mechanisms could be more than understood, but also *quantified.* This further work could also be applied to features which demonstrate other physical phenomena, linking to the above-mentioned improvements that could be done to this work.

8.2.4 Further work on aspects of uncertainty

The probabilistic approaches used in this work have an advantage, in that they readily allow for quantification of the confidence in features, values, and measurements. In this subsection, several avenues of further work are proposed which relate to the uncertainty returned from the tools presented in this thesis.

A particular advantage of the decomposition method shown in Chapter 6 is the quantification of uncertainty in the decomposed signal. In this work, that uncertainty was used to discuss the level of confidence one has in the decomposed signal, but in a qualitative manner. Some further work that the author suggests, is to develop a method of propagating this uncertainty from the decomposition to the uncertainty in the location. One possible avenue of exploration could be quantifying the path of uncertainty through the values of; reflection signal, signal onset, time-of-flight and damage location.

The uncertainty, at several stages of each method, could be compared to a more 'statistical' quantification of uncertainty, where multiple observations are used to generate the uncertainty distribution. In particular, for the localisation method, these comparisons could be made at several stages of the methodology. For the feature space modelling method, shown in Chapter 5, this comparison could be done by quantifying the uncertainty using multiple tests and coupons.

The Bayesian linear regression approach here assumes a Gaussian prior and likelihood, and so the posterior must also be Gaussian. This assumption means that a constraint is placed on the shape of the posterior for the signal decomposition shown in Chapter 6. Work could be done to determine if this constraint on the posterior has any implications for the uncertainty – in particular with respect to the uncertainty propagation through to location. Furthermore, tests could be done to determine if the posterior distributions change when applied to different phenomena.

The main motivation behind the work of Chapter 7 was to determine accurate dispersion-curve solutions for a given system, in order to obtain an accurate group velocity for localisation purposes. The samples from the posteriors can be used to quantify uncertainty in the material parameters, as well as allowing one to generate a posterior distribution of the dispersion curves. It may be useful to assess how each of these distributions affects the uncertainty in localisation. This assessment could be done by determining a method of propagating the quantified uncertainty, or by testing the accuracy of systems with large uncertainty and systems with smaller uncertainties. As well as this, any interaction between the uncertainty in the parameters and uncertainty in the curves could be studied.

8.2.5 Improving Bayesian material identification

The work in Chapter 7, showed that the model used for the dispersion-curve solutions is an important consideration in the material identification stage, even when the objective is just to determine an accurate curve with respect to the observed data. The applicability of the method to different dispersion-curve models is an encouraged avenue of research, and whether there is a limit to the model complexity. It is clear that the model applicability and fit would be highly dependent on a lot of factors, such as; the dimensionality of the parameter space, the fidelity of the model in comparison to the complexity of the system/material being measured, and the number and type of wave modes being included. In addition to this, work could be done to assess what sort of model reduction can be applied to given material types, whilst maintaining accuracy in the solutions. For example, can a transversely-isotropic model be used in place of an orthotropic model to reduce the dimensionality of the parameters?

With respect to the orthotropic model approach used here, some further work could be done on including the rotation of the stiffness matrix for more accurate modelling of propagation through the fibres. This adaptation would result in a much less sparse stiffness matrix being required, and therefore, a larger number of parameters are required to be sampled over. However, this also means there is only a need for a single sampling procedure applied to all propagation angles simultaneously, although this does not balance the increased computational expense.

As many of the improvements on this procedure will likely lead to increased computational expense, there is a need for research into the performance of the procedure for this application. One such avenue of research would be to reduce the order of dimensionality of the parameter space. The results of the sampling procedure showed correlation between many of the parameters, which varied between propagation angles and material types. Using both probabilistic and machine-learning approaches, a study could be done on determining a reduction mapping; the simplest of which would be a method such as principal component analysis, or locally-linear embedding. For all propagation angles and materials, there was a strongly linear correlation between the parameters C_{55} and ρ. Therefore, an obvious first step may be to utilise physical knowledge of material behaviour to apply dimensionality reductions, although this will be dependent on the fidelity of the model used.

Another potential method of increasing performance, is to determine a multivariate prior over the parameter space, which would improve sampling by reducing the number of rejected samples. More on this will be discussed in the next subsection.

8.2.6 Determination of space of valid elastic constants

For the posterior-sampling procedure in Chapter 7, any invalid parameter combinations were rejected from the sampling. This rejection was done by detecting any combinations which resulted in any eigenvalue in the solution being less than zero. However, this causes a reduction in model performance, as it creates a discontinuity in the valid parameter space. Furthermore, as the priors were assumed independent here, sampling performance could be improved via the use of a multivariate prior on the full dimensionality of the parameter space.

A solution to both these aspects which affect sampling performance, is to determine the valid space of material properties, with respect to dispersion-curve solutions. This implementation would also allow for more physically-meaningful parameters in the prior for other Bayesian analysis methods. An initial idea would be to define this space based on the requirement that all eigenvalues of the matrix A be less than zero, which would define this matrix to be a negative-definite matrix. There are many tools to determine *if* a matrix is negative definite; however, they are not *required*; i.e.

these definitions are non-exhaustive. In addition to this, these definitions would be extremely difficult to propagate backwards onto the material property space through the Legendre-polynomial expansion approach.

There are multiple approaches that could be done to determining the space of valid elastic constants. One such example would be to determine whether an analytical prior can be defined using the constitutive equations which govern the interaction between stiffness tensor components. For isotropic materials, this would be trivial using the equations relating the parameters c_L, c_T and ρ. Another approach would be to use the definition of valid material property combinations to generate samples of the valid space. Using these samples, a more data-based approach can be applied to determine an empirical definition of this space, some examples of which are; manifold learning, or topological data analysis.

9

ADDITIONAL WORK

As well as the studies and results presented in this thesis, the author completed several other pieces of work during the course of their PhD programme that they feel are worth highlighting here. As a result of either being extracurricular to this project, or unfortunate circumstances, the following work was not included in the main body of this thesis. One such of these works is the development of an experimental system for investigating guided waves in a full-scale wind turbine blade, with varying levels and types of damage. This work was intended to be a critical part of the thesis, however, the resulting data was unfortunately lost due to a clerical error out of the authors hands. The extracurricular activity that will be mentioned is the creation of an extensive experimental dataset for modal analysis of glider wings under varying environmental conditions, damage states, and simulated damage.

Full-Scale Wind Turbine Blade Damage and Fatigue Test

As part of the initial plan for the thesis, in partnership with Siemens Gamesa Renewable Energy, an experimental test investigating guided wave propagation in a full-scale wind turbine blade was designed. The test was to be performed during the cycle of an ongoing fatigue test on the blade, where damage was to be introduced to the structure, and the growth of this damage monitored under fatigue loading. The guided wave system was designed, developed, built, and maintained in order to allow autonomous collection of the required data. Additionally, due to travel limitations during the pandemic, the system had to be built to be operated remotely and set up by an external technician.

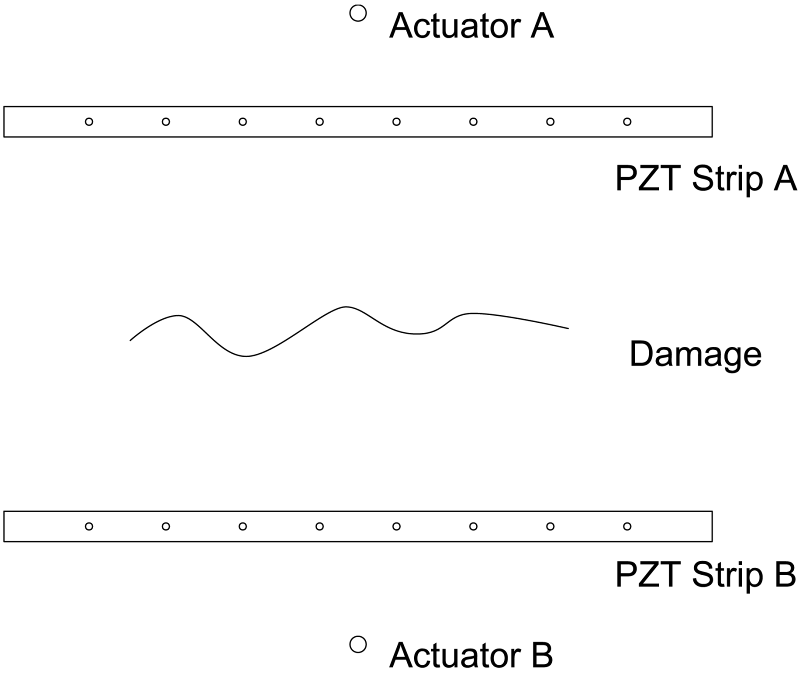

Figure 9.1: Layout of sensors and actuators with respect to the damage for full-scale wind turbine blade UGW experiment. Distances are not to scale.

The same layout was used for each damage case, in each location of the blade, and is shown in Figure 9.1. For actuation of the UGWs, a pair of Physik Instrumente P-016.20P Stack Actuators were placed on either side of the damage, and were supplied with a specified actuation signal. Because of the large thickness of the structure, PZT stack actuators (PZTSA) were used in order to supply enough energy to induce guided waves. The PZTSAs were actuated one at a time and synchronised with the acquisition in order to time-align the wave measurements in all directions and distances. For wave sensing, an array of evenly-spaced PZT sensors were placed on both sides of the damage (as shown in Figure 9.1) using Accellent Smart Layer®Sensors. The PZTSAs and sensing PZTs were placed in order to analyse the wave propagation before and after the damage, in both directions.

The system was designed and programmed in LabView™, with the programme flowchart shown in Figure 9.2. In order to test the effects of dispersion characteristics and frequency-driven attenuation mechanisms, a variety of actuation source signals were used.

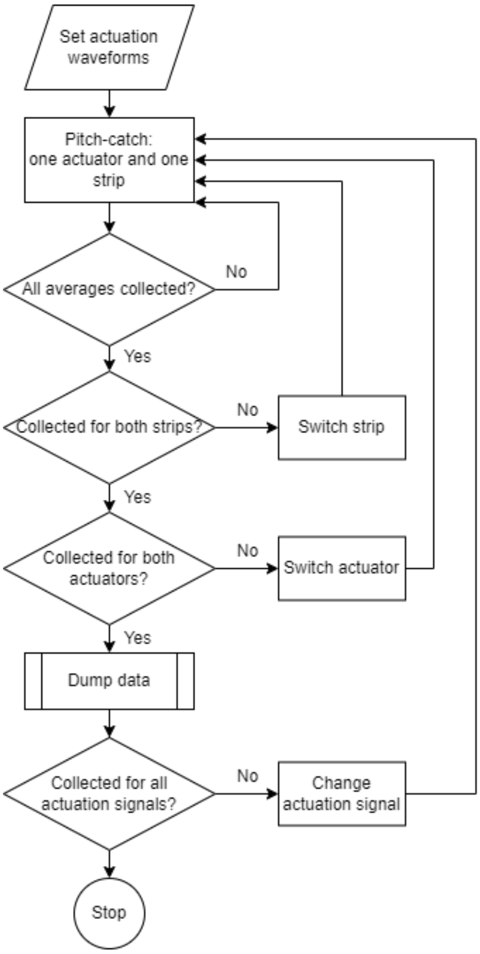

Figure 9.2: Flowchart of pitch-catch acquisition system.

Glider Wing Modal Analysis Dataset

The research interests of the author cover NDE and SHM techniques which utilise other methods, such as modal characteristics, which are well known to be damage-sensitive. Several challenges still hinder progress in the practical application of such techniques, and generalising SHM techniques. Such challenges include operational and environmental fluctuations, repeatability issues, and changes in boundary conditions. For SHM methodologies based on techniques such as machine learning, this can cause issues as these changes in conditions may be incorrectly flagged as damage, as the modal characteristics are changed. Accounting for these variations is especially important for population-based SHM, which seeks to transfer valuable information, including normal operating conditions and damage states, across similar structures. So, an experimental campaign was designed to create a modal dataset of a set of nominally-similar structures, with data collected at various environmental conditions and damage states – the latter being both practical and simulated.

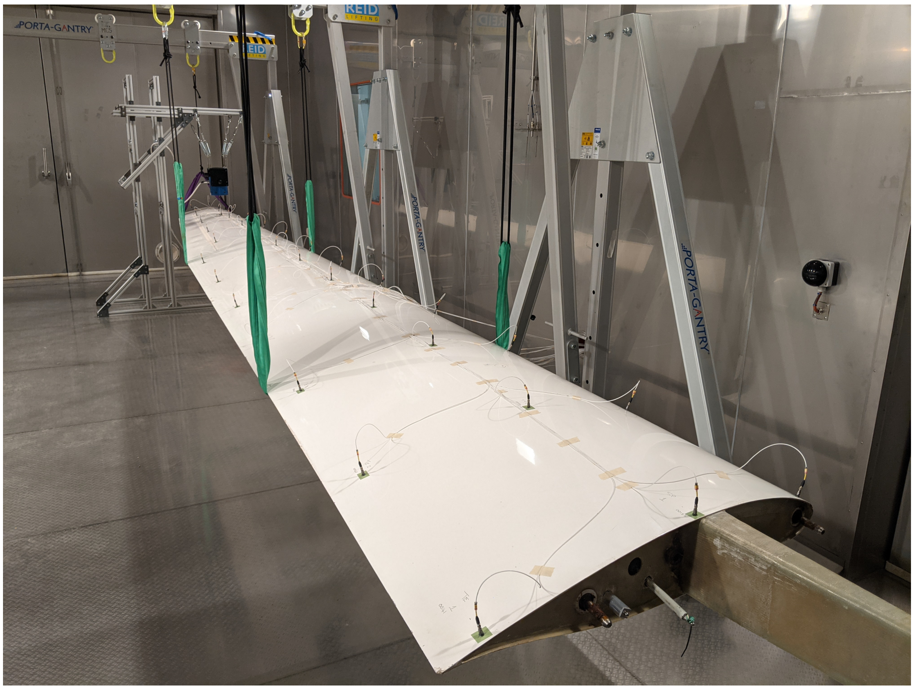

Figure 9.3: Glider wing in temperature-controlled chamber.

The structures chosen were four full-scale, 6.45-metre composite Astir glider wings, where one of the wings had naturally-occurring damage, an example of one setup for testing is shown in Figure 9.3. The details of these wings is shown in Table 9.1. Thirty-six uniaxial 10 mV/g accelerometers were placed at various locations along

Wing ID	Side	Damage State
A1	Starboard	Undamaged
A2	Port	Damaged
B1	Starboard	Undamaged
B2	Port	Undamaged

Table 9.1: Side and damage state of each of the wings tested during experimental campaign. The first letter of the Wing ID indicates the original glider which the wing was from.

the underside of each wing, and time signal data was acquired using Siemens PLM LMS SCADAS hardware and software. The same accelerometers were used on each wing, and care was taken to ensure that they were attached to the same locations on each wing. The locations of these sensors are shown in Figure 9.4. The shaking force was done using electrodynamic shakers, suspended with elastic cords from a gantry frame, in order to minimise any external blocking forces which may influence the input spectra.

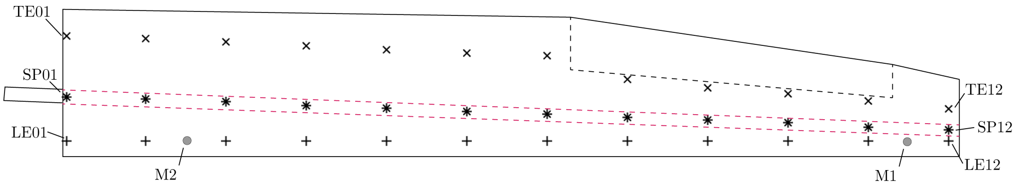

Figure 9.4: Layout of sensors on the Astir glider wings.

For the undamaged wings, additional masses were placed at specified locations to simulate the effects of damage on the structure. It is common practice in experimental work for vibration-based SHM techniques to add mass to the structure, as this has a similar effect to the reduction in stiffness that occurs as a result of damage [146]. The locations of these masses are also shown in Figure 9.4. Both masses were 64g in weight and attached using suction cups to not influence internal properties of the structure. Data was acquired with each mass placed individually, and both masses on simultaneously.

This dataset has already shown to be useful in developing and verifying SHM techniques which can overcome some of the difficulties mentioned above [147]. The publication of the dataset and accompanying journal paper are being developed by the author.

Publications

The following articles are the publications for which the author of this thesis is a contributing author on, completed during the project for which this thesis covers.

Journal Publications

M.Haywood-Alexander, N. Dervilis, K. Worden, T.J. Rogers. “A Bayesian Method for Material Identification of Composite Plates via Dispersion Curves” Mechanical Systems and Signal Processing (2022).

M. Haywood-Alexander, N. Dervilis, K. Worden, G. Dobie, T. J. Rogers. “Informative Bayesian Tools for Damage Localisation by Decomposition of Lamb Wave Signals”. Journal of Sound and Vibration ISMA2020 Special Issue (2021)

M. Haywood-Alexander, N. Dervilis, K. Worden, E.J. Cross, R.S. Mills, T.J. Rogers. “Structured Machine Learning Tools for Modelling the Characteristics of Guided Waves”. Mechanical Systems and Signal Processing (2021).

L.A. Bull, P.A. Gardner, N. Dervilis, E. Papatheou, M. Haywood-Alexander, R.S. Mills, K. Worden. “On the Transfer of Damage Detectors Between Structures: An Experimental Case Study”. Journal of Sound and Vibration (2021).

L.A. Bull, P.A. Gardner, N. Dervilis, E. Papatheou, M. Haywood-Alexander, R.S. Mills, K. Worden. “Transferring Damage Detectors Between Tailplane Experiments”. Chapter in Data Science in Engineering, Volume 9 (2022).

Conference Publications

M. Haywood-Alexander, N. Dervilis, K. Worden, T.J. Rogers. “On The Space of Valid Elastic Constants for Lamb Wave Propagation for Orthotropic Materials” (2022)

M. Bonney, G. Tsialiamanis, M. Haywood-Alexander, R.S. Mills. “Snapshot Model Updating of RAF T1A Hawk Using a Digital Twin Operational Platform” (2022)

M. Haywood-Alexander, N. Dervilis, K. Worden, T. J. Rogers. “Bayesian Identification of Material Properties for a Fibre-Composite Plate Via Dispersion Curves”. Submitted to 9th International Conference on Uncertainty in Structural Dynamics (2022)

T.A. Dardeno, M. Haywood-Alexander, R.S. Mills, P.A. Gardner, L.A. Bull, N. Dervilis, K. Worden. “Investigating the Effects of Ambient Temperature on Feature Consistency in Vibration-Based SHM”. Submitted to International Workshop in Structural Health Monitoring (2022)

M. Haywood-Alexander, N. Dervilis, K. Worden, T. J. Rogers. “A Bayesian Approach to Lamb-Wave Dispersion Curve Material Identification in Composite Plates”. Submitted to European Workshop on Structural Health Monitoring (2022)

M. Haywood-Alexander, K. Worden, T.J. Rogers, N. Dervilis. “Decomposition of Multi-Mode Signals Using Dispersion Curves and Bayesian Linear Regression” Health Monitoring of Structural and Biological Systems XV (2021).

M. Haywood-Alexander, K. Worden, G. Dobie, T.J. Rogers, N. Dervilis. “Lamb Wave Mode Separation Using Dispersion Curves”. 8th International Conference on Uncertainty in Structural Dynamics (2020).

L.A. Bull, P.A. Gardner, J. Gosliga, T.J. Rogers, M. Haywood-Alexander, N. Dervilis, E.J. Cross, K. Worden. “Towards Population-based Structural Health Monitoring, Part I: Homogeneous Populations and Forms”. Proceedings of IMAC XXXVIII – the 38th International Modal Analysis Conference (2020).

M. Haywood-Alexander, T.J. Rogers, K. Worden, R.J. Barthorpe, E.J. Cross, N. Dervilis. “Modelling of Guided Waves in a Composite Plate Through a Combination of Physical Knowledge and Regression Analysis”. Proceedings of IMAC XXXVIII – the 38th International Modal Analysis Conference (2020).

M. Haywood-Alexander, K. Worden, R. Barthorpe, R. Fuentes, T. Rogers, N. Stevanovic, N. Dervilis. “Health Monitoring of Composite Structures by Combining Ultrasonic Wave Data”. International Workshop in Structural Health Monitoring (2019).

BIBLIOGRAPHY

[1] C. R. Farrar and K. Worden, *Structural Health Monitoring: A Machine Learning Perspective.* John Wiley & Sons, 2012.

[2] A. Rytter, *Vibrational Based Inspection of Civil Engineering Structures.* PhD thesis, University of Aalborg, 1993.

[3] M.-Y. Lyu and T. Choi, "Research trends in polymer materials for use in lightweight vehicles", *International journal of precision engineering and manufacturing*, vol. 16, no. 1, pp. 213–220, 2015.

[4] V. Giurgiutiu, *Structural health monitoring of aerospace composites.* Academic Press, 2015.

[5] Z. Zhang, M. He, A. Liu, H. Singh, K. Ramakrishnan, D. Hui, K. Shankar, and E. Morozov, "Vibration-based assessment of delaminations in FRP composite plates", *Composites Part B: Engineering*, vol. 144, pp. 254–266, 2018.

[6] J. McCrory, S. Al-Jumaili, D. Crivelli, M. Pearson, M. Eaton, C. Featherston, M. Guagliano, K. Holford, and R. Pullin, "Damage classification in carbon fibre composites using acoustic emission: A comparison of three techniques", *Composites Part B: Engineering*, vol. 68, pp. 424–430, 2015.

[7] N. Takeda, Y. Okabe, and T. Mizutani, "Damage detection in composites using optical fibre sensors", *Proceedings of the Institution of Mechanical Engineers, Part G: Journal of Aerospace Engineering*, vol. 221, no. 4, pp. 497–508, 2007.

[8] S. Russell and E. Henneke, “Signature analysis of acoustic emission from graphite/epoxy composites”, tech. rep., 1977.

[9] M. Suzuki, H. Nakanishi, M. Iwamoto, and E. Jinen, “Application of static fracture mechanisms to fatigue fracture behavior of class A-SMC composite”, in *Japan-U. S. Conference on Composite Materials, 4 th, Washington, DC*, pp. 297–306, 1989.

[10] P. De Groot, P. Wijnen, and R. Janssen, “Real-time frequency determination of acoustic emission for different fracture mechanisms in carbon/epoxy composites”, *Composites Science and Technology*, vol. 55, no. 4, pp. 405–412, 1995.

[11] K. Komai, K. Minoshima, and T. Shibutani, “Investigations of the fracture mechanism of carbon/epoxy composites by AE signal analyses”, *JSME international journal. Ser. 1, Solid mechanics, strength of materials*, vol. 34, no. 3, pp. 381–388, 1991.

[12] W. Haselbach and B. Lauke, “Acoustic emission of debonding between fibre and matrix to evaluate local adhesion”, *Composites science and technology*, vol. 63, no. 15, pp. 2155–2162, 2003.

[13] C. Ramirez-Jimenez, N. Papadakis, N. Reynolds, T. Gan, P. Purnell, and M. Pharaoh, “Identification of failure modes in glass/polypropylene composites by means of the primary frequency content of the acoustic emission event”, *Composites Science and Technology*, vol. 64, no. 12, pp. 1819–1827, 2004.

[14] R. Gutkin, C. Green, S. Vangrattanachai, S. Pinho, P. Robinson, and P. Curtis, “On acoustic emission for failure investigation in CFRP: Pattern recognition and peak frequency analyses”, *Mechanical systems and signal processing*, vol. 25, no. 4, pp. 1393–1407, 2011.

[15] M. Venturini Autieri, *Acoustic emission characterisation of damage in CFRP composites.* PhD thesis, University of Southampton, 2007.

[16] D. Valentin, P. Bonniau, and A. Bunsell, “Failure mechanism discrimination in carbon fibre-reinforced epoxy composites”, *Composites*, vol. 14, no. 4, pp. 345–351, 1983.

[17] P. Beaumont, “The failure of fibre composites: an overview”, *The Journal of strain analysis for engineering design*, vol. 24, no. 4, pp. 189–205, 1989.

[18] C. Debel, “Identification of damage types in wind turbine blades tested to failure”, in *Materialeopførsel og skadesanalyse* (M. Somers, ed.), pp. 123–127, Dansk Metallurgisk Selskab, 2004.

[19] I. De Rosa, C. Santulli, and F. Sarasini, “Acoustic emission for monitoring the mechanical behaviour of natural fibre composites: A literature review”, *Composites part a: applied science and manufacturing*, vol. 40, no. 9, pp. 1456–1469, 2009.

[20] W. Van Paepegem, I. De Baere, and J. Degrieck, “Modelling the nonlinear shear stress–strain response of glass fibre-reinforced composites. part I: experimental results”, *Composites Science and Technology*, vol. 66, no. 10, pp. 1455–1464, 2006.

[21] W. Van Paepegem, I. De Baere, and J. Degrieck, “Modelling the nonlinear shear stress–strain response of glass fibre-reinforced composites. part II: Model development and finite element simulations”, *Composites Science and Technology*, vol. 66, no. 10, pp. 1465–1478, 2006.

[22] A. Abdul-Aziz, G. Baaklini, D. Zagidulin, and R. Rauser, “Challenges in integrating nondestructive evaluation and finite-element methods for realistic structural analysis”, in *Nondestructive Evaluation of Aging Materials and Composites IV*, vol. 3993, pp. 35–46, International Society for Optics and Photonics, 2000.

[23] R. Marani, D. Palumbo, U. Galietti, E. Stella, and T. D’Orazio, “Automatic detection of subsurface defects in composite materials using thermography and unsupervised machine learning”, in *2016 IEEE 8th International Conference on Intelligent Systems (IS)*, pp. 516–521, IEEE, 2016.

[24] K. Lee, A. Aihara, G. Puntsagdash, T. Kawaguchi, H. Sakamoto, and M. Okuma, “Feasibility study on a strain based deflection monitoring system for wind turbine blades”, *Mechanical Systems and Signal Processing*, vol. 82, pp. 117–129, 2017.

[25] M. Wymore, J. V. Dam, H. Ceylan, and D. Qiao, "A survey of health monitoring systems for wind turbines", *Renewable and Sustainable Energy Reviews*, vol. 52, pp. 976–990, 2015.

[26] H. Lee, M. Kang, and J. Park, "Fatigue failure of a composite wind turbine blade at its root end", *Composite Structures*, vol. 133, pp. 878–885, 2015.

[27] J.-S. Chou, C.-K. Chiu, I.-K. Huang, and K.-N. Chi, "Failure analysis of wind turbine blade under critical wind loads", *Engineering Failure Analysis*, vol. 27, pp. 99–118, 2013.

[28] X. Chen, W. Zhao, X. L. Zhao, and J. Z. Xu, "Preliminary failure investigation of a 52.3 m glass/epoxy composite wind turbine blade", *Engineering Failure Analysis*, vol. 44, pp. 345–350, 2014.

[29] F. Sayer, A. Antoniou, and A. van Wingerde, "Investigation of structural bond lines in wind turbine blades by sub-component tests", *International Journal of Adhesion and Adhesives*, vol. 37, pp. 129–135, 2012. Special Issue on Joint Design 3.

[30] J. Pohl, "Zerstörungsfreie charakterisierung adaptiver cfk-piezokeramik-verbunde : (konventionelle verfahren und health monitoring)", 2005.

[31] E. Joergensen, K. Borum, M. McGugan, C. Thomsen, F. Jensen, C. Debel, and B. Soerensen, "Full scale testing of wind turbine blade to failure - flapwise loading", 2004.

[32] R. Raišutis, E. Jasiūnienė, R. Šliteris, and A. Vladišauskas, "The review of non-destructive testing techniques suitable for inspection of the wind turbine blades", *Ultragarsas/Ultrasound*, vol. 63, no. 2, pp. 26–30, 2008.

[33] R. Raišutis, E. Jasiūnienė, and E. Žukauskas, "Ultrasonic NDT of wind turbine blades using guided waves", *Ultragarsas/Ultrasound*, vol. 63, no. 1, pp. 7–11, 2008.

[34] C. Gómez Muñoz, F. García Márquez, B. Hernández Crespo, and K. Makaya, "Structural health monitoring for delamination detection and location in wind turbine blades employing guided waves", *Wind Energy*, vol. 22, no. 5, pp. 698–711, 2019.

[35] G. Song, H. Li, B. Gajic, W. Zhou, P. Chen, and H. Gu, “Wind turbine blade health monitoring with piezoceramic-based wireless sensor network”, *International Journal of Smart and Nano Materials*, vol. 4, no. 3, pp. 150–166, 2013.

[36] C. MacLeod, S. Pierce, M. Morozov, R. Summan, G. Dobie, P. McCubbin, C. McCubbin, S. Dearie, and G. Munro, “Automated metrology and nde measurements for increased throughput in aerospace component manufacture”, in *E-Book of Abstracts 41st Annual Review of Progress in Quantitative Nondestructive Evaluation Conference*, p. 335, 2014.

[37] J. Rose, “Ultrasonic guided waves in structural health monitoring”, *Key Engineering Materials*, vol. 270-273, no. I, pp. 14–21, 2004.

[38] J. Rose and L. Soley, “Ultrasonic guided waves for anomaly detection in aircraft components”, *Materials Evaluation*, vol. 58, pp. 1080–1086, 2000.

[39] D. Hongerholt, G. Willms, and J. Rose, “Summary of results from an ultrasonic in-flight wing ice detection system”, *AIP Conference Proceedings*, vol. 615, no. 1, pp. 1023–1028, 2002.

[40] J. Rose, W. Zhu, and M. Zaidi, “Ultrasonic NDT of titanium diffusion bonding with guided waves”, *Materials Evaluation*, vol. 56, pp. 535–539, 1998.

[41] C. MacLeod, S. Pierce, J. Sullivan, A. Pipe, G. Dobie, and R. Summan, “An active whisking based remotely deployable nde sensor”, *IEEE Sensors Journal*, 2013.

[42] M. Lowe, G. Neau, and M. Deschamps, “Properties of guided waves in composite plates, and implications for NDE”, in *AIP Conference Proceedings*, vol. 700, pp. 214–221, American Institute of Physics, 2004.

[43] O. Putkis, R. Dalton, and A. Croxford, “The anisotropic propagation of ultrasonic guided waves in composite materials and implications for practical applications”, *Ultrasonics*, vol. 65, pp. 390–399, 2016.

[44] B. Zhang, X. Sun, M. Eaton, R. Marks, A. Clarke, C. Featherston, L. Kawashita, and S. Hallett, “An integrated numerical model for investigating guided waves

in impact-damaged composite laminates", *Composite Structures*, vol. 176, pp. 945–960, 2017.

[45] M. Gresil and V. Giurgiutiu, "Prediction of attenuated guided waves propagation in carbon fiber composites using Rayleigh damping model", *Journal of Intelligent Material Systems and Structures*, vol. 26, no. 16, pp. 2151–2169, 2015.

[46] S. Shoja, V. Berbyuk, and A. Boström, "Delamination detection in composite laminates using low frequency guided waves: Numerical simulations", *Composite Structures*, vol. 203, pp. 826–834, 2018.

[47] A. Arcos Jiménez, C. Gómez Muñoz, and F. García Márquez, "Machine learning for wind turbine blades maintenance management", *Energies*, vol. 11, no. 1, p. 13, 2018.

[48] A. Mardanshahi, V. Nasir, S. Kazemirad, and M. Shokrieh, "Detection and classification of matrix cracking in laminated composites using guided wave propagation and artificial neural networks", *Composite Structures*, vol. 246, p. 112403, 2020.

[49] S. Chaki, W. Harizi, G. Bourse, and M. Ourak, "Multi-technique approach for non destructive diagnostic of structural composite materials using bulk ultrasonic waves, guided waves, acoustic emission and infrared thermography", *Composites Part A: Applied Science and Manufacturing*, vol. 78, pp. 358–361, 2015.

[50] I. Viktorov, *Rayleigh and Lamb Waves: Physical Theory and Applications.* Plenum Press, 1967.

[51] K. Worden, "Rayleigh and Lamb waves - basic principles", *Strain*, vol. 37, pp. 167–172, 2001.

[52] J. Rose, *Ultrasonic Waves in Solid Media.* Cambridge University Press, 2014.

[53] T. Kundu, *Mechanics of Elastic Waves and Ultrasonic Nondestructive Evaluation.* CRC Press, 2019.

[54] “A review of non-destructive testing of composite materials”, *NDT International*, vol. 15, no. 2, pp. 75–86, 1982.

[55] V. Giurgiutiu, J. Bao, and W. Zhao, “Active sensor wave propagation health monitoring of beam and plate structures”, in *SPIE Smart Structures and Materials + Nondestructive Evaluation and Health Monitoring*, 2001.

[56] S. Kessler, S. Spearing, and C. Soutis, “Damage detection in composite materials using Lamb wave methods”, *Smart Materials and Structures*, vol. 11, no. 2, p. 269, 2002.

[57] C.-T. Ng and M. Veidt, “A Lamb-wave-based technique for damage detection in composite laminates”, *Smart Materials and Structures*, vol. 18, no. 7, p. 074006, 2009.

[58] W. Staszewski, B. Lee, L. Mallet, and F. Scarpa, “Structural health monitoring using scanning laser vibrometry: I. Lamb wave sensing”, *Smart Materials and Structures*, vol. 13, no. 2, p. 251, 2004.

[59] A. Clough and R. Edwards, “Scanning laser source Lamb wave enhancements for defect characterisation”, *NDT & E International*, vol. 62, pp. 99–105, 2014.

[60] M. Lowe, “Matrix techniques for modeling ultrasonic waves in multilayered media”, *IEEE Transactions on Ultrasonics, Ferroelectrics, and Frequency Control*, vol. 42, pp. 525–542, 1995.

[61] D. Alleyne and P. Cawley, “The interaction of Lamb waves with defects”, *IEEE Transactions on Ultrasonics, Ferroelectrics, and Frequency Control*, vol. 39, pp. 381–397, 1992.

[62] N. Guo and P. Cawley, “The interaction of Lamb waves with delaminations in composite laminates”, *The Journal of the Acoustical Society of America*, vol. 94, pp. 2240–2246, 1993.

[63] M. Sause, M. Hamstad, and S. Horn, “Finite element modeling of Lamb wave propagation in anisotropic hybrid materials”, *Composites Part B: Engineering*, vol. 53, pp. 249–257, 2013.

[64] B. Ben, S. Yang, C. Ratnam, and B. Ben, “Ultrasonic based structural damage detection using combined finite element and model Lamb wave propagation parameters in composite materials”, *The International Journal of Advanced Manufacturing Technology*, vol. 67, no. 5-8, pp. 1847–1856, 2013.

[65] Z. Ahmad, J. Vivar-Perez, and U. Gabbert, “Semi-analytical finite element method for modeling of Lamb wave propagation”, *CEAS Aeronautical Journal*, vol. 4, no. 1, pp. 21–33, 2013.

[66] C.-T. Ng, M. Veidt, L. Rose, and C. Wang, “Analytical and finite element prediction of Lamb wave scattering at delaminations in quasi-isotropic composite laminates”, *Journal of Sound and Vibration*, vol. 331, no. 22, pp. 4870–4883, 2012.

[67] P. Delsanto, T. Whitcombe, H. Chaskelis, and R. Mignogna, “Connection machine simulation of ultrasonic wave propagation in materials. I: the one-dimensional case”, *Wave Motion*, vol. 16, no. 1, pp. 65–80, 1992.

[68] P. Delsanto, R. Schechter, H. Chaskelis, R. Mignogna, and R. Kline, “Connection machine simulation of ultrasonic wave propagation in materials. II: the two-dimensional case”, *Wave Motion*, vol. 20, no. 4, pp. 295–314, 1994.

[69] P. Delsanto, R. Schechter, and R. Mignogna, “Connection machine simulation of ultrasonic wave propagation in materials III: The three-dimensional case”, *Wave Motion*, vol. 26, pp. 329–339, 1997.

[70] G. Dobie, A. Spencer, K. Burnham, S. Pierce, K. Worden, W. Galbraith, and G. Hayward, “Simulation of ultrasonic Lamb wave generation, propagation and detection for a reconfigurable air coupled scanner”, *Ultrasonics*, vol. 51, no. 3, pp. 258 – 269, 2011.

[71] K. Nadella and C. Cesnik, “Numerical simulation of wave propagation in composite plates”, in *Health Monitoring of Structural and Biological Systems 2012*, vol. 8348, p. 83480L, International Society for Optics and Photonics, 2012.

[72] K. Nadella and C. Cesnik, “Local interaction simulation approach for modeling wave propagation in composite structures”, *CEAS Aeronautical Journal*, vol. 4, pp. 35–48, 2013.

[73] Y. Shen and C. Cesnik, “Local interaction simulation approach for efficient modeling of linear and nonlinear ultrasonic guided wave active sensing of complex structures”, *Journal of Nondestructive Evaluation, Diagnostics and Prognostics of Engineering Systems*, vol. 1, no. 1, 2018.

[74] A. Pollock, “Classical wave theory in practical AE testing.” Progress in Acoustic Emission III: Proceedings of the 8th International Acoustic Emission Symposium, 1986.

[75] G. Mook, C. Willberg, U. Gabbert, and J. Pohl, “Lamb wave mode conversion in CFRP plates”, in *11th European Conference on Non-Destructive Testing*, 2014.

[76] C. Willberg, S. Koch, G. Mook, J. Pohl, and U. Gabbert, “Continuous mode conversion of lamb waves in CFRP plates”, *Smart Materials and Structures*, vol. 21, no. 7, 2012.

[77] S.-H. Rhee, J.-K. Lee, and J.-J. Lee, “The group velocity variation of Lamb wave in fiber reinforced composite plate”, *Ultrasonics*, vol. 47, no. 1, pp. 55–63, 2007.

[78] J. Lee, Y. Kim, and H. Kim, “Group velocity of Lamb wave S0 mode in laminated unidirectional CFRP plates”, in *Advances in Fracture and Strength*, vol. 297 of *Key Engineering Materials*, pp. 2213–2218, Trans Tech Publications Ltd, 2005.

[79] J. Lefebvre, V. Zhang, J. Gazalet, T. Gryba, and V. Sadaune, “Acoustic wave propagation in continuous functionally graded plates: an extension of the Legendre polynomial approach”, *IEEE Transactions on Ultrasonics, Ferroelectrics, and Frequency Control*, vol. 48, no. 5, pp. 1332–1340, 2001.

[80] C. Othmani, S. Dahmen, A. Njeh, and M. Ghozlen, “Investigation of guided waves propagation in orthotropic viscoelastic carbon–epoxy plate by Legendre polynomial method”, *Mechanics Research Communications*, vol. 74, pp. 27–33, 2016.

[81] C. Othmani, A. Njeh, and M. Ghozlen, “Influences of anisotropic fiber-reinforced composite media properties on fundamental guided wave mode

behavior: A Legendre polynomial approach", *Aerospace Science and Technology*, vol. 78, pp. 377–386, 2018.

[82] B. Lee and W. Staszewski, "Lamb wave propagation modelling for damage detection: II. damage monitoring strategy", *Smart materials and structures*, vol. 16, no. 2, p. 260, 2007.

[83] B. Ben, B. Ben, K. Vikram, and S. Yang, "Damage identification in composite materials using ultrasonic based Lamb wave method", *Measurement*, vol. 46, no. 2, pp. 904–912, 2013.

[84] P. Gardner, R. Fuentes, N. Dervilis, C. Mineo, S. Pierce, E. Cross, and K. Worden, "Machine learning at the interface of structural health monitoring and non-destructive evaluation", *Philosophical Transactions of the Royal Society A*, vol. 378, no. 2182, p. 20190581, 2020.

[85] S. Legendre, D. Massicotte, J. Goyette, and T. Bose, "Neural classification of Lamb wave ultrasonic weld testing signals using wavelet coefficients", *IEEE Transactions on Instrumentation and Measurement*, vol. 50, no. 3, pp. 672–678, 2001.

[86] Z. Su and L. Ye, "Lamb wave propagation-based damage identification for quasi-isotropic cf/ep composite laminates using artificial neural algorithm: Part I-methodology and database development", *Journal of Intelligent Material Systems and Structures*, vol. 16, no. 2, pp. 97–111, 2005.

[87] Y. Lu, L. Ye, Z. Su, L. Zhou, and L. Cheng, "Artificial neural network (ANN)-based crack identification in aluminum plates with lamb wave signals", *Journal of Intelligent Material Systems and Structures*, vol. 20, no. 1, pp. 39–49, 2009.

[88] O. Simeone, "A brief introduction to machine learning for engineers", *Foundations and Trends in Signal Processing*, vol. 12, no. 3-4, pp. 200–431, 2018.

[89] A. Deraemaeker and K. Worden, *New Trends in Vibration Based Structural Health Monitoring*, vol. 520. Springer Science & Business Media, 2012.

[90] G. Kerschen, K. Worden, A. Vakakis, and J.-C. Golinval, "Past, present and future of nonlinear system identification in structural dynamics", *Mechanical Systems and Signal Processing*, vol. 20, no. 3, pp. 505–592, 2006.

[91] C. Farrar, K. Worden, M. Todd, G. Park, J. Nichols, D. Adams, M. Bement, and K. Farinholt, “Nonlinear system identification for damage detection”, tech. rep., Los Alamos National Laboratory (LANL), Los Alamos, NM, 2007.

[92] G. Holmes, P. Sartor, S. Reed, P. Southern, K. Worden, and E. Cross, “Prediction of landing gear loads using machine learning techniques”, *Structural Health Monitoring*, vol. 15, no. 5, pp. 568–582, 2016.

[93] T. Rogers, G. Holmes, E. Cross, and K. Worden, “On a grey box modelling framework for nonlinear system identification”, in *Special Topics in Structural Dynamics, Volume 6*, pp. 167–178, Springer, 2017.

[94] T. Rogers, K. Worden, and E. Cross, “On the application of gaussian process latent force models for joint input-state-parameter estimation: With a view to Bayesian operational identification”, *Mechanical Systems and Signal Processing*, vol. 140, p. 106580, 2020.

[95] M. Lowe and O. Diligent, “Low frequency reflection characteristics of the S0 Lamb wave from a rectangular notch in a plate”, *The Journal of the Acoustical Society of America*, vol. 111, pp. 64–74, 2002.

[96] M. Lowe, P. Cawley, J.-Y. Kao, and O. Diligent, “The low frequency reflection characteristics of the fundamental antisymmetric Lamb wave A0 from a rectangular notch in a plate”, *The Journal of the Acoustical Society of America*, vol. 112, pp. 2612–2622, 2002.

[97] B. Lee and W. Staszewski, “Lamb wave propagation modelling for damage detection: I. two-dimensional analysis”, *Smart Materials and Structures*, vol. 16, no. 2, p. 249, 2007.

[98] A. Orifici, I. Herszberg, and R. Thomson, “Review of methodologies for composite material modelling incorporating failure”, *Composite structures*, vol. 86, pp. 194–210, 2008.

[99] P. Kijanka, A. Manohar, F. Lanza di Scalea, and W. Staszewski, “Damage location by ultrasonic Lamb waves and piezoelectric rosettes”, *Journal of Intelligent Material Systems and Structures*, vol. 26, pp. 1477–1490, 2015.

[100] M. Rébillat and N. Mechbal, "Damage localization in geometrically complex aeronautic structures using canonical polyadic decomposition of Lamb wave difference signal tensors", *Structural Health Monitoring*, vol. 19, pp. 305–321, 2020.

[101] A. Tobias, "Acoustic-emission source location in two dimensions by an array of three sensors", *Non-Destructive Testing*, vol. 9, pp. 9–12, 1976.

[102] T. Kundu, "Acoustic source localization", *Ultrasonics*, vol. 54, pp. 25–38, 2014.

[103] E. Flynn, M. Todd, P. Wilcox, B. Drinkwater, and A. Croxford, "Maximum-likelihood estimation of damage location in guided-wave structural health monitoring", *Proceedings of the Royal Society A: Mathematical, Physical and Engineering Sciences*, vol. 467, no. 2133, pp. 2575–2596, 2011.

[104] M. Jones, T. Rogers, K. Worden, and E. Cross, "A Bayesian methodology for localising acoustic emission sources in complex structures", *Mechanical Systems and Signal Processing*, vol. 163, p. 108143, 2022.

[105] Z. Tian and L. Yu, "Lamb wave frequency–wavenumber analysis and decomposition", *Journal of Intelligent Material Systems and Structures*, vol. 25, pp. 1107–1123, 2014.

[106] K. Zhou, Y. Zheng, J. Zhang, X. Xu, S. Ma, and Z. Wu, "A reconstruction-based mode separation method of Lamb wave for damage detection in plate structures", *Smart Materials and Structures*, vol. 28, p. 035033, 2019.

[107] I. Park, Y. Jun, and U. Lee, "Lamb wave mode decomposition for structural health monitoring", *Wave Motion*, vol. 51, pp. 335–347, 2014.

[108] C. Yeum, H. Sohn, and J. Ihn, "Lamb wave mode decomposition using concentric ring and circular piezoelectric transducers", *Wave Motion*, vol. 48, pp. 358–370, 2011.

[109] L. Solie and B. Auld, "Elastic waves in free anisotropic plates", *The Journal of the Acoustical Society of America*, vol. 54, no. 1, pp. 50–65, 1973.

[110] C. Chang and F. Yuan, "Extraction of guided wave dispersion curve in isotropic and anisotropic materials by matrix pencil method", *Ultrasonics*, vol. 89, pp. 143–154, 2018.

[111] P. Kudela, M. Radzienski, P. Fiborek, and T. Wandowski, “Elastic constants identification of woven fabric reinforced composites by using guided wave dispersion curves and genetic algorithm”, *Composite Structures*, vol. 249, p. 112569, 2020.

[112] B. I. Rylander, *Computational Complexity and the Genetic Algorithm.* University of Idaho, 2001.

[113] H. Kolsky, *Stress Waves in Solids*, vol. 1098. Courier Corporation, 1963.

[114] J. Achenbach, *Wave Propagation in Elastic Solids.* Elsevier, 1973.

[115] A. Ben-Israel, “A Newton-Raphson method for the solution of systems of equations”, *Journal of Mathematical Analysis and Applications*, vol. 15, no. 2, pp. 243–252, 1966.

[116] A. Ostrowski, *Solution of Equations and Systems of Equations: Pure and Applied Mathematics: A Series of Monographs and Textbooks, Vol. 9*, vol. 9. Elsevier, 2016.

[117] B. Pavlakovic, M. Lowe, D. Alleyne, and P. Cawley, “Disperse: A general purpose program for creating dispersion curves”, in *Review of Progress in Quantitative Nondestructive Evaluation*, pp. 185–192, Springer, 1997.

[118] D. Alleyne and P. Cawley, “A two-dimensional Fourier transform method for the measurement of propagating multimode signals”, *The Journal of the Acoustical society of America*, vol. 89, pp. 1159–1168, 1991.

[119] C. Ramadas, K. Balasubramaniam, A. Hood, M. Joshi, and C. V. Krishnamurthy, “Modelling of attenuation of Lamb waves using Rayleigh damping: Numerical and experimental studies”, *Composite Structures*, vol. 93, pp. 2020–2025, 2011.

[120] K. Schubert and A. Herrmann, “On attenuation and measurement of Lamb waves in viscoelastic composites”, *Composite Structures*, vol. 94, pp. 177–185, 2011.

[121] T. Bayes, “LII. an essay towards solving a problem in the doctrine of chances. by the late Rev. Mr. Bayes, FRS communicated by Mr. Price, in a letter to

John Canton, AMFR S", *Philosophical transactions of the Royal Society of London*, no. 53, pp. 370–418, 1763.

[122] O. I. Abiodun, A. Jantan, A. E. Omolara, K. V. Dada, N. A. Mohamed, and H. Arshad, "State-of-the-art in artificial neural network applications: A survey", *Heliyon*, vol. 4, no. 11, p. e00938, 2018.

[123] L. C. Marsh and D. R. Cormier, *Spline regression models.* No. 137, Sage, 2001.

[124] A. Zellner, *Bayesian Inference and Decision Techniques, Studies of Bayesian and Econometrics and Statistics*, vol. 6, ch. On Assessing Prior Distributions and Bayesian Regression Analysis with g Prior Distributions, pp. 233–243. Elsevier, 1986.

[125] C. Rasmussen and C. Williams, *Gaussian Processes for Machine Learning (Adaptive Computation and Machine Learning).* The MIT Press, 2005.

[126] A. O'Hagan, "Curve fitting and optimal design for prediction", *Journal of the Royal Statistical Society: Series B (Methodological)*, vol. 40, pp. 1–24, 1978.

[127] E. Padonou and O. Roustant, "Polar gaussian processes for predicting on circular domains." 2015.

[128] G. Wahba, *Spline Models for Observational Data.* Society for Industrial and Applied Mathematics, 1990.

[129] S. da Silva, "Data-driven model identification of guided wave propagation in composite structures", *Journal of the Brazilian Society of Mechanical Sciences and Engineering*, vol. 40, p. 543, 2018.

[130] P. Mangalgiri, "Composite materials for aerospace applications", *Bulletin of Materials Science*, vol. 22, no. 3, pp. 657–664, 1999.

[131] M. Pervaiz, S. Panthapulakkal, M. Sain, and J. Tjong, "Emerging trends in automotive lightweighting through novel composite materials", *Materials sciences and Applications*, vol. 7, no. 01, p. 26, 2016.

[132] P. Veers, T. Ashwill, H. Sutherland, D. Laird, D. Lobitz, D. Griffin, J. Mandell, W. Musial, K. Jackson, and M. Zuteck, "Trends in the design, manufacture and

evaluation of wind turbine blades", *Wind Energy: An International Journal for Progress and Applications in Wind Power Conversion Technology*, vol. 6, no. 3, pp. 245–259, 2003.

[133] D. Duvenaud, *Automatic Model Construction with Gaussian Processes.* PhD thesis, University of Cambridge, 2014.

[134] B. Lee and W. Staszewski, "Modelling of Lamb waves for damage detection in metallic structures: Part II. wave interactions with damage", *Smart Materials and Structures*, vol. 12, pp. 815–824, 2003.

[135] K. Holford, M. Eaton, J. Hensman, R. Pullin, S. Evans, N. Dervilis, and K. Worden, "A new methodology for automating acoustic emission detection of metallic fatigue fractures in highly demanding aerospace environments: An overview", *Progress in Aerospace Sciences*, vol. 90, pp. 1–11, 2017.

[136] H. Akaike, "Markovian representation of stochastic processes and its application to the analysis of autoregressive moving average processes", in *Selected Papers of Hirotugu Akaike*, pp. 223–247, Springer, 1998.

[137] R. Miller, M. Carlos, R. Findlay, V. Godinez-Azcuaga, M. Rhodes, F. Shu, and W. Wang, *Acoustic Emission Source Location, 3rd Edition.* ASNT, 2005.

[138] D. Olsson and L. Nelson, "The Nelder-Mead simplex procedure for function minimization", *Technometrics*, vol. 17, pp. 45–51, 1975.

[139] L. Le Cam, "Maximum likelihood: an introduction", *International Statistical Review/Revue Internationale de Statistique*, pp. 153–171, 1990.

[140] D. Gamerman and H. Lopes, *Markov chain Monte Carlo: stochastic simulation for Bayesian inference.* CRC Press, 2006.

[141] E. Lehmann and G. Casella, *Theory of Point Estimation.* Springer Science & Business Media, 2006.

[142] W. Hastings, "Monte Carlo sampling methods using Markov chains and their applications", *Biometrika*, vol. 57, pp. 97–109, 1970.

[143] R. Neal, *Handbook of Markov Chain Monte Carlo*, ch. MCMC Using Hamiltonian Dynamics, pp. 116–162. CRC Press, 2011.

[144] M. Betancourt and M. Girolami, "Hamiltonian Monte Carlo for hierarchical models", *Current trends in Bayesian methodology with applications*, vol. 79, no. 30, pp. 2–4, 2015.

[145] Stan Development Team, *Stan Modelling Language Users Guide and Reference Manual.* https://mc-stan.org, 2021. 2.28.

[146] E. Papatheou, G. Manson, R. J. Barthorpe, and K. Worden, "The use of pseudo-faults for novelty detection in shm", *Journal of Sound and Vibration*, vol. 329, no. 12, pp. 2349–2366, 2010.

[147] T. Dardeno, M. Haywood-Alexander, R. Mills, L. Bull, N. Dervilis, and K. Worden, "Investigating the effects of ambient temperature on feature consistency in vibration-based shm", 2021.